The influence of crustal heterogeneity on translational and rotational motions in the seismic coda

Von der Fakultät für Physik und Geowisschenschaften
der Universität Leipzig
genehmigte

Dissertation

zur Erlangung des akademischen Grades
doctor rerum naturalium
(Dr. rer. nat)

vorgelegt von

Peter Jost Gaebler

geboren am 11. Dezember 1982 in Ingolstadt

Gutachter

Prof. Dr. Michael Korn
Prof. Dr. Hisashi Nakahara
Dr. Christoph Sens-Schönfelder

Tag der Verleihung: 16. November 2015

Dedicated to Lisa and Josef

Bibliographical information

Monte Carlo solutions to the radiative transfer equations are used to model translational and rotational multi-component seismogram envelopes in random elastic media with deterministic background structure assuming multiple anisotropic scattering. The synthesized multi-component seismogram envelopes are compared to various seismic signals from local, regional and teleseismic earthquakes to estimate crustal scattering and attenuation parameters in south-east Germany and to study the influence of the crustal heterogeneity on the generation of the seismic coda. The results are in good agreement with comparable studies in Europe and suggest that the preferred model of crustal heterogeneity correctly describes the main mechanisms generating the seismic coda of the local, regional and teleseismic events.

Statement of authorship

- The thesis I have submitted entitled *The influence of crustal heterogeneity on translational and rotational motions in the seismic coda* is my own work.

- I have only used the sources indicated and have not made unauthorized use of services of a third party. Where the work of others has been quoted or reproduced, the source is always given.

- I have not already presented this thesis or parts thereof to a university as part of an examination or degree.

- I affirm that the above is the absolute truth to the best of my knowledge and that I have not concealed anything.

_____

Peter Gaebler

Acknowledgements

Zusammenfassung

In dieser Studie werden Monte Carlo Lösungen für die Energietransfergleichungen genutzt, um Seismogrammeinhüllende von Translations- und Rotationsbewegungen zu modellieren. Die Ergebnisse der Monte Carlo Simulationen werden durch einen Vergleich mit 3D finiten Differenzen Simulationen verifiziert. Diese Modellierung findet in einem elastischen Zufallsmedium mit deterministischer Hintergrundstruktur unter Annahme multipler anisotroper Streuung statt. Die Beobachtung und Modellierung der drei zusätzlichen Komponenten der Rotationsbodenbewegungen kann unabhängige Informationen über die Ausbreitung seismischer Wellen im Erdkörper liefern. Rotationsbewegungen um die vertikale Achse in der P-Wellen Koda sind in diesem Zusammenhang von speziellem Interesse, da sie nur von horizontal polarisierten Scheerwellen angeregt werden können. Die gemessenen Rotationsbewegungen deuten folglich auf Konversionen von P- zu SH-Energie durch multiple Streuung an 3D-Heterogenitäten hin. Für die Bestimmung von Streu- und Dämpfungsparametern im Südosten Deutschlands (Gräfenberg Array, Vogtland) werden synthetisch erzeugte, mehrspurige Seismogrammeinhüllende mit Daten lokaler und regionaler Schwarmbeben und teleseismicher Ereignisse verglichen. In einem ersten Schritt werden frequenzabhängige Krustenparameter für die Vogtlandregion mittels eines lokalen Datensatzes von nahen Schwarmbeben bestimmt. Die Resultate mittels elastischer Energietransfertheorie werden mit Ergebnissen aus Simulationen mittels akustischer Energietransfertheorie verglichen. Beide Methoden liefern ähnliche Parameter und sagen einen größeren Einfluss der intrinsichen Dämpfung im Vergleich zur Streudämpfung voraus. Aus den elastischen Simulationen geht hervor, dass für die Beschreibung der Daten Vorwärtsstreuung angenommen werden muss, die Stärke dieser lässt sich jedoch nicht auflösen. In einem zweiten Schritt werden die Streu- und Dämpfungseigenschaften der Erdkruste im Untergrund des Gräfenberg Arrays untersucht. Hierzu wird eine nicht-lineare genetische Inversion von Seismogrammeinhüllenden regionaler Ereignisse bei hohen Frequenzen (4–8 Hz) verwendet. Das bevorzugte Modell der Krustenheterogenität wird durch ein exponentielles Zufallsmedium, einer mittleren freien Transportweglänge von ca. 420 km und einem Qualitätsfaktor für S-Wellen Q_S^i von ca. 700 beschrieben. Ein letzter Schritt vergleicht Simulationen von teleseismischen P-Welleneinsätzen mit beobachteten Seismogrammeinüllenden von tiefen Erdbeben unter der Nutzung der Parameter aus der regionalen Inversion. Die Simulationen der teleseismischen Ereignisse mit den Parametern der regionalen Inversion zeigen eine gute Übereinstimmung mit den gemessenen Seismogrammeinhüllenden. Dieser Vergleich beinhaltet Ringlaserbeobachtungen der Rotationsbewegungen um die vertikale Achse, welche aus dem angenommenen Streumodell resultieren. Das Modell sagt voraus, dass die elastische Energie in der teleseismischen P-Wellen Koda im Gegensatz zur Koda lokaler oder regionaler Ereignisse nicht gleichverteilt ist, sondern einen Überschuss an Scheerenergie beinhaltet. Die Resultate aus den Untersuchungen der lokalen, regionalen und teleseismischen Datensätze zeigen, dass die Streuereignisse, welche die seismische Koda erklären, hauptsächlich in der Kruste unterhalb der seismischen Empfänger stattfinden. Streuung des Wellenfeldes im Mantel wird für die Erklärung der Daten nicht benötigt, schwache Streuung im lithosphärischen Mantel kann jedoch nicht ausgeschlossen werden.

Summary

In this study Monte Carlo solutions to the radiative transfer equations are used to model translational and rotational motion seismogram envelopes in random elastic media with deterministic background structure assuming multiple anisotropic scattering. The results of the Monte Carlo radiative transfer theory simulations are verified by comparisons with 3D full wave field finite difference simulations. The observation and modeling of the three additional components of rotational ground motions can provide independent information about seismic wave propagation in the Earth's structure. Rotational motions around the vertical axis observed in the P-wave coda are of particular interest as they can only be excited by horizontally polarized shear waves and therefore indicate the conversion from P- to SH-energy by multiple scattering at 3D-heterogeneities. Scattering and attenuation parameters in south-east Germany beneath the Gräfenberg array and in the Vogtland region are estimated by comparisons of synthesized multi-component seismogram envelopes to seismic data from local and regional swarm earthquakes and to teleseismic events. In a first step, frequency dependent scattering and attenuation parameters from a local data set are estimated for the Vogtland region using nearby swarm earthquakes. The results from the elastic simulations are compared to outcomes from acoustic radiative transfer simulations. Both methods yield similar results and suggest that intrinsic attenuation dominates scattering attenuation. From the elastic simulations it is observable, that forward scattering is required to explain the data. However, the amount of forward scattering strength remains unresolvable. In a second step scattering and attenuation parameters beneath the Gräfenberg array are estimated using a nonlinear genetic inversion of seismogram envelopes from regional events at high frequencies (4–8 Hz). The preferred model of crustal heterogeneity consists of a random medium described by an exponential autocorrelation function with a transport mean free path length of ~ 420 km. The quality factor for elastic S-wave attenuation Q_S^i is around 700. In a final step simulations of teleseismic P-wave arrivals, using this estimated set of scattering and attenuation parameters, are compared to observed seismogram envelopes from deep events. Simulations of teleseismic events with the parameters found from the regional inversion show good agreement with the measured seismogram envelopes. This includes ringlaser observations of vertical rotations in the teleseismic P-wave coda that naturally result from the proposed model of wave scattering. The model also predicts, that the elastic energy recorded in the teleseismic P-coda is not equipartitioned, unlike the coda of regional events, but contains an excess of shear energy. The combined results from the three different data sets suggest that scattering generating the seismic coda mainly occurs in the crustal part of the lithosphere beneath the receivers. The observations do not require scattering of high frequency waves in the mantle, but weak scattering in the lithospheric mantle cannot be ruled out.

Contents

1 Introduction

Back in the year 1692, the English astronomer, mathematician and physicist Edmond Halley, best know for his computation of the orbit of *Halley's comet*, put forth the theory of the hollow earth (Halley, 1692). He suggested the Earth to be hollow on the inside with a 500 mile thick shell forming the outside of the planet. Inside the shell, he proposed two inner concentric shells and one innermost core with diameters of roughly the diameters of the planets Venus, Mars and Mercury, respectively. He presumed, that each of the shells was separated by an atmosphere and that each shell and the innermost core all have individual magnetic poles. Furthermore all the shells were supposed to rotate at different speeds relatively to each other. Halley's theory was based on the examination of the continuous movement of the magnetic inclination lines using data from all over the world. In the cause of history many scientists picked up on Halley's idea and suggested various hollow Earth models, even in the present days some advocates of this theory exist. With the deepest drilling hole in the world at the moment only reaching a depth of around 12000 m (Exxon, 2015), it is obviously not possible to examine the entire Earth's interior with the naked eye, but modern science clearly proves, that the Earth is anything but hollow on the inside. Today's scientific understanding of a solid Earth comes from conclusions drawn from various methods, for example including the observation and investigation of topography and bathymetry, measurements of the geomagnetic field, sampling of rocks brought to the Earth's surface by volcanic activity, from gravity field measurements or from the Earth's flattening. One of the most powerful approaches to derive our current understanding of the Earth's interior on various scales, from thousands of kilometers down to a few meters, is seismology, the study of seismic waves.

Considering the Earth's interior on a larger scale, it can be described as a multitude of spherical layers. These layers can be distinguished by their chemical or physical properties. These large-scale layers can be determined by examining travel time curves of seismic waves (Bullen and Bolt, 1985), by surface wave dispersion analysis or investigations of the Earth's normal modes (Dziewonski and Anderson, 1981). The outermost layer is the silicate rich and solid crust, which on average extends down to 38 km beneath continents and reaches depths of 7–8 km beneath the oceans (Fowler, 2005). The crustal part of the Earth was identified in the beginning of the 20th century by Milne (1906) and Rutherford (1907). Adjacent to the Earth's crustal layer is the mantle, first described by Wiechert (1897). The mantle extends down to a depth of 2900 km and is physically and chemically different from the crust. It can be divided up into

different zones. The first zone (40–100 km) is the lithospheric part of the mantle and has a rigid solid behavior, together with the crust it forms the lithosphere. Beneath the lithosphere extends the asthenosphere down to a depth of 300 km, which has a highly plastic behavior due to its high temperatures. It is a low velocity and low viscosity zone. Lithosphere and asthenosphere form the upper part of the mantle. The border between upper mantle and lower mantle is represented by a $\sim$ 400 km thick transition zone (300–700 km), which includes several discontinuities at for example 410, 520 and 660 km depth. This discontinuities can be observed as strong reflectors of seismic waves. The lower mantle extends down to 2900 km with the last 200 km (2700-2900 km) referring to as the D''-layer. In this layer a very high temperature contrast of $\sim$ 1000 K from mantle to core can be observed. This D''-layer can be regarded as the core mantle boundary. The Earth's core can be divided into an outer core (2900–5100 km) and in an inner core (5100–6371 km). The existence of a core was identified by for example Oldham (1906) and Gutenberg (1914) in the early 20th century. The outer core is liquid (Jeffreys, 1926) and mainly consists out of an iron-nickel melt. The inner core on the other hand is solid (Lehmann, 1936) and is mainly comprised out of iron. In addition to this large-scale approximation of spherical layers, many medium-scale 3D-heterogeneities can be observed. These inhomogeneities are normally larger than the predominant seismic wavelength and can be resolved using tools like seismic tomography Nolet (1987). This heterogeneities for example include continental shields with high velocity roots (Fowler, 2005), mantle plumes (Zhao, 2001) or subduction zones (Spakman et al., 1988). Additionally to the large- and medium-scale heterogeneous structures, the Earth's subsurface is made up out of very small-scale 3D-heterogeneities, normally smaller than the predominant seismic wavelength. These structures cannot be resolved with classical methods like seismic tomography or the analysis of the Earth's normal modes and require a statistical description as a random continuous medium concerning for example density and velocity fluctuations. To describe these small-scale structures scattering theory can be used.

The purpose of this study is to investigate these small-scale structures and to evaluate the contribution of the local crustal heterogeneities to the generation of scattered elastic energy recorded in various seismic signals. Of specific interest in this context are records of rotational ground motions that, acting as a polarization filter for shear energy, can provide additional independent information about conversion scattering, that couples P- and S-wave propagation. In a first part of the study, frequency dependent crustal scattering and intrinsic attenuation parameters in the Vogtland region are estimated using local swarm earthquakes. The results are obtained using acoustic and elastic radiative transfer theory (RTT). This local data set will also be used to investigate the resolution limits of the random medium parameters as well as trade-offs between the parameters. In a next step a genetic inversion of regional swarm earthquakes from the Vogtland region is used to describe the crustal structure beneath the Gräfenberg array in south-east Germany in terms of its scattering and attenuation properties. In a third step it is tested whether the medium heterogeneity, described by the parameters found in the regional inversion, is suitable for the generation of seismogram envelopes

of teleseismic earthquakes. For this, seismogram envelopes of P- and PcP-coda from deep teleseismic events, including rotational motions, are simulated and compared to ringlaser recordings of the vertical rotation rate and to common translational motion seismograms.

This thesis starts with a short introduction on the scattering of seismic waves in chapter 2, followed by some general information about rotational motions in seismology (chapter 3). Chapter 4 introduces the approach of acoustic and elastic RTT, its solutions using Monte Carlo (MC) techniques and the modeling of multi-component translational and rotational seismogram envelopes from local, regional and teleseismic events. A validation of the RTT modeling method by comparisons to 3D finite difference (FD) simulations is described in chapter 5. Chapter 6 features the investigations of a local data set concerning the estimation of scattering and attenuation parameters in different frequency bands. Results from the genetic inversion of the regional data set are presented in chapter 7. Based on the results from the regional inversion, a comparison of rotational and translational motion seismogram envelopes to a set of records from deep teleseismic events is given in chapter 8. Results from the different datasets are discussed and interpreted in chapter 9.

The content from chapter 4, 7 and 8 is published in Geophysical Journal International (Gaebler et al., 2015a). Content from chapter 6 is published in Geophysical Journal International (Gaebler et al., 2015b).

2 Scattering of seismic waves

As this study is based on the analysis of scattered seismic waves, it starts with a short introduction on scattered energy in the seismic coda in section 2.1. Different random medium realizations, which represent the random small-scale heterogeneities of the Earth's structure, are presented in section 2.2. An overview of previous investigations of crustal wave scattering and intrinsic attenuation is given in section 2.3.

2.1 Scattered energy in the seismic coda and modeling methods

Since the early 1970s, the observation, modeling and interpretation of coda waves is receiving attention in the field of seismology. According to Aki (1969) the seismic coda can be referred to as seismic energy recorded after the passage of the primary seismic waves (for example P- or S-waves) and can be explained with the scattering of seismic waves at randomly distributed small-scale heterogeneities in the Earth's subsurface (Aki and Chouet, 1975). The development of a P-wave coda due to scattering events at small-scale heterogeneities is illustrated in figure 2.1. The direct initial arrival of seismic energy undergoes no scattering events and travels along the minimum-time path from the earthquake hypocenter to the receiver (figure 2.1, left). Energy that is scattered, arrives later in the seismogram (figure 2.1, middle and right). This scattered energy could have been scattered at a number of individual scatterers that would lead to the observed travel time. For single scattering events and a constant homogeneous velocity in the medium, the possible scatterers for one single observed travel time form an ellipsoid with the source and the receiver being the focal points of the ellipsoid. For multiple scattering or for a medium with a heterogeneous velocity structure the travel paths can become arbitrarily complicated.

The energy decay of the seismic coda with time depends on the investigated frequency band and on the local properties of the subsurface. Parameters such as source mechanism, epicentral distance, event magnitude and source depth show minor influence on the energy decay in the seismic coda (Trégourès et al., 2002). Therefore many studies relate the physical properties of the subsurface to the observed local, regional or teleseismic coda (Aki, 1969; Abubakirov and Gusev, 1990; Korn, 1997; Calvet and Margerin, 2013).
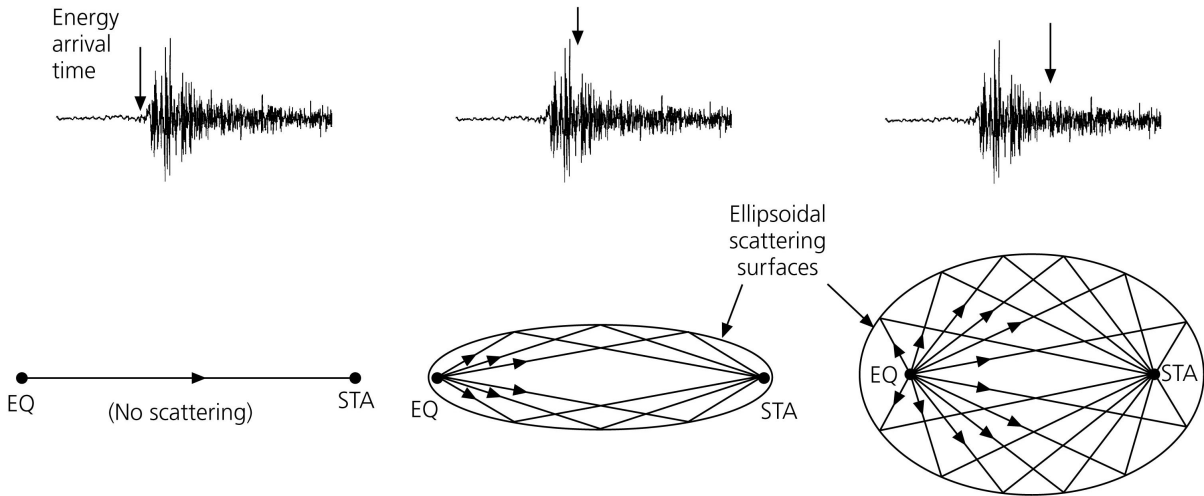
Figure 2.1: Formation of a P-wave coda due to single scattering. *left*: First arrival of seismic energy, following the minimum-time path from earthquake (EQ) to receiver (STA). No scattered energy is visible at this observation time. *middle*: Scattered energy after the first onset arrives from an infinite number of possible scatterers that yield the same arrival time. In a homogeneous velocity model the locus of these scattering points forms an ellipsoidal surface. *right*: Same as middle part, but a later arrival of seismic energy, which results in a larger ellipsoidal surface. Figure redrawn from Stein and Wyssession (2009).

The total attenuation Q^t of the seismic energy in the direct wave is not only due to anelastic attenuation measured by the intrinsic quality factor Q^i, but is a combination of intrinsic attenuation and amplitude decrease of the seismic wave field due to redistribution of energy by scattering described by the quality factor Q^s (Aki, 1981; Dainty, 1981; Toksöz et al., 1988). The total or apparent attenuation Q^t is therefore given by:

$$\frac{1}{Q^t} = \frac{1}{Q^i} + \frac{1}{Q^s}. \tag{2.1}$$

The decay of the coda amplitude can in analogy be expressed by a quality factor Q^c. The spatial scale of the small-scale heterogeneities that interact with the wave field to generate the scattered part of the seismic energy is below the resolution limits of classical imaging techniques such as tomography or surface wave dispersion analysis. This prohibits a deterministic investigation of the small-scale heterogeneities. It is instead possible to regard the heterogeneities as a continuous random medium. The medium is often described by parameters such as fluctuation strength ϵ and the correlation length a. These parameters are a measure for the strength of the velocity or density variations in the medium, respectively for the length scale of these fluctuations. Examples of different random medium realizations are given in section 2.2. Parameters to describe the effect of the scattering in the Earth's subsurface on the propagation of seismic waves are the mean free path l^0 and the transport mean free path l^*. The mean free path

l^0 is a measure of characteristic distance between two scattering events, the transport mean free path l^* can be regarded as the propagation distance required for a wave to lose memory of its initial direction.

Several methods were proposed to model the generation of the seismic coda due to scattering at statistically distributed heterogeneities in the subsurface (Sato et al., 2012). One of the simplest approaches to simulate the seismic energy decay in the coda assumes single, isotropic scattering of acoustic energy and was described by Sato (1977). Single scattering theory assumes, that the seismic waves are scattered only once between source and receiver. Scattering events in this theory are supposed to be isotropic, which means there is no preferred direction of scattering of the energy. Therefore cases of forward scattering are not included in this theory. The scattering of S-waves is treated in the limits of the acoustical approximation. Scattering of P-waves and conversions between S- and P-energy are not included in this theory. The acoustic approach can for example be used for the analysis of the S-wave coda and consequently for the estimation of medium, source and site parameters (Sens-Schönfelder and Wegler, 2006). The equipartition of seismic waves, reached after long lapse times in the seismic coda, results in a constant ratio of S- to P-energy, that is clearly dominated by the amount of present S-energy. This dominance of S-energy is the reason for modeling the propagation of S-energy and neglecting the transport of P-energy. This makes the acoustic approach useful for the investigation of coda waves and the direct S-wave arrival. One possible method to model the propagation of seismic energy in a scattering medium is the RTT. Details to this theory and a possible method for the solution of the underlying equations is discussed and presented in chapter 4.

A variety of studies make use of the diffusion approximation to model the seismic coda (Dainty et al., 1974; Aki and Chouet, 1975; Dainty, 1981). This approach is only valid for very long lapse times. Other studies clearly show the importance of multiple scattering of the seismic wave field at heterogeneities in the Earth's subsurface (Wu, 1985; Wu and Aki, 1988; Abubakirov and Gusev, 1990; Hoshiba et al., 1991; Margerin et al., 2000; Wegler and Lühr, 2001; Sens-Schönfelder et al., 2009). Abubakirov and Gusev (1990) and Hoshiba (1995) introduced the theory for anisotropic scattering. This approach now allows to include forward scattering processes. The modeling of elastic energy allows to treat P- and S-energy, as well as conversions between the two modes. Multiple elastic scattering was for example modeled by Margerin et al. (2000) using randomly distributed spheres in an otherwise homogeneous background medium. This theory was extended to a medium with continuous random inhomogeneities (Przybilla et al., 2006). Sens-Schönfelder et al. (2009) describe an algorithm based on RTT to model seismogram envelopes for multiple anisotropic scattering of elastic waves at randomly distributed heterogeneities in a deterministic macroscopic background structure. This method is able to model not only the coda, but also the envelopes of the direct onsets of the primary waves.

2.2 Random media realizations

The Earth's subsurface is heterogeneous and can only to a certain extent be described by classical imaging techniques such as tomography. The spatial scale of the heterogeneity, that interacts with the high frequency wave field to generate the scattered part, is normally smaller than the predominant seismic wavelength, which prohibits a deterministic investigation of the medium. Instead it is possible to regard the heterogeneities as a continuous random medium, where the medium properties like e.g. seismic wave velocity v are given as

$$\rho(\mathbf{x}) = v_0(1 + \xi(\mathbf{x})), \tag{2.2}$$

with v_0 being the average background value and $\xi(\mathbf{x})$ describing its random fluctuations. The fluctuations are described by their statistical properties and are often defined using the autocorrelation function (ACF) R. In a statistically homogeneous isotropic medium, the ACF only depends on the absolute value of distance $r = |\mathbf{r}|$ between two points. Such ACFs are mainly characterized by two parameters, the fluctuation strength ϵ and the correlation length a. The fluctuation strength ϵ is a measure of amplitude of the velocity or density fluctuations around their background value. The correlation length a gives information about the length scale of the fluctuations. For numerical modeling the medium fluctuations are usually described by their power spectral density (PSD) function P, which is the Fourier transform of the ACF. The most commonly used random media have Gaussian, exponential or von Karman type ACFs (Sato et al., 2012). Example realizations of the three random media types with a correlation length a of 1 km are illustrated in figure 2.2.

(a) gaussian (b) exponential (c) von Karman
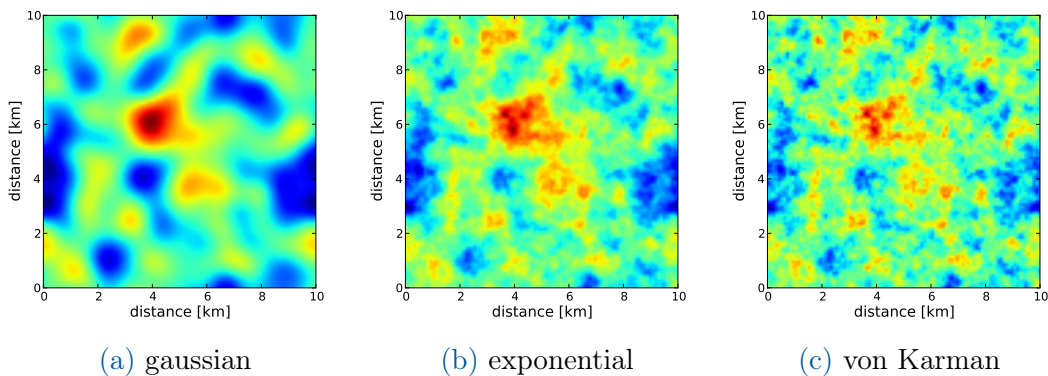
Figure 2.2: Different medium realizations. All three figures show a medium with an autocorrelation length a of 1 km. The Gaussian medium (a) is a relatively smooth medium with fluctuations of similar size. The exponential medium (b) shows a moderate roughness in comparison to the Gaussian medium. The von Karman medium (c) is even rougher than the exponential medium, in this case the Hurst parameter ν, which defines the roughness, is set to 0.1.

Gaussian ACFs are used to describe relatively smooth media with fluctuations of similar size. The Gaussian ACF $R_g(r)$ and the corresponding PSD function $P_g(m)$ are given as

$$R_g(r) = \epsilon^2 e^{-r^2/a^2}, \tag{2.3a}$$

$$P_g(m) = \epsilon^2 \sqrt{\pi^3} a^3 e^{m^2 a^2/4}, \tag{2.3b}$$

with m being the magnitude of the wave number vector $\mathbf{m}$ ($m = |\mathbf{m}|$). A wide range of random media with small-scale fluctuations is described by the von Karman ACF. Additional to the fluctuation strength ϵ and correlation length a, a third parameter ν is introduced, which describes the roll-off of the amplitude of fluctuations at high wave numbers, which governs the roughness of the medium. The Hurst parameter ν ranges from 0–0.5, with smaller values of ν increasing the roughness of the medium. The von Karman ACF $R_{vk}(r)$ and the corresponding PSD function $P_{vk}(m)$ are given by

$$R_{vk}(r) = \frac{\epsilon^2 2^{1-\nu}}{\Gamma(\nu)} \left(\frac{r}{a}\right)^\nu K_\nu \left(\frac{r}{a}\right), \tag{2.4a}$$

$$P_{vk}(m) = \frac{8\pi^{3/2}\epsilon^2 a^3 \Gamma(\nu + 3/2)}{\Gamma(\nu)(1 + a^2 m^2)^{\nu+3/2}}, \tag{2.4b}$$

with Γ being the gamma function and K_ν being the modified Bessel function of second kind and order ν. In this study a random medium with exponential ACF is used, which is a special case of the von Karman medium with moderate roughness expressed by $\nu = 0.5$. The exponential ACF $R_e(r)$ and the corresponding PSD function $P_e(m)$ are defined as

$$R_e(r) = \epsilon^2 e^{-r/a}, \tag{2.5a}$$

$$P_e(m) = \frac{8\pi\epsilon^2 a^3}{(1 + a^2 m^2)^2}. \tag{2.5b}$$

2.3 Previous investigations of crustal wave scattering and intrinsic attenuation

Scattering and intrinsic attenuation parameters of the crust in many different regions worldwide have been subject to numerous studies using a broad range of datasets, models and methods. Inhomogeneities in volcanic areas can be very strong and the mean free path length l^0 can reach values from as low as 0.1 up to 150 km (Abubakirov and Gusev, 1990; Fehler et al., 1992; Wegler and Lühr, 2001). Areas with common continental crust generally show weaker scattering than volcanic areas. This is visible in higher values for the mean free path length l^0. In Germany, Sens-Schönfelder and Wegler (2006) used an acoustic and isotropic scattering model to estimate a mean free path length of 690 km and an intrinsic Q-value for S-waves Q_S^i of 679 at a frequency

of 3 Hz. A further investigation by Sens-Schönfelder et al. (2009) in France using an elastic, multiple anisotropic scattering approximation resulted in a transport mean free path of 761 km and a Q_S^i-value of 625 at a 3 Hz frequency. A study by Rothert (2000) is of special interest here, as it covers a similar region as our investigations, the area beneath the Gräfenberg array in south-east Germany. Wave fronts from teleseismic P-wave arrivals were analyzed to describe the heterogeneities in the Earth's subsurface. A random medium with velocity fluctuations ϵ of 3–7 % and a correlation length a of 0.6–4.8 km is proposed to describe the inhomogeneities. Hock et al. (2004) found values of 1–2 km for the correlation length a and 4–5 % for the fluctuation strength ϵ in the same area. Similar values for crustal wave scattering have for example been reported by Levander and Holliger (1992) or Calvet and Margerin (2013). A comparison of crustal intrinsic attenuation and scattering parameters from selected studies is given in table 2.1. For a more complete review on investigations of crustal wave scattering and intrinsic attenuation the reader is referred to Sato et al. (2012).

reference	region	distance	f_c [Hz]	Q_S^{i-1}	l^0 [km]	l^* [km]	ϵ [%]	a [km]
[1]	Kamchatka	local	3	0.0032	150	—	—	—
[2]	Japan	local	3	0.0026	150	—	—	—
[3]	Germany	teleseismic	2	—	—	—	3-7	0.6-4.8
[4]	France	regional	3	0.0013	250	250	—	—
[5]	Germany	regional	3	0.0013	690	690	—	—
[6]	Norway	local	3	—	175	250	—	—
[7]	France	regional	3	0.0016	—	761	2.1	0.77
[8]	France	local	6	0.0013	>80	400	3.7	0.16
[9]	Germany	regional	6	0.0015	290	420	2.9	0.27

Table 2.1: Comparison of crustal attenuation and scattering parameters for different study areas. f_c is the center frequency of the investigated frequency band. [1] Abubakirov and Gusev (1990), [2] Fehler et al. (1992), [3] Rothert (2000), [4] Lacombe et al. (2003), [5] Sens-Schönfelder and Wegler (2006), [6] Przybilla et al. (2009), [7] Sens-Schönfelder et al. (2009), [8] Calvet and Margerin (2013), [9] section 7.3 in this study.

3 Rotational motions in seismology

This chapter covers the topic of rotational motions in seismology. It starts with some basic information and a short introduction on rotational motions in the seismic wave field in section 3.1, followed by a description of rotational motion sensors used in this study in section 3.2. In section 3.3 some data examples from the Wettzell ringlaser are presented and possible applications of the additional use of the measured rotational motions are given. The testing and the installation of the R2 rotational motion sensor is described in section 3.4.

3.1 Rotational motions of seismic waves

In classical seismology only the three components of translational motion (rigid body translations) of the seismic wave field are investigated. Rigid body translations are referred to, if all points that make up a volume, move together without a change of shape of the volume. If during the movement the volume changes its shape, this process is referred to as deformation. This deformation processes are not included in the classical observation of the translational motions and require additional measurements. To differentiate between rigid body motions and the deformation, the relative motion of neighboring points in the volume has to be considered. Here the notation from Segall (2010) is followed and a displacement $\mathbf{u}$ of a point at position x relative to an arbitrary origin x_0 is investigated (see figure 3.1).
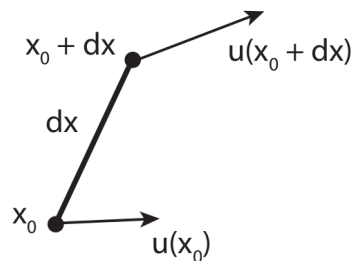

Figure 3.1: Generalized displacement of a line segment $\mathbf{dx}$. The point $\mathbf{x_0}$ is displaced by an amount $\mathbf{u(x_0)}$. The end point of the line segment $\mathbf{x_0} + \mathbf{dx}$ is displaced by $\mathbf{u(x_0} + \mathbf{dx)}$. Figure redrawn from Segall (2010).

3 Rotational motions in seismology

The Taylor series expansion of the displacement $\mathbf{u}$ about the origin x_0 is given as

$$u_i(x) = u_i(x_0) + \left.\frac{\partial u_i}{\partial x_j}\right|_{x_0} dx_j + ..., \tag{3.1}$$

with $i, j = 1, 2, 3$. The first term of the right hand side of equation 3.1 represents the rigid body motions $u_i(x_0)$, the second term represents the relative displacement in terms of the gradient of displacement $\partial u_i/\partial x_j$. The partial derivatives $\partial u_i/\partial x_j$ make up the displacement gradient tensor consisting of nine independent components:

$$\frac{\partial u_i}{\partial x_j} = \begin{pmatrix} \partial u_1/\partial x_1 & \partial u_1/\partial x_2 & \partial u_1/\partial x_3 \\ \partial u_2/\partial x_1 & \partial u_2/\partial x_2 & \partial u_2/\partial x_3 \\ \partial u_3/\partial x_1 & \partial u_3/\partial x_2 & \partial u_3/\partial x_3 \end{pmatrix}. \tag{3.2}$$

The displacement gradient tensor in equation 3.2 can be separated into a symmetric part, represented by the strain tensor ϵ_{ij}, and in an antisymmetric part, represented by the rotational motion components ω_{ij}. This separation then yields:

$$u_i(x) = \underbrace{u_i(x_0)}_{\text{rigid body translations } u_i(x_0)} + \underbrace{\frac{1}{2}\left(\frac{\partial u_i}{\partial x_j} + \frac{\partial u_j}{\partial x_i}\right) dx_j}_{\text{strain tensor } \epsilon_{ij}} + \underbrace{\frac{1}{2}\left(\frac{\partial u_i}{\partial x_j} - \frac{\partial u_j}{\partial x_i}\right) dx_j}_{\text{rotations } \omega_i}. \tag{3.3}$$

Therefore a complete description of the seismic wave field, according to Aki and Richards (2002), is given by:

- Three components of translational motions (u_1, u_2, u_3).

- Six components of strain $(\epsilon_{11}, \epsilon_{22}, \epsilon_{33}, \epsilon_{12}, \epsilon_{13}, \epsilon_{23})$.

- Three components of rotation $(\omega_1, \omega_2, \omega_3)$.

The components of rigid body translations have routinely been measured and investigated to obtain information about the seismic wave field. The three components of translational ground displacement (respectively ground velocity or acceleration) are measured using classic inertial seismometers. In addition, it is possible to record the strain deformations in the Earth's subsurface using strain meters (Gomberg and Agnew, 1996), but these measurements are not as common. The third quantity, the three components of rotational motion, on the other hand, is extremely difficult to measure, mainly due to the low sensitivity of the rotational motion sensors. It was also assumed that rotation amplitudes are very small, even in the vicinity of seismic faults (Bouchon and Aki, 1982), this fact complicates the measurement of the rotational motions. Today there is growing evidence that rotational motion amplitudes in the near-, as well as in the far-field, might have been underestimated. The lack of instrument sensitivity was overcome with the development of high quality rotational motion sensors, such as ringlaser gyroscopes. This allows to record the the rotational motions in the seismic wave field induced by earthquakes (Igel et al., 2007) or even by ambient seismic noise, for example oceanic microseisms (Hadziioannou et al., 2012). In this study two different

rotational motion sensors are used: the high quality one-component ringlaser gyroscope located at the geodetic Fundamentalstation in Wettzell, Germany (section 3.2) and the portable three-component rotational motion sensor Eentec R2 (section 3.2 and 3.4).

Rotational motions can provide independent information about wave propagation in the Earth's subsurface. Of particular interest are rotational motions around the vertical axis observed in the P-wave coda, as they can only be excited by horizontally polarized shear waves and not by compressional waves. These direct observations of rotational motions in the teleseismic P-coda were for example reported by Igel et al. (2007) and Pham et al. (2009a). It was pointed out by Igel et al. (2007), that P- and Rayleigh-waves at the surface can lead to tilting effects and therefore pollute the rotational motion measurements. The tilt signal can roughly be estimated from the vertical translational motions, but its contribution to the rotations is small in comparison to the noise level of the rotational motion sensors, in this case the ringlaser gyroscope (Pham et al., 2009b), and far below the detected signal. Another possible, and very likely, explanation of the observed rotations is the conversion from P- to SH-energy at 3D-heterogeneities in the vicinity of the receiver, that means in the crustal structure below the receivers.

3.2 Rotational motion sensors

This section introduces the rotational motion sensors used in this study, the ringlaser gyroscope and the R2 rotational motion sensor. Additionally, a short overview of other existing rotational motion sensors is given.

Ringlaser gyroscope

The ringlaser gyroscope (figure 3.2), located at the geodetic observatory in Wettzell in south-east Germany, is operated by the Federal Agency for Cartography and Geodesy. The main task of the instrument was to continuously measure the Earth's rotation rate with high accuracy. After discovering its potential for the use in the field of seismology, the equipment was upgraded to satisfy the seismological data acquisition needs. The instrument is a one-component recording device, which measures the rotation rate around the vertical axis only. The sensor itself is installed in a 5 m deep underground laboratory to shield it from pressure and temperature variations and to tightly couple it to underground. The ringlaser is an active, optical interferometer with two laser beams circulating in opposite directions around a closed cavity. As the speed of light is equal for the two beams in both directions, the rotation of the instrument in space causes a changing interference pattern leading to amplitude changes in the measurement cell with a characteristic frequency. The Sagnac beat frequency δf of the two light beams

Figure 3.2: Ringlaser gyroscope in Wettzell. The sensor is installed at the geodetic observatory and measures changes in the rotation rate due to changes in the Earth's rotation or due to seismic waves (Wettzell, 2015). Clearly visible are the four sides of the cavity, hosting the counter propagating laser beams, with a length of 4 m each. This results in a sensor surface of 16 m^2 and a perimeter of 16 m.

is given as

$$\delta f = \frac{4A(\mathbf{n} \cdot \dot{\mathbf{\Omega}})}{\lambda P},\tag{3.4}$$

with A being the surface area within the ringlaser, $\mathbf{n}$ is the surface normal, $\dot{\mathbf{\Omega}}$ is the rotation rate, λ the wavelength of the laser and P being the perimeter of the instrument. As an optical instrument the sensor has a flat response over the entire frequency range, which allows simultaneous observations of the long period Earth's rotations as well as of rotations induced by the high frequency seismic wave field. A change in the beat frequency δf can be caused by several effects (Igel et al., 2007):

(1) Variations of the scaling factor $4A/(P\lambda)$ will lead to changes in the beat frequency δf. This effect is minimized by temperature and pressure shielding of the instrument and an extremely low expansion coefficient of the device.

(2) Variations in δf can be caused by changes in the surface normal $\mathbf{n}$ of the ringlaser with respect to the rotation axis of the Earth. These variations can for example be caused by solid earth tides, ocean loading (Schreiber et al., 2009) or by diurnal polar motions (Schreiber et al., 2004).

(3) Changes in the rotation rate $\dot{\mathbf{\Omega}}$ itself can lead to variations in δf. These variations can be caused by changes in the Earth's rotation rate as a consequence of mass

redistribution or may also be seismically induced (earthquakes, ambient seismic noise).

(4) Rigid body motions also influence the rotation rate in the form of tilting effects, but as mentioned in section 3.1, these variations are negligible.

The ringlaser in Wettzell is a He-Ne laser with a wavelength λ of 633 nm. The surface area A measures 16 m^2 with a perimeter of 16 m. The instrument is mounted in a horizontal plane at ∼49.15°N latitude. The resulting Sagnac frequency for these parameters and location is 348.6 Hz. The measurement sensitivity strongly increased after an upgrade and improvement of the sensor equipment in August 2009 (mirror replacement) down to 10^{-12} rad/s. For more information and details on the Wettzell ringlaser the reader is referred to Schreiber et al. (2004).

Eentec R2 rotational motion sensor

The Eentec R2 rotational motion sensor (figure 3.3) is an electrochemical transducer. The transducer itself is contained in a channel filled with a specifically prepared electrolytic solution. It is made up by four fine platinum mesh electrodes (two anodes, two cathodes). Those electrodes are separated by thin microporous spacers (Eentec, 2015a). For a sketch of the sensor cell interior see figure 3.4.
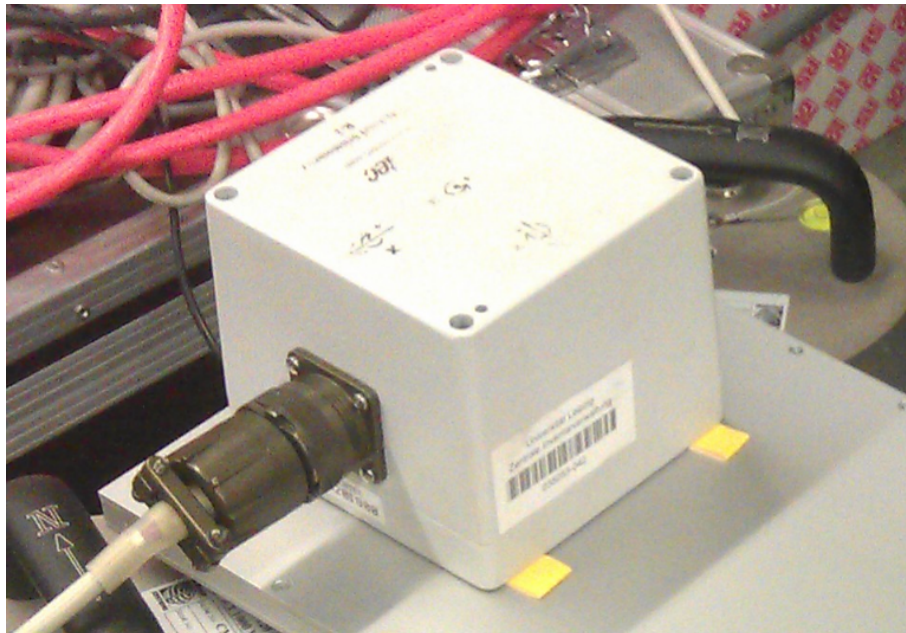
Figure 3.3: R2 sensor housing. The sensor housing measures 158×158×100 mm with a total weight of 1.5 kg, which makes it easily portable. The device can be set up in any position and is shown here during laboratory testing at the GFZ Potsdam, Germany.

The fluid motion in the channel is measured by converting the motion of the electrolyte to an electric signal. This is achieved by using the convective diffusion of the ions in the electrolyte solution. The current of the ions through the transducers strongly depends on the viscosity of the fluid, which depends on temperature. Following specifications
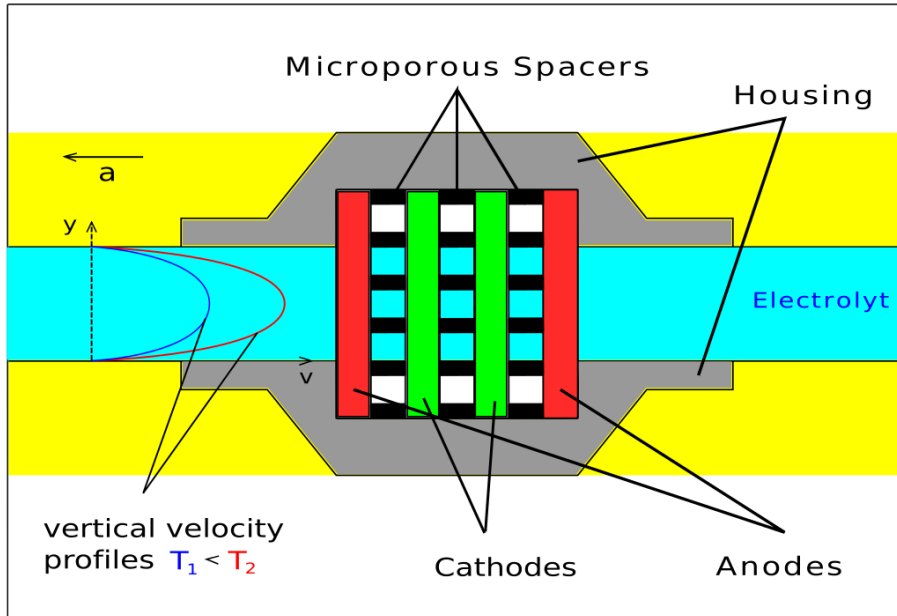
Figure 3.4: Sketch of the R2 sensor inside. Electrochemical device with a channel filled with a electrolytic solution. Through convective diffusion of the ions the fluid motion is converted to an electric signal, which is proportional to the rotation rate of the sensor. Figure from Bernauer et al. (2012).

are taken from the R2 instruction manual (Eentec, 2015b). The sensor is a three-component device with the orthogonal axes in the directions X, Y and Z. The housing measures $158 \times 158 \times 100$ mm with a total weight of 1.5 kg. It covers a frequency range from 0.03– 50 Hz with a self noise level of 0.5 $\mu rad/s$ RMS. The generator constant is 50 Vs/rad and the operating temperature range is -15°C to 55°C. The resolution of the instrument is 0.5E-7 rad/s on all axes. For sensor testing, installation and a data example see section 3.4.

Further rotational motion sensors

Only the two sensors, the ringlaser and the R2 sensor, are utilized in this study. For completeness a brief overview of further available rotational motion sensors is given.

Eentec R1 sensor

This sensor is the predecessor of the R2 rotational motion sensor. It is based on a similar operating technique as the R2 sensor, an electrochemical method. The main

difference between the two instruments is the lower sensitivity of the R1 sensor in comparison to the R2 sensor.

Rotaphone sensor (Brokešová et al., 2012; Brokešová and Málek, 2013)

This sensor operates with a mechanical technique and is based on the measurement of differential motions between paired geophones which are attached to a rigid body (see figure 3.5). The same differential velocity, and consequently the rotation rate, is obtained by multiple geophone pairs simultaneously and therefore allows in-situ calibration and cross-checking of the individual sensor pairs. The sensor is characterized by a nearly flat frequency response between 2 and 200 Hz and a measurement sensitivity of 10^{-8} rad/s. It was originally designed for prospecting purposes, but for example demonstrated its potential to record earthquake induced rotation rates in the order of 10^{-6} rad/s or rotation rates from blasts with amplitudes in the order of 10^{-7} rad/s.

LCG-Demonstrator fiber optic device

This device is manufactured by Northrop Grumman LITEF and is a first demonstrator of a new rotational motion sensor product specifically adapted to the needs of seismology and civil engineering. Information about this device are from Bernauer et al. (2012). In principle the sensor is a portable fiber optic gyro with the same operating principle as the Wettzell ringlaser. It has a lower self-noise level of 0.2 μrad/s (at 0.1 Hz) in comparison to the electrochemical sensors R1 and R2. As it is an optical instrument, it has a flat response over the entire frequency band, limitations in the frequency range can be caused by the data acquisition system.

Further ringlaser gyroscopes

In addition to the Wettzell ringlaser, several similar optic sensors are operated at permanent observatories, also measuring the rotation rate around the vertical axis. This includes the ringlaser at the Pinon Flat observatory, USA (Schreiber et al., 2009), the rotational motion sensor deployed in Christchurch, New Zealand (McLeod and Stedman, 1998) as well as the ringlaser in Arkansas, USA (Dunn et al., 2009). A further sensor, which in contrast measures the rotational motions around a horizontal axis, is installed and under development at the Virgo site, Italy and is described by Belfi et al. (2012).

3.3 Possible applications and data examples of rotational motions

Some examples for the use of rotational motions in the field of seismology are given in section 3.3.1. A data example from the Wettzell ringlaser is shown in section 3.3.2.
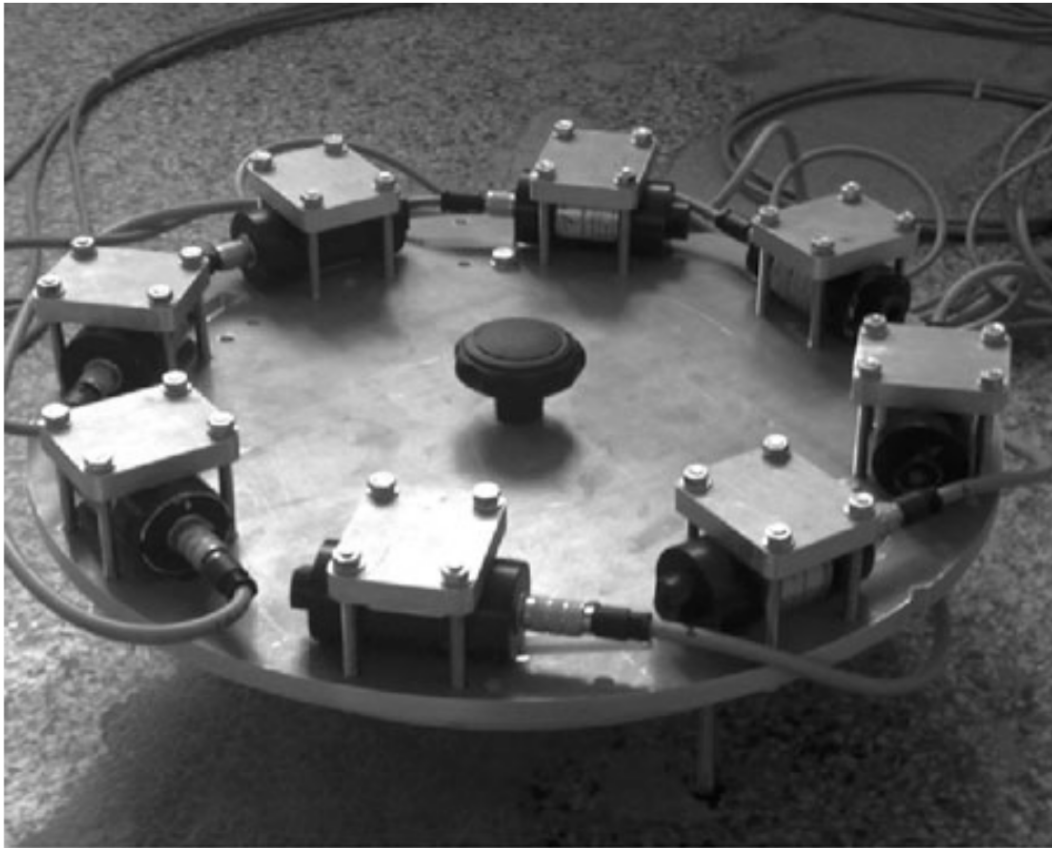
Figure 3.5: Rotaphone rotational motion sensor. This device is a mechanical sensor system based on the measurement of differential motions between paired geophone pairs. The geophone pairs (four in the image) are attached to a rigid body. The use of multiple geophone pairs allows for in situ calibration of the geophones as well as for cross-checking between the individual pairs. In this setup the sensor would measure the rotation rate around the vertical axis. Figure from Brokešová et al. (2012).

3.3.1 Possible applications of the use of rotational motions

Some possible applications arise from the use of rotational motions additionally to the commonly used translational motions.

Strong motion seismology

In the field of strong motion seismology the horizontal components of the rigid body translations are often contaminated by tilt. This tilting signal can directly be measured as rotational motion around the horizontal axes. To correct for this unwanted signal, collocated measurements of three translational and three rotational components can be used to correct the translational motions and derive the true point motion (see for

example van Driel et al. (2012)).

Incorporation into the seismic inverse problem

Bernauer et al. (2012) introduced a new technique to incorporate the rotational ground motions into the seismic inverse problem. This incorporation results in an improvement of tomographic resolution in the vicinity of seismic stations.

Wave polarization filter

Rotational motions can be used to determine the content of S-energy in the seismic wave field, as they are only sensitive to shear waves. Further it is possible to discriminate between SV- and SH-energy using three-component rotational motion records. While the rotations around the vertical axis can only be excited by horizontally polarized S-waves (SH), the rotations around the two horizontal axes can only be generated by vertically polarized S-waves (SV).

Relationship between rotation rate and transverse acceleration

An additional application arises from a well-known relation between the rotation rate around the vertical axis and the transverse acceleration. Under the assumption of a horizontally polarized plane wave, the vertical rotation rate $\dot{\Omega}_z$ and the transverse acceleration a_t should at all times be in phase. From the definition of the rotation rate $\dot{\Omega} = 0.5 \nabla \times \mathbf{v}$, with $\mathbf{v}$ being the ground velocity, it can easily be derived that the relation between $\dot{\Omega}_z$ and a_t is given as $a_t = -2c\dot{\Omega}_z$, c represents the phase velocity in the investigated frequency band. This relation can be used to directly compute phase velocities and source directions from point-like, collocated measurements of rotational and translational motions. This approach was for example used by Igel et al. (2007), Stupazzini et al. (2009), Kurrle et al. (2010) and Hadziioannou et al. (2012).

3.3.2 Rotational motion data example

Figure (figure 3.6) shows examples of seismically induced rotation rates around the vertical axis observed with the ringlaser in Wettzell. Left side of the figure shows a regional event, the right side shows records of a teleseismic earthquake. The top three rows represent the three components of translational motion in up-down (TZ), north-south (TN) and east-west (TE) direction. Bottom row shows the rotation rates around the vertical axis (RZ). The regional earthquake occurred on August 26th 2011 in the Vogtland region with a magnitude M_L of 3.6. A clear increase in rotational motion energy is visible after the passage of the direct S-wave. Amplitudes in this distance range ($\sim$130 km) are in the order of 10 nrad/s for the rotational motions. The teleseismic event has a moment magnitude of 6.7 and occurred in the Sea of Okhotsk region on May 24th 2013 in a depth of 629 km. A clear increase in rotational motion energy can be observed after the passage of the P- and PcP-phases. The origin of the rotational motion energy is discussed in chapter 8.
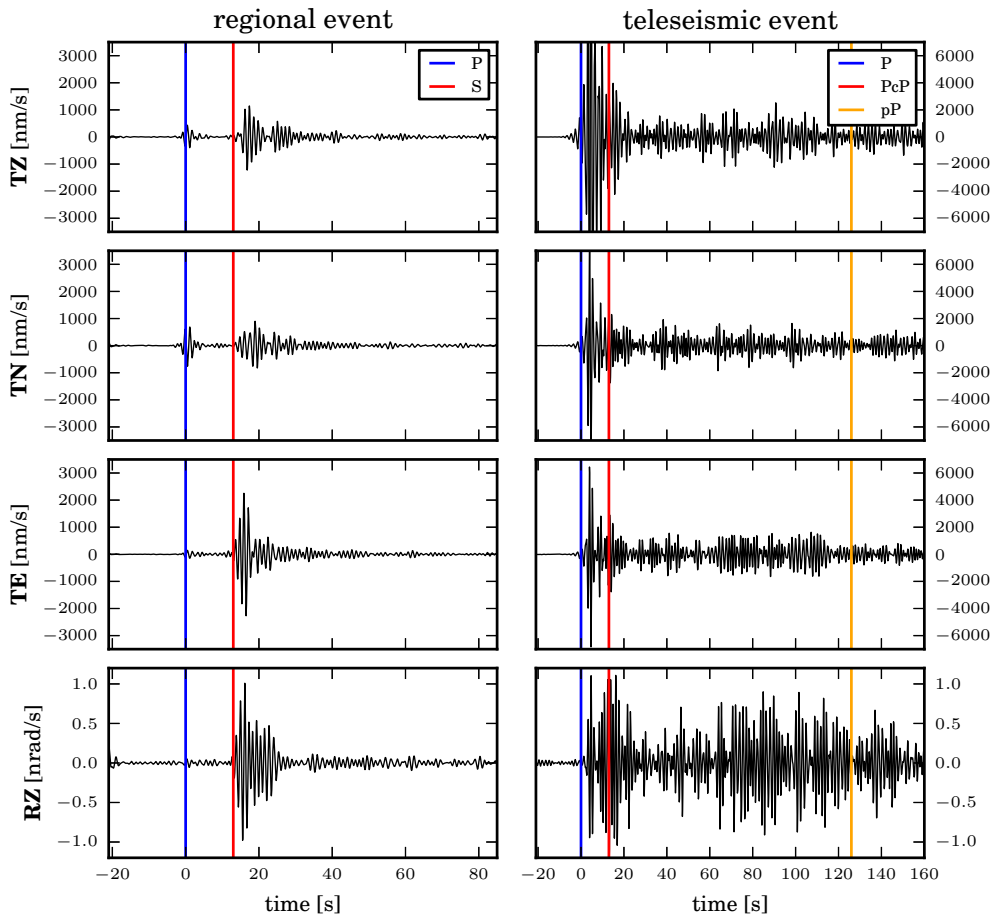
Figure 3.6: Example for rotational motions. Top three traces show measured ground velocities in vertical (TZ), north-south (TN) and east-west (TE) direction for a regional (left) and a teleseismic (right) event. A bandpass filter with center frequency of 1 Hz is applied. Bottom trace shows the observed rotation rates around the vertical axis (RZ). Colored vertical lines indicate arrivals of primary waves. Note the clear increase in rotational motion amplitude after the direct P-wave arrival in the teleseismic event.

3.4 Testing and installation of the R2 rotational motion sensor

In addition to the ringlaser gyroscope detailed in section 3.2, it was intended to install and use the R2 sensor (section 3.2) in this study to particularly record rotational motions from local and regional seismic events. Prior to the installation of the sensor at the site WERN (Wernitzgrün) in Germany (50.287°N 12.376°E), the sensor was subject to laboratory tests at the LMU Munich and the GFZ Potsdam for investigating its recording properties.

The first test took place at the LMU Munich and was carried out and described by

Bernauer et al. (2012). For the test and calibration a Lennartz step table and a tilt bridge were used. This setup is normally used for the calibration of standard inertial seismometers. The tests focused on the sensor generator constant as a function of temperature and on the self-noise of the sensor. The main outcomes and conclusions of the LMU Munich tests are summed up in the following lines:

- The generator constant of the sensor deviates up to 18 % from the nominal value of 50 V/rad/s in a temperature range from $20°\,C$ to $50°\,C$.

- The self-noise amplitudes are in the order of 10^{-7} rad/s in the 10 to 100 s period band. This value is too high for seismic weak motion applications. For example the sensor would not have recorded the 2011 Tohoku earthquake in Wettzell due to its low sensitivity.

- The self noise is increasing with increasing frequency.

Figure 3.7: Laboratory test of the Eentec R2 rotational motion sensor. Comparison of the rotational motion sensor R2 (right) with a Nanometric Trillium seismometer (left). The seismometer is placed on a Lennartz step table, the R2 sensor is located on a bridge with arm length of 396.5 mm. In this test the generator constant and the phase shift for the different axes of the R2 sensor in multiple frequency bands are determined.

The second experiment was carried out at the GFZ Potsdam. A similar setup to the one in Munich was used (figure 3.7). Different movements (steps, sinusoidal movements) were simulated using a Lennartz step table with an attached tilt bridge. This tests focused on the frequency dependence of the sensor generator constant and the phase shift of the sensor at constant temperature. Investigations of the generator constant and the phase shift were carried out in frequencies between 0.1 and 10 Hz. The measurements were compared to the nominal values from the manufacturers manual (Eentec, 2015b) (figure 3.8). From the tests following conclusions can be drawn:

- The generator constant at room temperature is relatively stable throughout the investigated frequencies for all three axes.

- The measured generator constant values deviate significantly from the nominal values given in the user manual (Eentec, 2015b).

- Significant phase shifts of the sensor are observable for frequencies below 1 Hz.
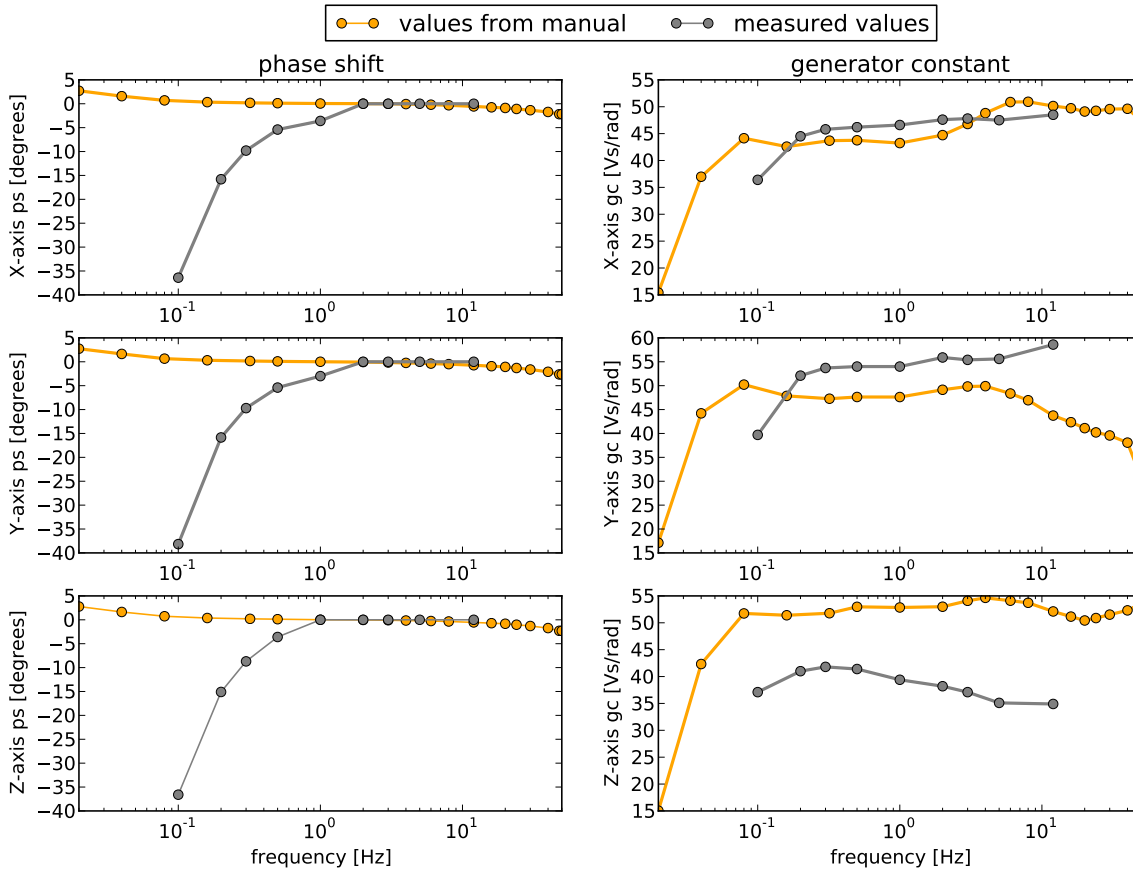
Figure 3.8: Measured and theoretical phase shifts (ps) and generator constants (gc) of the R2 sensor. Phase shift (left column) and generator constant (right column) for the three different axes X, Y and Z of the sensor (from top to bottom row). Orange colors indicate values taken from the manufacturer product manual (Eentec, 2015b), grey values indicate values measured in the laboratory experiments. The phase shift of the instrument can be reproduced quite well for the three axes in the investigated frequency bands greater than 1 Hz. The generator constant, especially for the Z-axis, shows strong deviations from the nominal values, but is nearly constant over the entire investigated frequency band.

After the laboratory tests, the sensor was installed at the station WERN collocated to a three-component seismometer as part of the Saxonian seismic network (SX). Continuous data from the sensor was available, although no earthquake or other events (for
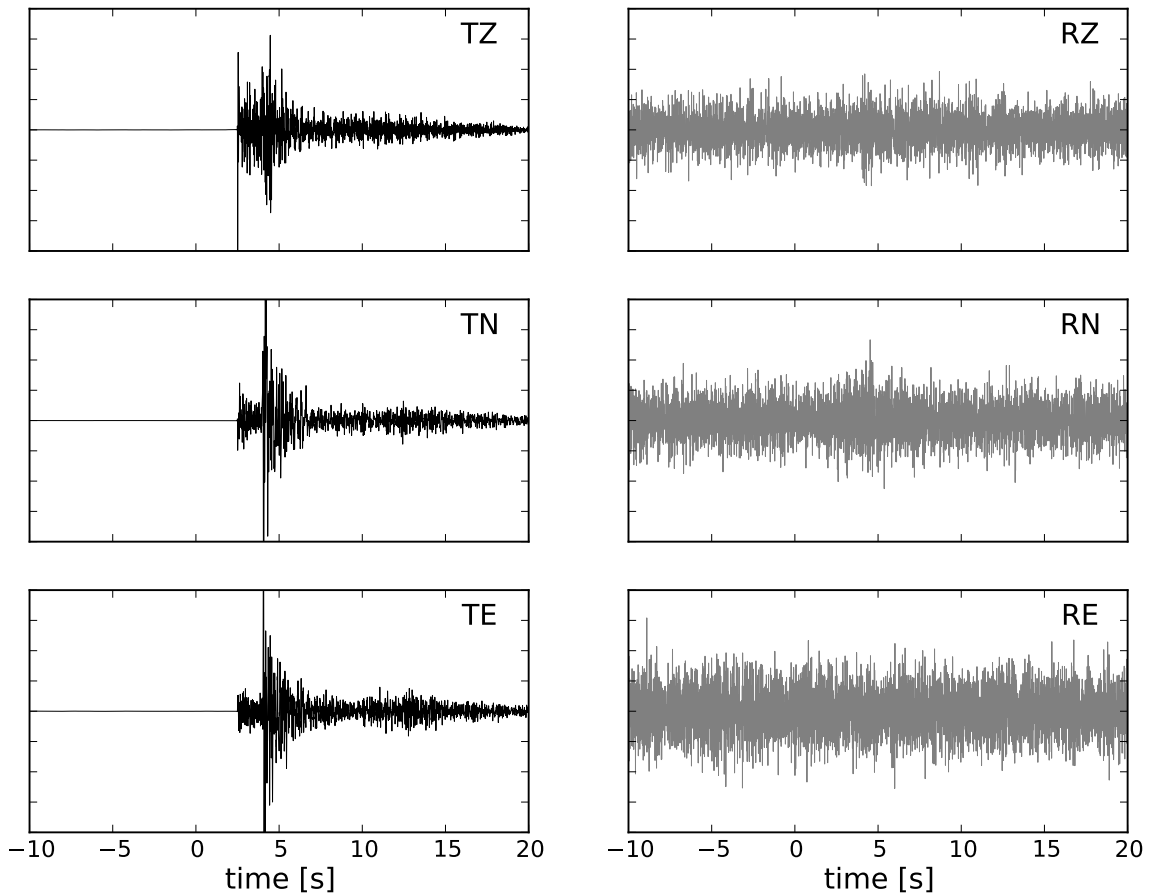
Figure 3.9: Local event in the Vogtland region recorded at station WERN. Records of a regional earthquake (2013-01-01 18:20:12 UTC) that occurred in the Vogtland region with a magnitude M_L of 2.2. It was recorded at the station WERN (Wernitzgrün). Event depth was 9.8 km, epicentral distance to the receiver was less than 10 km. Left three traces (black) show the translational velocity records in vertical (TZ), north-south (TN) and east-west (TE) direction. Right three traces represent the rotational motion rates around the three axes (RZ, RN, RE). No event is visible in the rotational motion records due to the low sensitivity of the rotational motion sensor.

example quarry blasts) were recorded during the testing period. For a data example see figure 3.9.

From the figure it is clear, that it was not possible to record rotational motions even from very close earthquakes of magnitudes up to 3. This is due to the lack of measurement sensitivity of the R2 sensor. Therefore, for this study, only the high quality ringlaser in Wettzell will be used. Sensitivity of portable rotational motion sensors has to be improved to make the sensors usable in weak motion seismology applications, however sensor sensitivity may be sufficient for strong motion engineering purposes.

4 Radiative transfer approach to translational and rotational motions

MC solutions to the elastic radiative transfer equations (RTE) are used to simulate multi-component seismogram envelopes of translational and rotational motions. Multiple anisotropic scattering following the Born approximation in a heterogeneous medium with deterministic macroscopic background structure is assumed. Additionally, to estimate crustal attenuation parameters in a local framework, acoustic RTT is used in section 6.

At first an introduction to RTT in seismology in general is given in section 4.1. Acoustic RTT is introduced in section 4.2, details about the elastic radiative transfer approach are presented in section 4.3. Solutions to the elastic RTEs using MC techniques are discussed in section 4.4. A brief description and the key features of the simulation algorithm are given in section 4.5. In section 4.6 the simulation of multi-component translational and rotational seismogram envelopes using elastic RTT is explained, followed by the simulation procedure for modeling seismic wave arrivals from local, regional and teleseismic events in section 4.7.

4.1 Radiative transfer theory in seismology

A suitable and one of the most common methods to describe the propagation of seismic energy in a scattering medium is the RTT. The RTEs have first been introduced by Chandrasekhar (1960) in the context of atmospheric sciences to describe the propagation of light through a turbulent atmosphere and were only later introduced to the field of seismology. The central quantity of the RTT is the specific intensity $I(\mathbf{n}, \mathbf{r}, t)$. It describes the angularly resolved energy flux from a radiating surface located at position $\mathbf{r}$ into an unit solid angle around direction $\mathbf{n}$ at time t. Phenomenologically the transport problem can be regarded as a conservation of energy as illustrated in figure 4.1.

In the acoustic case the change of intensity along an infinitesimal path element δs is
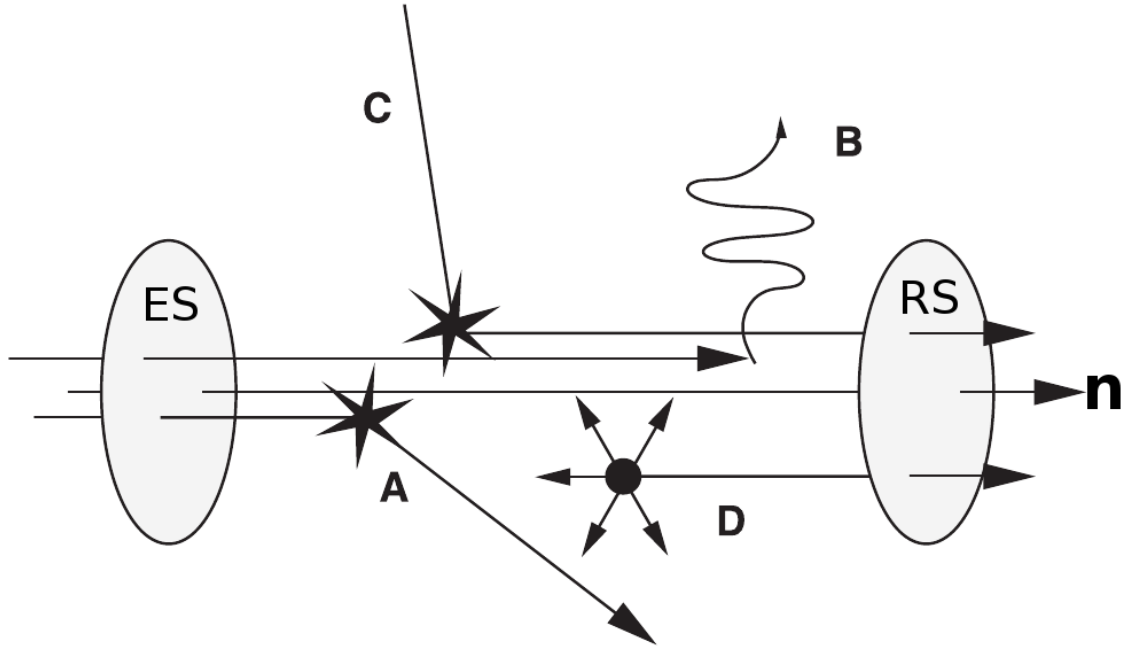
Figure 4.1: Conservation of energy in the RTT. Energy flux from an emitting surface (ES) into a receiving surface (RS) around a direction **n**. Flux reduction by scattering in other directions (A) and by dissipation (B). Flux increase by scattering from other directions into direction **n** (C) and from additional sources (D) along the path. Figure redrawn from Sens-Schönfelder et al. (2009).

given by:

$$\frac{\delta}{\delta s}I(\mathbf{n},\mathbf{r},t) = -(g_0 + b)I(\mathbf{n},\mathbf{r},t) + \int_{4\pi} g(\mathbf{n}',\mathbf{n})I(\mathbf{n}',\mathbf{r},t)d\Omega_{n'}. \tag{4.1}$$

The incident direction is described by the unit vector **n**, all other directions are indicated by **n**'. Scattering of energy away from direction **n** is described by the parameter g_0, the scattering from all other directions **n**' into direction **n** is given by $g(\mathbf{n}',\mathbf{n})$. The parameter b describes the absorption of energy (intrinsic attenuation). A reduction of intensity can therefore be achieved by scattering of energy away from direction **n** and by dissipation or absorption. A flux increase can result from scattering from other directions **n**' into direction **n** or from additional sources along the path. The specific intensity I is related to the local, angularly-resolved energy density $a(\mathbf{n},\mathbf{r})$:

$$a(\mathbf{n},\mathbf{x}) = \frac{1}{v}I(\mathbf{n},\mathbf{r}). \tag{4.2}$$

Here v denotes the velocity of the particle/ray. In this study it is assumed, that the specific intensity I depends on time and also on frequency. This assumption is true,

due to the fact, that energy transport in seismology is always a non-stationary problem and the random medium is static. This fact leads to a conservation of frequency along the ray (Sens-Schönfelder et al., 2009).

As mentioned in section 2.1 first and simplest approaches assume single, isotropic scattering of acoustic energy, while more sophisticated models describe multiple anisotropic scattering of elastic energy. The approach used here is based on the assumption of multiple anisotropic scattering of elastic waves at randomly distributed small-scale heterogeneities in a deterministic macroscopic structure and is based on an algorithm detailed by Sens-Schönfelder et al. (2009). The algorithm is extended here to model multi-component seismogram envelopes of translational and rotational motions for sources with different epicentral distances (local, regional and teleseismic).

4.2 Acoustic radiative transfer theory

In addition to elastic RTT, the method of acoustic energy transfer is used in the framework of the local data set investigations in chapter 6 to estimate crustal intrinsic and scattering attenuation parameters. This approach to model the energy density is similar to the one described by Sens-Schönfelder and Wegler (2006). In this method only the acoustic transport of energy is modeled, that indicates only the propagation of seismic shear energy in considered in the model. The radiative transfer of P-energy and consequently conversions from P- to S-energy and vice versa are not included in this approach. In the approach, multiple scattering is considered under the assumption of isotropic scattering, meaning that there is no preferred direction of scattering at the medium heterogeneities. In the simulations the energy propagation is modeled in a half space medium with an isotropic shear wave source. To be able to model the energy transfer in half space, first the energy transfer in full space has to be considered. This is given by the energy density Green's function in full space $G_f(\mathbf{r}, t)$ detailed by Sato et al. (2012):

$$G_f(\mathbf{r}, t) = F(\mathbf{r}, t) + v_0 g_0 \int_{-\infty}^{\infty} dt' \int \int \int d\mathbf{r}' F(\mathbf{r} - \mathbf{r}', t - t') G_f(\mathbf{r}', t'). \qquad (4.3)$$

The function $F(\mathbf{x}, t)$ is defined as the Green's function of the coherent wave energy and is given as:

$$F(\mathbf{r}, t) = \frac{1}{4\pi v_0 r^2} H(t) \delta\left(t - \frac{r}{v_0}\right) e^{-v_0 g_0 t}. \qquad (4.4)$$

v_0 indicates the average S-wave velocity, g_0 is the total scattering coefficient. H is the Heaviside function and r indicates the distance from source to receiver. In the modeling an analytic approximation to equation 4.3, given by Paasschens (1997), is used. This approximation is derived from comparisons of solutions of the Boltzmann equation in

a 2D and 4D isotropic scattering media and yields in full space

$$
\begin{aligned}
G_f(\mathbf{r}, t) \simeq{} & \frac{e^{-g_0 v_0 t}}{4\pi v_0 r^2} \delta\left(t - \frac{x}{v_0}\right) + \frac{(1 - r^2/(v_0^2 t^2))^{1/8}}{(4\pi v_0 t/(3g_0))^{3/2}} \\
& \times e^{-g_0 v_0 t} M\left(g_0 v_0 t \left(1 - \frac{r^2}{v_0^2 t^2}\right)^{3/4}\right) H\left(t - \frac{r}{v_0}\right),
\end{aligned}
\tag{4.5}
$$

where the function $M(x) \simeq e^x \sqrt{1 + 2.026/x}$. According to Sens-Schönfelder and Wegler (2006) the deviation of equation 4.5 from the exact solution given in equation 4.3 is below 5 %. Larger perturbations only occur in the tail of the direct S-wave. For purposes of this study this deviations are acceptable as only the average value in a time window around the direct wave is used. The energy in this time window mainly consists of unscattered energy. This energy content is described correctly in equation 4.5. In the simulations a half space model is used including the free surface condition. As equation 4.5 is valid for a full space medium, a correction for the free surface is necessary. At the free surface the vertical and horizontal component mean square envelopes show different amplification rates in comparison to the envelopes simulated in a full space medium. According to a study by Emoto et al. (2010) a factor of four is a good approximation for the amplification rates of both the vertical and the horizontal components. Furthermore corrections for the source energy W as well as for the site response at the receiver R have to be applied to the Green's function $G_f(\mathbf{r}, t)$. Intrinsic attenuation is accounted for by multiplication with a time dependent factor of the form e^{-bt}. b is the attenuation coefficient defined as

$$
b = 2\pi f/Q^i,
\tag{4.6}
$$

with f being frequency, Q^i is the intrinsic quality factor. The final modeled energy density $E(\mathbf{r}, t)$ is given by:

$$
E(\mathbf{r}, t) = 4WR G_f(\mathbf{r}, t) e^{-bt}.
\tag{4.7}
$$

The main drawback of the acoustic simulations is, that it is only possible to model the propagation of S-wave energy, therefore not considering P-energy transport. Furthermore, due to the assumption of isotropic scattering, forward scattering cannot be included and modeled in the simulations.

4.3 Elastic radiative transfer equations

Since the 1960s the theory of radiative transfer developed without any rigorous connection to the physics of seismic waves and was solely based on the energy balance consideration (figure 4.1). The contributions by Weaver (1990) and Turner and Weaver (1994), as well as the linking of local angularly-resolved energy density and the wave

equations, lead to the derivation of the RTEs from the elastic wave equation for waves in a random medium (Ryzhik et al., 1996). These transfer equations not only include the description of S-energy propagation, but also contain the propagation of P-energy and the coupling between these two modes through conversion processes (for example scattering events or reflections at interfaces). The elastic transport equations are a system of two coupled integro-differential equations for the P- and S-intensities. For the S-intensity this is represented by a 2×2 coherence matrix. The coherence matrix $\hat{I}$ for the two possible S-wave polarizations is defined according to Apresyan and Kravtsov (1996) by

$$\hat{I} = \begin{bmatrix} I_{\theta\theta} & I_{\theta\phi} \\ I_{\phi\theta} & I_{\phi\phi} \end{bmatrix} = c' \begin{bmatrix} \langle A_\theta A_\theta^* \rangle & \langle A_\theta A_\phi^* \rangle \\ \langle A_\phi A_\theta^* \rangle & \langle A_\phi A_\phi^* \rangle \end{bmatrix}, \tag{4.8}$$

with θ and ϕ referring to unit vectors in the directions of the angles θ and ϕ in a spherical coordinate system and c' being a proportionality coefficient. The angles and the coordinate system are illustrated in figure 4.2. A_θ and A_ϕ are the components of
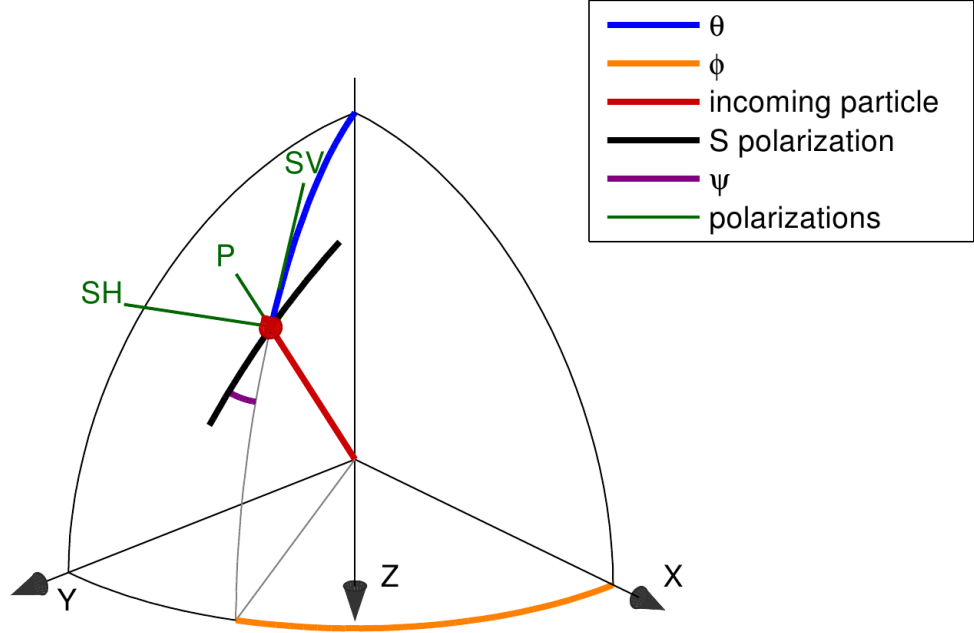
Figure 4.2: Illustration of relevant angles and directions. Red arrow represents the propagation direction of the particle, with θ (blue) being the particle direction measured from upwards to downwards and ϕ (orange) being the particle direction measured from north to east. Black line indicates the polarization of the S-particle. The polarization angle ψ (purple) is measured between the polarization direction and the vertical plane. Green lines represent the polarization directions P_P, P_{SV} and P_{SH}.

the S-wave polarization amplitudes. The complex conjugate amplitudes of a S-wave propagating in directions θ and ϕ are given as A_θ^* and A_ϕ^*. A proportionality factor c is introduced to account for the local elastic medium properties. The coefficient c is

defined as

$$
\mathbf{c} =
\begin{bmatrix}
c_1 & 0 & 0 & 0 & 0 \\
0 & c_2 & 0 & 0 & 0 \\
0 & 0 & c_3 & 0 & 0 \\
0 & 0 & 0 & c_4 & 0 \\
0 & 0 & 0 & 0 & c_5
\end{bmatrix},
\tag{4.9}
$$

with $c_1 = \rho\omega^2 v_p/2$ and $c_{2\ldots5} = \rho\omega^2 v_s/2$. Here ρ describes the local density and ω is the angular frequency of the wave field. v_p and v_s are the P- and S-wave speed, respectively. The polarization can also be described by a Stokes vector $\mathbf{S}$ of elastic waves, that additionally to the two S-intensities contains the P-intensity (Turner and Weaver, 1994; Margerin et al., 2000). This vector contains a full description of the polarization state of seismic waves and is defined as

$$
\mathbf{S} =
\begin{bmatrix}
I_P \\
I_\theta^S \\
I_\phi^S \\
U \\
V
\end{bmatrix}
=
\begin{bmatrix}
I_P \\
I_{\theta\theta} \\
I_{\phi\phi} \\
I_{\phi\theta} + I_{\theta\phi} \\
i(I_{\phi\theta} - I_{\theta\phi})
\end{bmatrix}
= c
\begin{bmatrix}
\langle |A^P|^2 \rangle \\
\langle |A_\theta|^2 \rangle \\
\langle |A_\phi|^2 \rangle \\
2\Re\langle A_\theta A_\phi^* \rangle \\
2\Im\langle A_\theta A_\phi^* \rangle
\end{bmatrix},
\tag{4.10}
$$

with I^P, I_θ^S and I_ϕ^S denoting the intensities for the P-wave and the two polarizations of the S-waves, respectively. The parameters U and V can be expressed through the phase difference δ between the two different S-wave polarizations measured along the directions θ and ϕ. U and V are given as:

$$
U = 2c_4 \langle A_\theta A_\phi \cos\delta \rangle,
\tag{4.11a}
$$

$$
V = 2c_5 \langle A_\theta A_\phi \sin\delta \rangle.
\tag{4.11b}
$$

According to Sens-Schönfelder et al. (2009) the treatment of the polarizations in equation 4.10 can be restricted to linearly polarized waves due the character of a point shear dislocation and the structure of the scattering coefficients. A point shear dislocation source emits linearly polarized waves, the phase shift for the two different S-wave polarizations is therefore zero. Scattering events do also not cause a shift in phase. Under the assumption of linearly polarized waves, the V-component of the Stokes vector is zero (equation 4.11b). According to Apresyan and Kravtsov (1996) the U component of a polarized wave field can be expressed by

$$
(I_\theta^S + I_\phi^S)^2 = (I_\theta^S - I_\phi^S)^2 + U^2 + V^2.
\tag{4.12}
$$

Setting $V = 0$ in equation 4.12, U is simply defined in dependence of I_θ^S and I_ϕ^S. Due to the approximation of purely polarized waves, the transport equations for I_P, I_θ^S and I_ϕ^S can be written as a system of three coupled scalar equations (Apresyan and Kravtsov, 1996; Sens-Schönfelder et al., 2009). These equations describe a multi-mode system directly following a local energy conservation principle. The transport equations for I^P (equation 4.13a), I_θ^S (equation 4.13b) and I_ϕ^S (equation 4.13c) are consequently given

as:

$$\left(\frac{\partial}{v_p \partial t} + \mathbf{n} \cdot \nabla\right) I^P(\mathbf{n}, \mathbf{r}) = -\left(g_0^{PP} + g_o^{PS} + \frac{\omega}{v_p Q_P^i}\right) I^P(\mathbf{n}, \mathbf{r})$$

$$+ \int_{4\pi} g^{PP}(\Theta) I^P(\mathbf{n}', \mathbf{r}) d\Omega_{n'}$$

$$+ \int_{4\pi} g^{SP}(\Theta, \Phi_\theta) I_\theta^S(\mathbf{n}', \mathbf{r}) d\Omega_{n'}$$

$$+ \int_{4\pi} g^{SP}(\Theta, \Phi_\phi) I_\phi^S(\mathbf{n}', \mathbf{r}) d\Omega_{n'}, \qquad (4.13a)$$

$$\left(\frac{\partial}{v_s \partial t} + \mathbf{n} \cdot \nabla\right) I_\theta^S(\mathbf{n}, \mathbf{r}) = -\left(g_0^{SS} + g_o^{SP} + \frac{\omega}{v_s Q_S^i}\right) I_\theta^S(\mathbf{n}, \mathbf{r})$$

$$+ \int_{4\pi} g_l^{SS}(\Theta, \Phi_\theta) I_\theta^S(\mathbf{n}', \mathbf{r}) \cos^2(\psi) d\Omega_{n'}$$

$$+ \int_{4\pi} g_r^{SS}(\Theta, \Phi_\theta) I_\theta^S(\mathbf{n}', \mathbf{r}) \sin^2(\psi) d\Omega_{n'}$$

$$+ \int_{4\pi} g_l^{SS}(\Theta, \Phi_\phi) I_\phi^S(\mathbf{n}', \mathbf{r}) \cos^2(\psi) d\Omega_{n'}$$

$$+ \int_{4\pi} g_r^{SS}(\Theta, \Phi_\phi) I_\phi^S(\mathbf{n}', \mathbf{r}) \sin^2(\psi) d\Omega_{n'}$$

$$+ \int_{4\pi} g^{PS}(\Theta) I^P(\mathbf{n}', \mathbf{r}) \cos^2(\psi) d\Omega_{n'}, \qquad (4.13b)$$

$$\left(\frac{\partial}{v_s \partial t} + \mathbf{n} \cdot \nabla\right) I_\phi^S(\mathbf{n}, \mathbf{r}) = -\left(g_0^{SS} + g_o^{SP} + \frac{\omega}{v_s Q_S^i}\right) I_\phi^S(\mathbf{n}, \mathbf{r})$$

$$+ \int_{4\pi} g_l^{SS}(\Theta, \Phi_\theta) I_\theta^S(\mathbf{n}', \mathbf{r}) \sin^2(\psi) d\Omega_{n'}$$

$$+ \int_{4\pi} g_r^{SS}(\Theta, \Phi_\theta) I_\theta^S(\mathbf{n}', \mathbf{r}) \cos^2(\psi) d\Omega_{n'}$$

$$+ \int_{4\pi} g_l^{SS}(\Theta, \Phi_\phi) I_\phi^S(\mathbf{n}', \mathbf{r}) \sin^2(\psi) d\Omega_{n'}$$

$$+ \int_{4\pi} g_r^{SS}(\Theta, \Phi_\phi) I_\phi^S(\mathbf{n}', \mathbf{r}) \cos^2(\psi) d\Omega_{n'}$$

$$+ \int_{4\pi} g^{PS}(\Theta) I^P(\mathbf{n}', \mathbf{r}) \sin^2(\psi) d\Omega_{n'}. \qquad (4.13c)$$

In equations 4.13a to 4.13c, Q_P^i and Q_S^i denote the intrinsic quality factor for P- and S-waves. Θ represents the scattering angle between incoming and outgoing direction $\mathbf{n}'$ and $\mathbf{n}$. Subscripts l and r distinguish between the two possible polarizations of the S-waves with respect to the scattering plane. r represents a polarization perpendicular to the scattering plane and l indicates a polarization parallel to the plane. The angle between polarization direction of the incident wave and the scattering plane (spanned by $\mathbf{n}$ and $\mathbf{n}'$) is given as Ψ. The differential solid angle is expressed through $d\Omega_{n'}$,

ω denotes the angular frequency of the wave field. g^{ij} and g_0^{ij} ($i, j =$P or S) are the scattering and total scattering coefficients following the Born approximation. These coefficients describe the scattering of energy in a heterogeneous medium. A derivation of these coefficients from the elastic wave equation in random elastic media is given by Sato et al. (2012). The scattering coefficients are determined using a random medium with continuous velocity and density variations with respect to a background model $(v_{p,0}, v_{s,0}, \rho_0)$. The assumption of proportional P- and S-wave speeds (Sato et al., 2012), as well as a linear relation between density and velocity (Birch, 1961) is used for the determination of the scattering coefficients. Due to these assumptions, the number of independent fluctuations of density and velocity is reduced to one spatially stationary random variable $\xi(\mathbf{x})$ (Przybilla and Korn, 2008), given by

$$\xi(\mathbf{x}) = \frac{\delta v_p}{v_{p,0}} = \frac{\delta v_s}{v_{s,0}} = \frac{1}{\nu}\frac{\delta \rho}{\rho_0}, \tag{4.14}$$

with ν ranging between 0.78 and 0.8 in standard lithosphere (Sato et al., 2012). The properties of the random medium are defined by an autocorrelation function R

$$R(\mathbf{x}) = \langle \xi(\mathbf{x} + \mathbf{x}')\xi(\mathbf{x}) \rangle \tag{4.15}$$

and the variance is given as:

$$\epsilon^2 = R(0) = \langle \xi(\mathbf{x})^2 \rangle. \tag{4.16}$$

The Fourier Transform of the autocorrelation function R at a certain wavenumber $\mathbf{m}$ yields the power spectrum of the medium $P(\mathbf{m})$ given as:

$$P(\mathbf{m}) = \int \int \int R(\mathbf{x})e^{-i\mathbf{m}\cdot\mathbf{x}}d\mathbf{x}. \tag{4.17}$$

For choices of different ACFs R and the corresponding PSD functions see section 2.2. The complete direction dependent Born scattering coefficients in spherical coordinates (Θ, Φ) are given by Sato et al. (2012):

$$g^{PP}(\Theta) = \frac{k_s^4}{4\pi}|X^{PP}(\Theta)|P\left(\frac{2k_s}{\gamma_0}\sin\left(\frac{\Theta}{2}\right)\right), \tag{4.18a}$$

$$g^{PS}(\Theta) = \frac{1}{\gamma_0}\frac{k_s^4}{4\pi}|X^{PS}(\Theta)|P\left(\frac{k_s}{\gamma_0}\sqrt{1 + \gamma_0^2 - 2\gamma_0\cos(\Theta)}\right), \tag{4.18b}$$

$$g^{SP}(\Theta, \Phi) = \gamma_0\frac{k_s^4}{4\pi}|X^{SP}(\Theta, \Phi)|P\left(\frac{k_s}{\gamma_0}\sqrt{1 + \gamma_0^2 - 2\gamma_0\cos(\Theta)}\right), \tag{4.18c}$$

$$g_l^{SS}(\Theta, \Phi) = \frac{k_s^4}{4\pi}|X_l^{SS}(\Theta, \Phi)|P\left(2k_s\sin\left(\frac{\Theta}{2}\right)\right), \tag{4.18d}$$

$$g_r^{SS}(\Theta, \Phi) = \frac{k_s^4}{4\pi}|X_r^{SS}(\Theta, \Phi)|P\left(2k_s\sin\left(\frac{\Theta}{2}\right)\right). \tag{4.18e}$$

The angle between the initial direction and the direction after scattering is given by Θ. Φ defines the angle between the polarization direction of the particle and the scattering plane. This scattering plane is spanned by the incident particle direction and the direction after the scattering event. The superscripts (P or S) give information about the type of scattering, a superscript of PS for example indicates the conversion scattering from P- to S-energy, a superscript of PP indicates scattering of P-energy without mode conversion. Scattering from P- to S-energy always creates polarizations in the scattering plane. k_s represents the S-wavenumber. Differences in the scattering pattern due to different medium heterogeneities are described through the PSD function P. For an isotropic elastic medium, according to Sato et al. (2012), the basic scattering patterns X are given as:

$$X^{PP}(\Theta) = \frac{1}{\gamma_0} \left[\nu \left(-1 + \cos(\Theta) + \frac{2}{\gamma_0^2} \sin^2(\Theta) \right) - 2 + \frac{4}{\gamma_0^2} \sin^2(\Theta) \right], \qquad (4.19a)$$

$$X^{PS}(\Theta) = -\sin(\Theta) \left[\nu \left(1 - \frac{2}{\gamma_0} \cos(\Theta) \right) - \frac{4}{\gamma_0} \cos(\Theta) \right], \qquad (4.19b)$$

$$X^{SP}(\Theta, \Phi) = \frac{1}{\gamma_0^2} \sin(\Theta) \cos(\Phi) \left[\nu \left(1 - \frac{2}{\gamma_0} \cos(\Theta) \right) - \frac{4}{\gamma_0} \cos(\Theta) \right], \qquad (4.19c)$$

$$X_l^{SS}(\Theta, \Phi) = \cos(\Phi) \left[\nu \left(\cos(\Theta - \cos(2\Theta)) \right) - 2\cos(2\Theta) \right], \qquad (4.19d)$$

$$X_r^{SS}(\Theta, \Phi) = \sin(\Phi) \left[\nu \left(\cos(\Theta) - 1 \right) + 2\cos(\Theta) \right]. \qquad (4.19e)$$

If a scattering event occurs, the probability distribution of the propagation directions after scattering is given by the scattering coefficients (equations 4.18). The total scattering coefficients g_0^{ij} are given as the integral over the scattering coefficients g^{ij} over the solid angle with i, j = P or S. The total scattering coefficients g_0^{ij} are defined according to (Sato et al., 2012):

$$g_0^{ij} = \frac{1}{4\pi} \oint g^{ij} d\Omega. \qquad (4.20)$$

The conversion mean free path l^{ij} is defined as the inverse of g_0^{ij} and represents the average distance a particle of type i has to travel until it is scattered into mode j. The total mean free path l^i of a particle with mode i is given by:

$$l^i = \left(\sum_j g_o^{ij} \right)^{-1}. \qquad (4.21)$$

4.4 Monte Carlo solutions to the transfer equations

Only in some special cases exact analytical solutions to the RTEs can be found, for example in the case of scalar waves or in the case of acoustic, isotropic scattering in full space (Zeng et al., 1991; Paasschens, 1997). For more complex scattering processes (for example anisotropic scattering following the Born approximation), elastic energy transport or complicated model structures (for example including a free surface or interfaces) it is difficult or not even possible to find analytical solutions to the RTEs for the modeling of seismic energy propagation. Instead the solutions are often based on numerical techniques, for example MC methods. In the field of seismology two different types of MC approaches are mainly used to solve the transport equations. The first one was introduced by Hoshiba et al. (1991) and can be referred to as a *probability summation method*. In this approach the seismic energy propagation is modeled by a number of particles propagating through the medium. At every single scattering event the probability for each single particle is calculated, that it is scattered towards a receiver in the medium. This probability is dependent on the scattering properties of the medium and the scattering angle towards the receiver. To account for intrinsic attenuation and the geometrical spreading of the energy, this probability is corrected by multiplication with a correction factor. The resulting probability is therefore the amount of energy at a receiver at the theoretically predicted arrival time of the particle. A benefit of this method is, that the energy density can be measured at point like receivers in media with weak symmetry. Every scattering event, if the scattering direction is towards the receiver, contributes to the local energy density at a receiver. A second method based on MC techniques was introduced by Gusev and Abubakirov (1987) and might be called a *particle counting* method. This method was for example used in algorithms by Margerin et al. (2000), Yoshimoto (2000), Przybilla and Korn (2008) or Sens-Schönfelder et al. (2009). In this method the central quantity of the RTEs, the specific intensity I, is modeled by the number density of particles N. To estimate the local particle density, the particles are counted in finite volumes around the receivers in consecutive time segments. Therefore snapshots of the energy density are stored in a 4D-array consisting of three spatial and one temporal dimension. In contrast to the method described by Hoshiba et al. (1991) this method has its advantages when the symmetry in the model setup is high, for example if the exploitation of a cylindrical or spherical symmetry is possible. This not only includes the symmetry of the medium but also includes the symmetry of the source radiation pattern. For sources with a realistic shear radiation pattern the symmetry is therefore weaker than for example for an isotropic source. In summary the algorithm used in this work is based on the *particle counting* method used by Gusev and Abubakirov (1987) and Yoshimoto (2000) and is briefly described in the following section 4.5.

4.5 Description of the simulation algorithm

Only a brief description of the simulation algorithm is given here, for more details the reader is referred to Sens-Schönfelder et al. (2009). To simulate the seismogram envelopes the MC method by Gusev and Abubakirov (1987) is followed. The counting of the particles is similar to the method described by Yoshimoto (2000). A description of the key features of the algorithm is given in the following lines:

Coordinate system

The propagation, as well as the recording of the particles takes place in a Cartesian co-ordinate system (figure 4.2). The z-axis denotes the depth of the model and increases in downwards direction. The x-axis describes the north-component, the y-axis represents the east-component. The position of the particle (x, y, z) and the particle velocity (v_x, v_y, v_z) are described within this coordinate system. The propagation direction, as well as the scattering process directions, are described by the polar and azimuthal angles θ and ϕ. The relation between the Cartesian and the spherical coordinate system is illustrated in figure 4.2.

Particle description

The particles in the simulation run are fully described by following parameters:

(1) Mode of the particle (P, S) .

(2) Coordinates in space and time (x, y, z, t).

(3) Velocity of the particle (v_x, v_y, v_z).

(4) Stokes vector **S** $([I^P, I^S_\theta, I^S_\phi, U, V])$ (equation 4.10).

(5) Polarization angle ψ (figure 4.2).

Additionally to these parameters, the direction of the particle velocity is stored in spherical coordinates (v_θ, v_ϕ). Auxiliary to the Stokes vector **S** the polarization angle ψ is kept stored throughout the simulation run. It describes the angle between the polarized axis of a linearly polarized S-particle and the vertical plane that includes the ray path. This redundantly stored information is used to speed up the simulations.

Particle emission and propagation

At the start of the simulation run the particles are emitted from a source following a defined radiation pattern. This for example includes an isotropic radiation pattern with no preferred direction of particle emission (figure 4.5) or an unidirectional source (figure 4.7). The ratio between emitted S-energy W_S and P-energy W_P is equal to the ratio of emitted S- and P-particles and is obtained from a model of a point-like shear dislocation. The ratio W_S/W_P for a shear dislocation according to Sato et al. (2012) is given as

$$\frac{W_S}{W_P} = \frac{3}{2}\gamma^5, \tag{4.22}$$
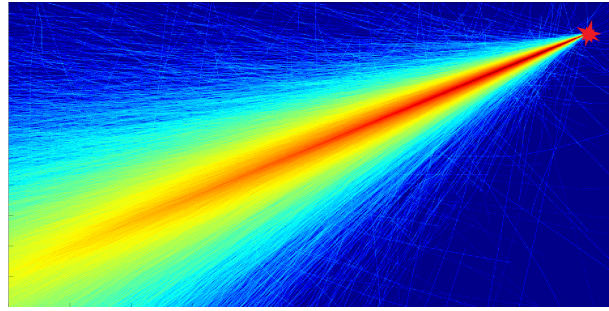
(a) scattering events
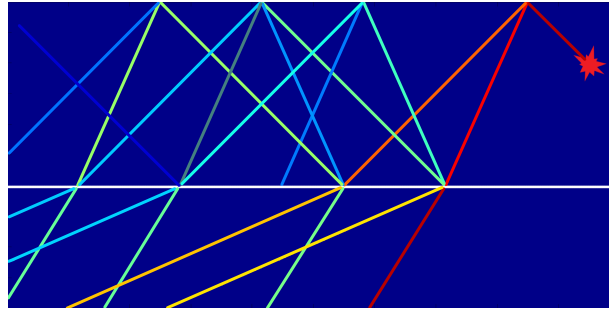
(b) ray theory
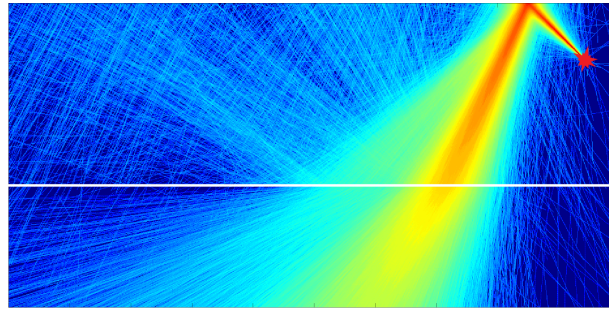
(c) ray theory + scattering

Figure 4.3: Energy propagation in different models. Source is represented by a red star, horizontal white line indicates an interface. Reddish colors represent regions with high seismic energy density, blueish colors represent areas with a low energy density. (a) Particles are emitted unidirectional in a heterogeneous full space model. The scattering of the particles is clearly visible. (b) Particles are emitted unidirectional towards the free surface in a homogeneous layer over half space model. Particles do not undergo any scattering and are propagating solely according to ray theory. (c) Same as (b) but in a heterogeneous layer over half space model.

with γ being the ratio of P- and S-wave velocity at the source. After the particles are emitted from the source, their propagation through the medium is determined by scattering events at medium heterogeneities and movement according to ray theory (figure 4.3b). These scattering events (figure 4.3a) at medium heterogeneities follow the Born approximation and include mode conversions and a possible change of prop-

agation direction. Particles are scattered into new modes and directions with a certain probability (Sens-Schönfelder et al., 2009), which is dependent on the total scattering coefficients (equations 4.18a to 4.18e). Propagation without scattering includes the interaction with interfaces (reflections, transmissions and mode conversions) or ray bending for propagation in regions with vertical velocity gradients. The propagation in a scattering medium with deterministic structures is shown in figure 4.3c.

Intrinsic attenuation

In the simulations two wave modes are present, P and S. Each of these modes has different attenuation parameters, therefore the loss of energy due to intrinsic attenuation has to be accounted for during the simulation runs. Particles continuously lose energy (I^P, I^S) over time as they propagate through the medium. The frequency dependent attenuation of P- and S-energy is proportional to the exponential decay rate of seismic wave ampliutde with distance r and is given as:

$$E_P(r, f) = e^{\frac{-2\pi r f}{v_p Q_P^i}}, \tag{4.23a}$$

$$E_S(r, f) = e^{\frac{-2\pi r f}{v_s Q_S^i}}. \tag{4.23b}$$

Here Q_P^i and Q_S^i denote the intrinsic quality factor for P- and S-waves, respectively. r represents the distance to the source.

Recording of energy

To estimate the local particle density, particles are counted in finite, 3D rectangular volumes around the receivers in consecutive time segments. This is achieved by adding the energy of the particle to the corresponding receiver volume for all directions. Therefore snapshots of the energy density are stored in a 4D-array consisting of three spatial and one temporal dimension.

Implementation and performance

The overall structure of the MC algorithm detailed above is implemented in the *C*-programming language. The particle propagation loop can easily be split up and can be parallelized on clusters of arbitrary size. The speed of the simulations strongly depends on the random medium structure, the number of particles, the number of available cores as well as on the simulation time length. Some of the processing steps after the simulation run are performed in the *Python*-programming language.

Test of the implementation

The algorithm has been tested to fulfill following criteria according to Sens-Schönfelder et al. (2009):

(1) Energy conservation by invariance of the number of particles in the simulation.

(2) Equipartition of P- and S-energy.

(3) Verification of the simulation method by comparison with 3D FD simulations (chapter 5).

4.6 Modeling of multi-component seismogram envelopes

The algorithm models the propagation of particles (wave packets). The particles, if averaged over a large number of them, represent the properties of the seismic wave field. It is straightforward to compute the seismogram envelopes of P- and S-energy in the RTT simulations. Only the mode, velocity and location of the particle, as well as the time step in the simulation are required for the synthesis of the envelopes of P- and S-energy. All these parameters are available for each particle at each time step during the simulations without any further calculations or transformations. The simulation of translational and rotational multi-component seismogram envelopes on the other hand, requires numerous transformations that depend on the particle propagation direction and on the particle polarization state. These transformations allow to simulate envelopes of translational motions in arbitrary directions as well as rotational motions around arbitrary axes. The first step is the rotation of the Stokes vector **S** (equation 4.10) from the system with variable polarization angle ψ (figure 4.2) into the standard system of SV and SH polarizations ($\mathbf{S} = (I_P, I_{SV}, I_{SH})$) using the following equation according to Ishimaru (1978) or Margerin et al. (2000):

$$\mathbf{S} = \begin{pmatrix} I_P \\ I_{SV} \\ I_{SH} \end{pmatrix} = \begin{pmatrix} 1 & 0 \\ 0 & \cos^2(\psi) \\ 0 & \sin^2(\psi) \end{pmatrix} \begin{pmatrix} I_P \\ I_S \end{pmatrix}. \tag{4.24}$$

The relations of intensity to the mean squared particle velocities $\langle |\dot{u}|^2 \rangle$, i.e. the mean squared envelopes, for the different polarizations are, according to Margerin et al. (2000), given as

$$\langle |\dot{u}_P|^2 \rangle = \frac{2Rs}{\rho} \frac{1}{v_P} I_P, \tag{4.25a}$$

$$\langle |\dot{u}_{SV}|^2 \rangle = \frac{2Rs}{\rho} \frac{1}{v_S} I_{SV}, \tag{4.25b}$$

$$\langle |\dot{u}_{SH}|^2 \rangle = \frac{2Rs}{\rho} \frac{1}{v_S} I_{SH}, \tag{4.25c}$$

with ρ being the density and v_P and v_S representing P- and S-wave group velocities, respectively. The term R describes a site effect, that accounts for local density perturbations and velocity variations, s represents the source strength. The term $2Rs/\rho$ will further be identified as C. Here $\dot{u}$ is assumed to be filtered in a narrow frequency band. Angle brackets indicate a time average over a few periods. The vectorial components of the velocities depend on the propagation direction of the wave packet. The propagation direction is given as $d(\theta, \phi)$, with θ being the particle direction measured from upwards to downwards and ϕ being the azimuth of the particle propagation measured from north to east, as illustrated in figure 4.2. From this propagation direction the

particle polarization directions $\mathbf{P}$ for P-, SV- and SH-waves are defined as:

$$\mathbf{P} = \begin{pmatrix} \mathbf{P_P} \\ \mathbf{P_{SV}} \\ \mathbf{P_{SH}} \end{pmatrix} = \begin{pmatrix} \sin(\theta)\cos(\phi) & \sin(\theta)\sin(\phi) & -\cos(\theta) \\ -\cos(\theta)\cos(\phi) & -\cos(\theta)\sin(\phi) & -\sin(\theta) \\ -\sin(\phi) & \cos(\phi) & 0 \end{pmatrix}. \tag{4.26}$$

The direction of the coordinate system in which the simulations are recorded, can be defined as a matrix $\mathbf{E}$ containing the unit vectors and is given by:

$$\mathbf{E} = \begin{pmatrix} E_{11} & E_{12} & E_{13} \\ E_{21} & E_{22} & E_{23} \\ E_{31} & E_{32} & E_{33} \end{pmatrix}. \tag{4.27}$$

This coordinate system can for example represent a standard XYZ-coordinate system, where $\mathbf{E}$ is the identity matrix (section 4.7.2) or a ray based LQT-coordinate system (section 4.7.1). The latter system depends on the source and receiver position and corresponds to the P-SV-SH axes of a direct wave illustrated in figure 4.2. The projections $\mathbf{\Pi}$ of the polarizations $\mathbf{P}$ onto the unit vector matrix $\mathbf{E}$ are therefore defined as:

$$\mathbf{\Pi} = \mathbf{EP} = \begin{pmatrix} \Pi_{11} & \Pi_{12} & \Pi_{13} \\ \Pi_{21} & \Pi_{22} & \Pi_{23} \\ \Pi_{31} & \Pi_{32} & \Pi_{33} \end{pmatrix}. \tag{4.28}$$

Applying equation 4.28 to the intensity vector S described in equation 4.24, the mean square velocity envelopes $\langle |\dot{u}_i|^2 \rangle$ (equations 4.25a to 4.25c) for the different directions $i = 1, 2, 3$ of the defined coordinate system is obtained. Thus the translational motion envelopes are given as:

$$\langle |\dot{u}_1|^2 \rangle = C(\frac{1}{v_P}\Pi_{11}^2 I_P + \frac{1}{v_S}\Pi_{12}^2 I_{SV} + \frac{1}{v_S}\Pi_{13}^2 I_{SH}), \tag{4.29a}$$

$$\langle |\dot{u}_2|^2 \rangle = C(\frac{1}{v_P}\Pi_{21}^2 I_P + \frac{1}{v_S}\Pi_{22}^2 I_{SV} + \frac{1}{v_S}\Pi_{23}^2 I_{SH}), \tag{4.29b}$$

$$\langle |\dot{u}_3|^2 \rangle = C(\frac{1}{v_P}\Pi_{31}^2 I_P + \frac{1}{v_S}\Pi_{32}^2 I_{SV} + \frac{1}{v_S}\Pi_{33}^2 I_{SH}). \tag{4.29c}$$

To derive envelopes of rotational motions around the coordinate system axis, the general relation between the particle velocity $\dot{u}$ and the rotation rate $\dot{\Omega}$, is considered, which is defined as:

$$\dot{\mathbf{\Omega}} = \begin{pmatrix} \dot{\Omega}_1 \\ \dot{\Omega}_2 \\ \dot{\Omega}_{3.} \end{pmatrix} = \frac{\mathbf{1}}{\mathbf{2}} \begin{pmatrix} \partial_2\dot{u}_3 - \partial_3\dot{u}_2 \\ \partial_3\dot{u}_1 - \partial_1\dot{u}_3 \\ \partial_1\dot{u}_2 - \partial_2\dot{u}_1 \end{pmatrix}. \tag{4.30}$$

For a locally plane wave with unit amplitude $|\bar{\dot{u}}_0| = 1$ the wave is defined as:

$$\bar{\dot{u}} = \bar{\dot{u}}_0 e^{i(\omega t - \bar{k}\bar{x})}. \tag{4.31}$$
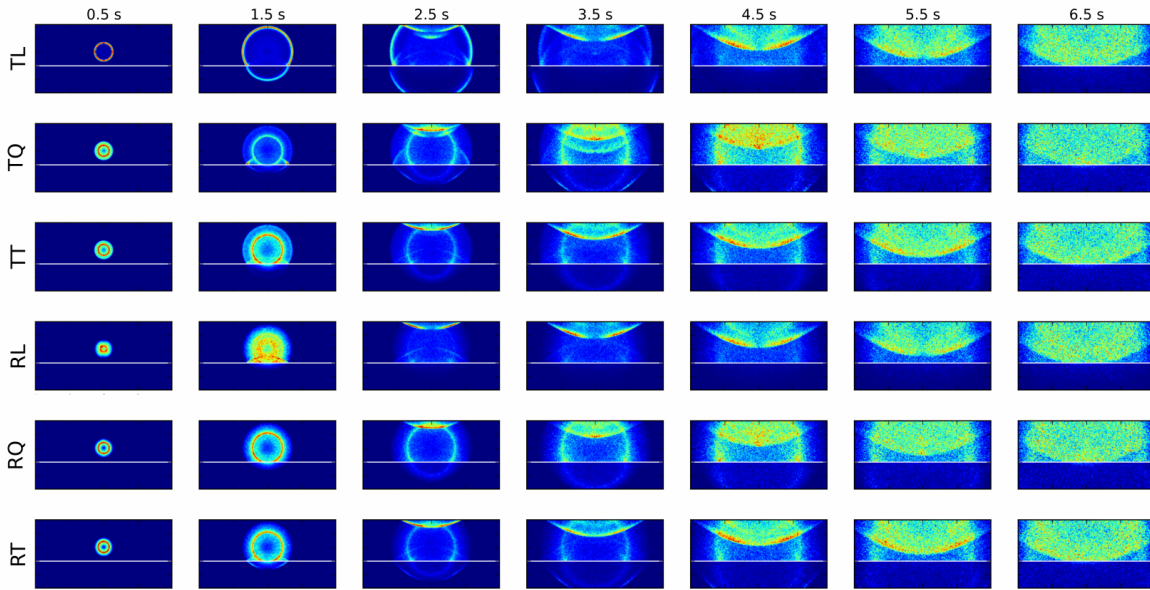
Figure 4.4: Multi-component RTT simulations. This figure illustrates the energy propagation for energy propagation for the three components of translational motion (TL, TQ, TT) and for the three components of rotational motion (RL, RQ, RT). Recording of the components takes place in a ray-based LQT system. The L-component represents the direct path from source to receiver, the Q-component represents the direction perpendicular to the radial component in the vertical plane and the T-component is defined as the direction perpendicular to the L and Q direction. A purely compressional source is placed in the upper part of the model, which represents the strongly heterogeneous crust. The mantle is represented by the bottom part of the model. Snapshots for different times are shown.

The partial derivatives ∂_l ($l = 1, 2, 3$) are given by

$$\partial_l \dot{u}_m = \dot{u}_{0m} e^{i(\omega t - \bar{k}\bar{x})}(-ik_l) = -ik_l \dot{u}_m, \tag{4.32}$$

where $m = 1, 2, 3$ and k_l is the l-th component of the wave vector, i.e. the projection of the propagation direction onto the l-th component of the recording coordinates, multiplied with ω/v_s. Here $\bar{k}$ is parallel to the P-polarization P_P. The mean square rotation rate $\langle|\dot{\Omega}|^2\rangle$ can now be obtained from the translational motion equations 4.29a to 4.29c using (4.30). As an example the equations for the mean squared rotation rates around the first axis of a general recording system from the intensities of P-, SV- and SH-waves are given as:

$$\langle|\dot{\Omega}_{1,P}|^2\rangle = C \left[\frac{1}{2}\frac{\omega}{v_p}(k_2 P_{P,3} - k_3 P_{P,2})\right]^2 \frac{1}{v_p} I_P, \tag{4.33a}$$

$$\langle|\dot{\Omega}_{1,SV}|^2\rangle = C\left[\frac{1}{2}\frac{\omega}{v_s}(k_2 P_{SV,3} - k_3 P_{SV,2})\right]^2 \frac{1}{v_s} I_{SV}, \tag{4.33b}$$

$$\langle|\dot{\Omega}_{1,SH}|^2\rangle = C\left[\frac{1}{2}\frac{\omega}{v_s}(k_2 P_{SH,3} - k_3 P_{SH,2})\right]^2 \frac{1}{v_s} I_{SH}. \tag{4.33c}$$

Note, that a P-wave does not excite rotations because of its longitudinal polarization ($k \parallel P_P$). Assuming a phase relation between the SV- and SH-polarizations, the total mean square rotation rate around the three axes ($i = 1, 2, 3$) can be derived from the summed contribution of the different polarizations. For XYZ-coordinates, where $\mathbf{E}$ is diagonal, the rotation rate around the vertical axis is therefore given as:

$$\langle\dot{\Omega}_z^2\rangle = \frac{1}{4}\frac{\omega^2}{v_s^3}C\left(\sin^2(\theta)I_{SH}\right). \tag{4.34}$$

Figure 4.4 shows example simulations for the three translational motions (equations 4.29a-4.29c) and for the three rotational motions in a ray based LQT coordiante system. A purely compressional, isotropic source is placed in the strongly scattering crustal part of the model. The bottom part of the model represents the weakly scattering mantle.

4.7 Simulation of local, regional and teleseismic events

In the following sections the modeling approaches are described to simulate the multi-component seismogram envelopes for shallow local and regional events (section 4.7.1) as well as for wave arrivals from deep teleseismic events (section 4.7.2).

4.7.1 Simulation of local and regional events

For the simulation of shallow local (chapter 6) and regional (chapter 7) events the translational and rotational seismogram envelopes are modeled in a ray based coordinate system (LQT-system). The choice of the LQT recording system is convenient as it can exploit the cylindrical symmetry of the problem. It allows to stack data from stations at different azimuth but similar distance, thus saving computational time in the MC-RTT simulations due to the computation of stacked envelopes. The recording system is dependent on the position of the source as well as on the location of the receiver element in the medium. The L-component therefore represents the direct path from source to receiver, the Q-component represents the direction perpendicular to the radial component in the vertical plane and the T-component is perpendicular to the L and Q directions. The unit vector matrix $\mathbf{E}_{LQT}$ for the LQT-coordinate system according to equation 4.27 is therefore identical to the matrix describing the P-, SV- and SH-polarizations (equation 4.26). In the simulation an isotropic point source with
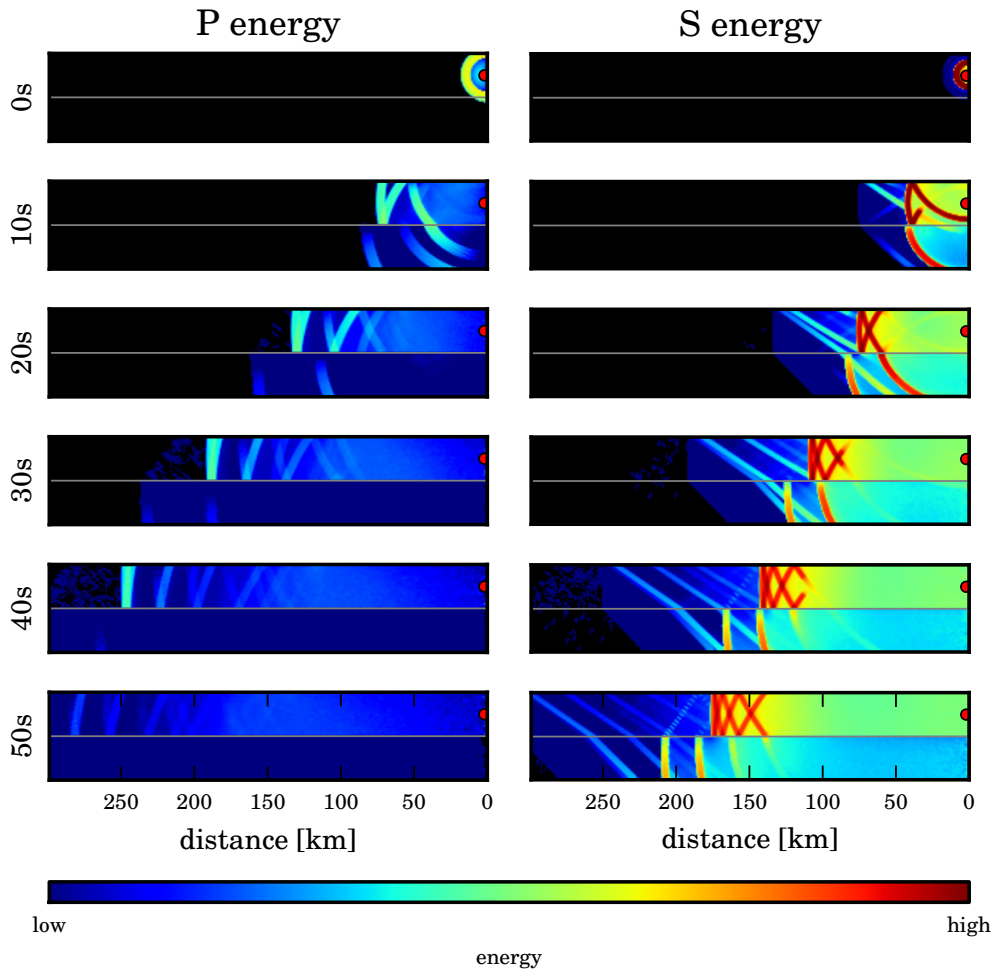
Figure 4.5: Energy propagation from a regional, shallow earthquake. An isotropic source (red circle) with a fixed P- to S- energy ratio is placed in the strongly scattering crust overlaying the transparent mantle (no scattering in the lithospheric mantle). Slices show snapshots of P-energy (left column) and S-energy (right column) for different times. Time is measured in seconds after the first arrival of energy at the surface. The development of guided S-energy (Lg-waves) is clearly visible. To increase the contrast for illustration purposes the ratio of emitted P- and S-energy at the source is set to 0.2.

a fixed P to S energy ratio (see for example Sato et al. (2012) or Shearer (1999)) of ~ 0.05 is modeled. To illustrate the energy propagation, cross-sections through the seismic wave field in the vertical plane for different depths are simulated. An example of the simulation output is shown in figure 4.5. The simulations of local and regional events with a hypocenter in the crust show strong reverberation of seismic energy in the crust. A striking feature is the formation of guided S-waves. It is clearly visible, that the seismic coda following the direct S-wave arrival is mainly composed of scattered S-energy, which is homogeneously distributed in space. Scattered P-energy only plays

a minor role in the generation of the seismic coda after the S-wave arrival.

4.7.2 Simulation of teleseismic events
Simulations using a directed source

To compute seismogram envelopes for teleseismic arrivals, not the full path from the distant source to the receiver is modeled, but rather the excitation by a plane, incoming wavefront is simulated. In the realistic setup this wavefront can be seen as a multitude of directed, parallel incoming particles and is illustrated for the vertical and tilted incidence in figures 4.6a and 4.6c. The green lines in figures 4.6a and 4.6c indicate
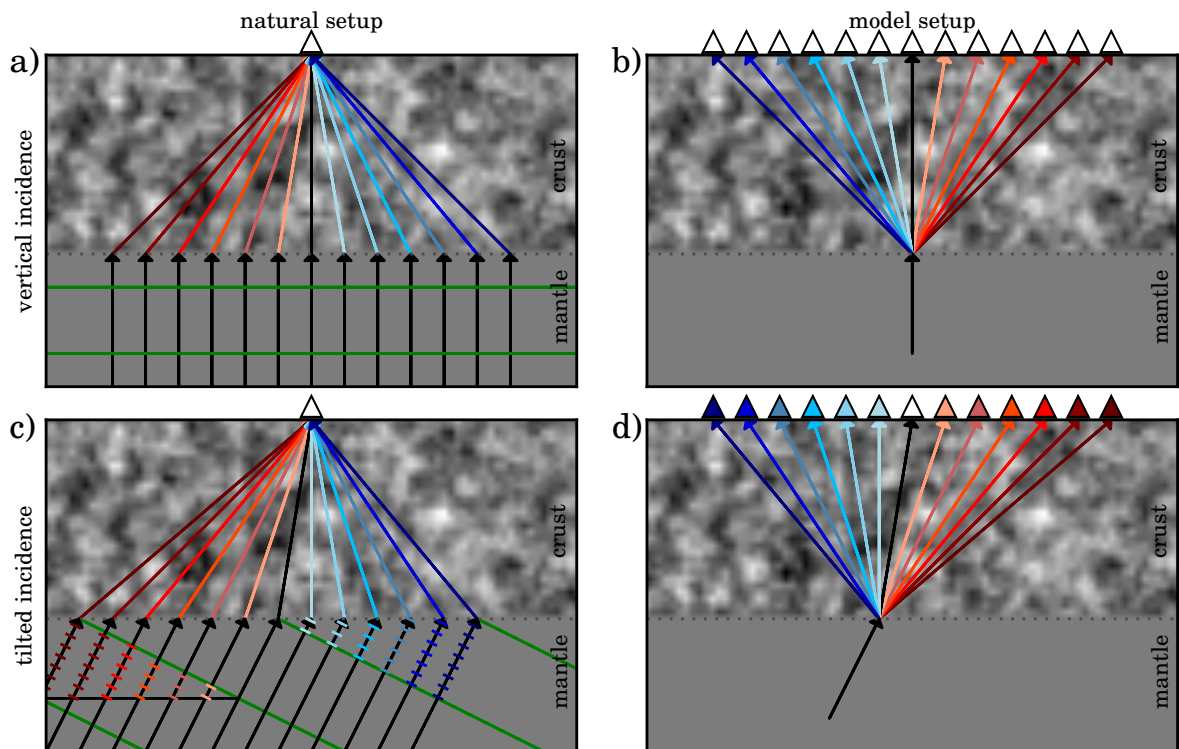
Figure 4.6: Modeling of a plane wavefront with a strongly scattering crust overlaying a transparent mantle. Left column illustrates a plane wavefront (green) in the realistic setup for vertical (a) and tilted incidence (c). The plane wave can be seen as a multitude of parallel incoming particles. In the model setup (b) and (d), the plane wave is modeled by one single incoming wave segment, its energy is recorded along the whole surface. Arrow colors in the left and right column indicate identical travel paths. For the tilted case of the model setup a time correction has to be applied for receivers apart from the central receiver. This time correction is indicated by colors inside the receivers in the tilted model setup. Blueish triangles indicate a positive time delay, reddish triangles indicate a negative delay.

the plane wavefronts. In the simulations such a wave can be excited by many different

unidirectional particle sources that fire with an offset dependent time delay if the incident angle is oblique. This time delay is indicated by the blueish ticks (positive
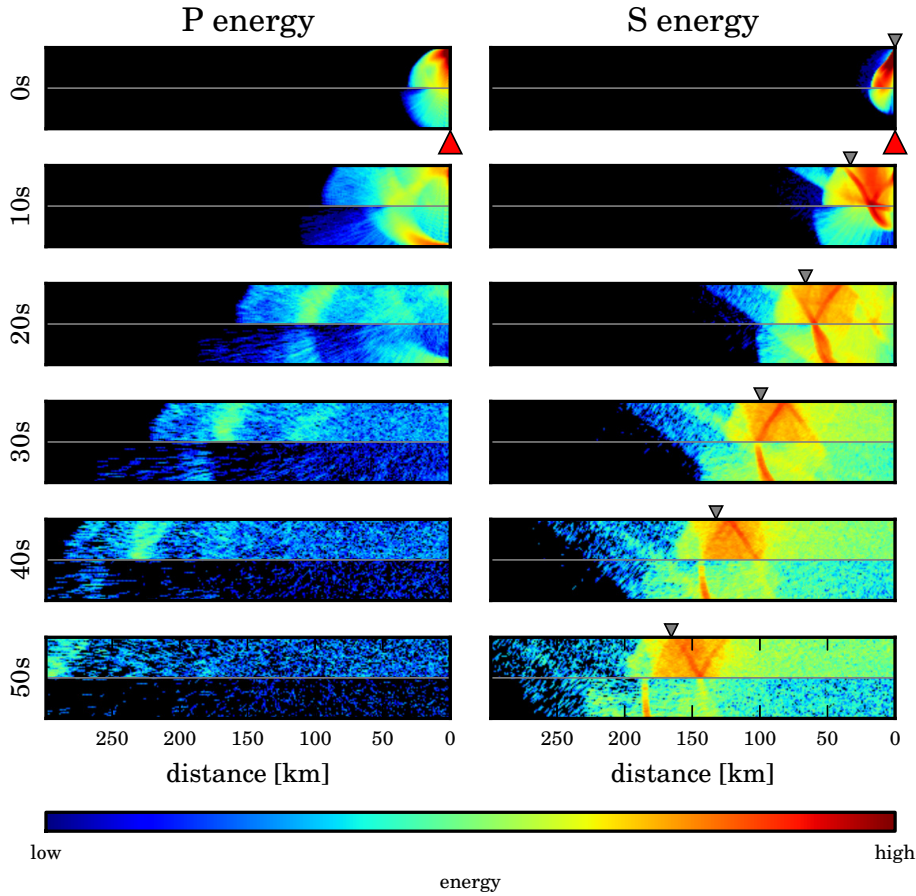
Figure 4.7: Energy propagation for a teleseismic event. A vertically directed purely compressional source (red arrow) is placed in the transparent mantle, underlying a strongly scattering crust. Slices show snapshots of P energy (left column) and S energy (right column) for different times. Time is measured in seconds after the first arrival of energy at the surface. Even though the energy is emitted only vertically from the source, the emergence of guided S-wave energy is clearly visible.

time delay) and the reddish ticks (negative time delay) along the rays in figure 4.6c. The resulting seismogram at one specific receiver in the realistic setup is the sum of the traces generated by all individual single directed sources measured at the receiver (figure 4.6c). In contrast to this natural setup with a plane wave generated by multiple sources, the model setup in the simulations makes use of the translational symmetry of the setup and only consists of one directional source. The seismogram for one receiver (central receiver in the model setup, figures 4.6b and 4.6d) is then given as the integral over all seismograms recorded at the surface receivers. Due to the translational invariance of the medium, the path from each unidirectional source to the receiver can also be found in the model setup. Identical travel paths are indicated by same colors.

44

The source delay for a tilted incidence translates into a delay of the records indicated by the color of the triangles in figure 4.6d. The simulations for teleseismic arrivals are carried out in a standard Cartesian XYZ-coordinate system. The unit vector matrix **E** in equation 4.27 is therefore defined as:

$$\mathbf{E}_{XYZ} = \begin{pmatrix} 1 & 0 & 0 \\ 0 & 1 & 0 \\ 0 & 0 & 1 \end{pmatrix}. \tag{4.35}$$

An example of the simulation for a vertically incident teleseismic P-wave is shown in figure 4.7. In this simulation a single vertically upward directed, purely compressional source in a homogeneous mantle is used. Even though initially the energy propagates only vertically, the development of horizontally propagating P- and S-energy wave trains is clearly visible after a short duration. This can be explained solely with scattering of seismic energy in the crustal part of the lithosphere. Similar to the excitation by a crustal source (figure 4.5) the seismic energy predominantly propagates as a guided S-wave even though the source is a pure P-source. To infer a seismogram envelope from figure 4.7 that shows the energy distribution in the model setup with a single source only, one needs to integrate over the surface of each time slice. This integration is required to transform from a model with one source and multiple receivers (figures 4.7b and 4.7d) to the natural setup with a plane wavefront represented by multiple sources and one single receiver (figures 4.6a and 4.6c). An example of the resulting seismogram envelopes is shown in figure 8.4.

Synthesis of the teleseismic seismogram envelopes

To synthesize the teleseismic seismogram envelopes a model is used consisting of a heterogeneous layer representing the crust over a half space representing the mantle. As scattering in the mantle is very weak in general (Sato et al., 2012), the mantle is chosen to be transparent, meaning no scattering of seismic energy occurs in the mantle. A purely compressional source is placed in the transparent mantle, excluding any source side scattering from the simulations. The energy is radiated in a single direction upwards with an angle θ_2, which results in the predicted angle at the surface θ_1. The incidence angle θ_1 is calculated from the IASPEI91 model (Kennett and Engdahl, 1991) from the depth of the event and the epicentral distance. An illustration of the relevant angles is presented in figure 4.8 From the angle θ_1 and the P-wave velocities in the crust and mantle, $v_{P,c}$ and $v_{P,m}$, the source radiation angle θ_2 in the mantle can be calculated according to Snell's law:

$$\theta_2 = \arcsin\left(\frac{v_{p,c}}{v_{p,m}} \sin \theta_1\right). \tag{4.36}$$

To obtain the final seismogram envelopes an integration over all receivers at the surface has to be applied. For a tilted incidence at the surface, a travel time correction is required for the seismogram envelopes recorded at the surface receivers. This correction is illustrated in figures 4.6c and d. A travel time shortening is required for rays that
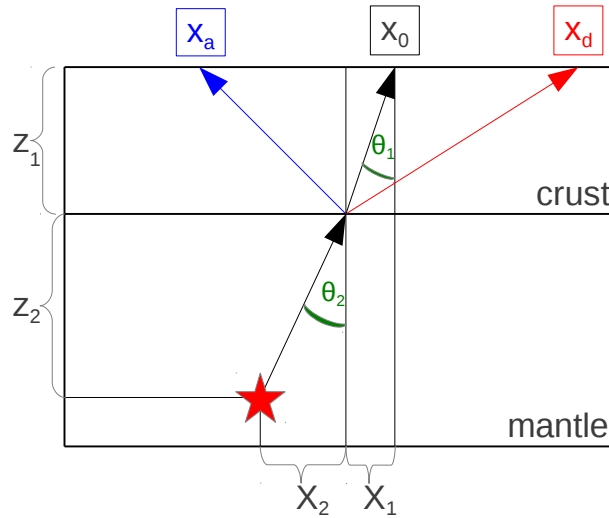
Figure 4.8: Teleseismic model. Illustration of relevant angles and the travel time correction. Red star represents the directed compressional source. x_a denotes a receiver with a travel time acceleration, x_d a receiver with a travel time delay. x_0 denotes the central receiver. Angles θ_1 and θ_2 represent the incidence angle and the source radiation angle, respectively.

travel a longer distance in the mantle (blue lines), on the other hand travel times have to be delayed for rays that have shorter travel times in the mantle (red lines). This time correction depends on the seismic P-wave speed in the mantle and on the incidence angle θ_2, when the ray hits the interface between mantle and crust. Only the travel time in the mantle has to be corrected. Travel paths in the crust have equal length and therefore do not require a travel time correction. In figure 4.8 the travel time correction is illustrated for one receiver which requires a negative travel time delay and for one receiver which requires a positive travel time correction. From the angle θ_1 and θ_2 the location of the central receiver x_0 can be calculated, this receiver does not require a travel time correction. The time correction for the remaining receivers (x_a and x_d) now depends on the receiver position at the surface with respect to the central receiver x_0. For all points at the surface the travel time correction is calculated according to following equation

$$t_c = (x - x_0)\frac{\sin(\theta_2)}{v_p}, \tag{4.37}$$

with t_c being the travel time correction for the envelopes, x_0 being the point at the surface for which the correction yields zero, x is the location of the receiver in x-direction and v_p is the P-wave speed in the mantle. The angle θ_2 indicates the source radiation angle. An example of the travel time correction is shown in figure 4.9. Top row shows the correction for the total translational motion energy (Z+N+E), middle row for the horizontal components (N+E) and bottom row for the vertical energy (Z). The uncorrected envelopes for the envelopes recorded at receivers at the surface are shown in the left column. x_0 is located at around 2500 km in x-direction. Applying the travel

time correction according to equation 4.37 for all receivers at the surface yields the corrected seismogram envelopes (figure 4.9, middle column). It can clearly be observed that envelopes with a travel time delay are shifted back in time (0–2500 km) and envelopes with a travel time acceleration are shifted to earlier times (2500-5000 km). The envelopes shown in the right column of figure 4.9 are the result of the integral of all envelopes over the entire surface and represent the teleseismic envelopes.
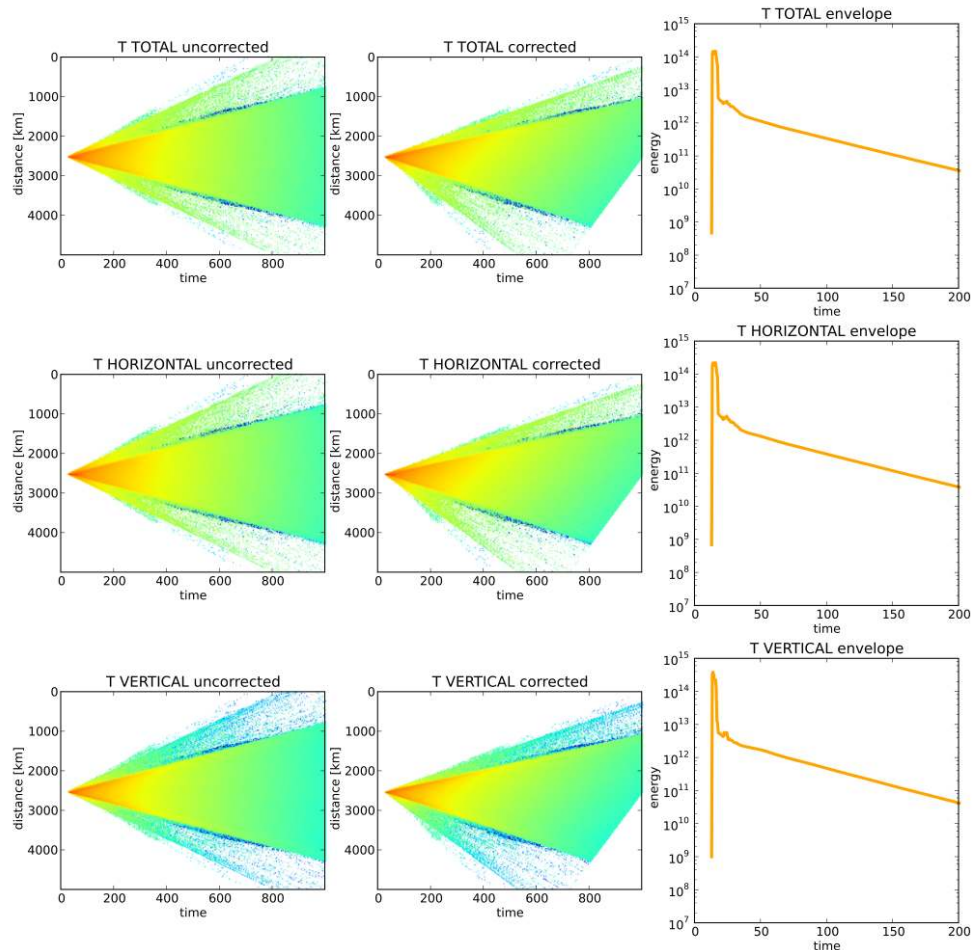
Figure 4.9: Travel time correction for the translational motions. Top row shows the total translational motion energy. Horizontal and vertical translational energy is shown in middle and bottom row, respectively. Left column shows the uncorrected envelopes recorded at the surface receivers, middle column shows the corrected envelopes. The right column shows the resulting envelope, when integrating over the entire surface. Greenish colors indicate low seismic energy, reddish colors indicate high seismic energy.

5 Validation of the simulation method

The simulation of the multi-component seismogram envelopes of translational and rotational ground motions using RTT is validated by comparisons with 3D FD-simulations. Section 5.1 describes the FD algorithm and the implementation of the rotational motions. The model setup for the comparison of FD and RTT simulations is described in section 5.2, the required data processing steps are given in section 5.3. Results of the comparison are presented, discussed and compared to results from another study in section 5.4.

5.1 Finite difference algorithm and implementation of the rotational motions

For many subsurface configurations, for example models including heterogeneity, interfaces or a free surface, it is not possible to find exact analytical solutions to the elastic wave equation to validate the results of the RTT simulations. Therefore the MC-RTT simulations are compared to an approach also based on numerical techniques. The theoretical waveforms of vector waves are computed using a FD technique implemented and described by Bohlen (2002). The software is named *FDMPI* (Finite Difference Message Passing Interface) and is based on an approach described by Virieux (1986) and Levander (1988). The utilized FD algorithm (Bohlen et al., 2010) is based on a staggered grid approach (figure 5.1) for particle velocities and stresses in space and time and employs higher order FD operators for the spatial and temporal dimensions. Seismic wave effects, such as dispersion or intrinsic attenuation, are considered by modeling an elastic, respectively viscoelastic, wave propagation through the medium. The software is implemented in the *C*-programming language and is based on a decomposition of the modeling domain. Therefore the software works only in MPI environments and consequently can be run on PC clusters or massive parallel supercomputers. The FD simulations for the comparison to the RTT simulations were executed on the supercomputer *JUROPA* (Jülich Research on Petaflop Architectures) located at the Jülich supercomputing center. The software *FDMPI* offers manifold opportunities to model
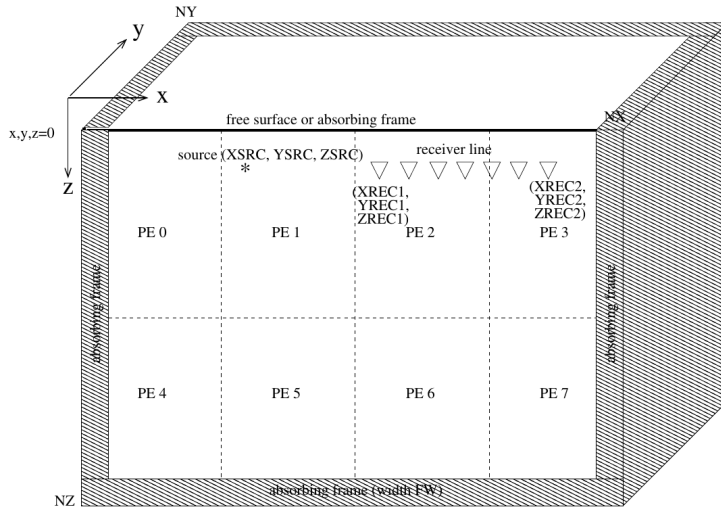
Figure 5.1: Geometry of the staggered FD grid. This grid uses 4 processors in x-direction and 2 in z-direction. The number of processors in y-direction in unspecified. At the surface either a free surface condition or an absorbing boundary condition can be applied. NX, NY and NZ indicate the number of gridpoints in the three directions. XSRC, YSRC and ZSRC specify the source location. XREC, YREC and ZREC indicate receiver positions. Figure redrawn from Bohlen et al. (2010).

the propagation of the seismic waves in various complex 3D Earth structures. Key features of the *FDMPI* program are:

- Various possible implementations of the seismic source, including different source wavelets (Ricker, Fuchs-Müller, sin^3, self-defined), different source types (P, S) and the option to define the source radiation direction.

- Output of the particle velocity in the X, Y and Z direction, total rotation, total divergence and of the pressure field.

- Incorporation of the free surface condition.

- Modeling of intrinsic absorption of seismic energy.

- Possibility to model different media (homogeneous, heterogeneous, layered, free surface)

- Different boundary conditions (absorbing boundaries, perfectly matched layer boundary condition, periodic boundary conditions)

To compare the multi-component seismogram envelopes from the MC-RTT simulations, the *FDMPI* software was extended not only to model the total rotational motions, but also to model the individual rotation rates around the different coordinate system axes. The rotational motions are incorporated into the code according to equation 4.30 and

considering the gradients of the particle velocities $(v_x,\ v_y,\ v_z)$ in the directions of the different coordinate system axes. This yields the three components of rotation rates $\dot{\omega}$ around the axes X, Y and Z:

$$\dot{\omega}_x = 0.5(\partial_y v_z - \partial_z v_y), \tag{5.1a}$$

$$\dot{\omega}_y = 0.5(\partial_z v_x - \partial_x v_z), \tag{5.1b}$$

$$\dot{\omega}_z = 0.5(\partial_x v_y - \partial_y v_x). \tag{5.1c}$$

The configuration was tested for different model setups (homogeneous full space, homogeneous half space with free surface) and different source types (isotropic and purely compressional source, pure shear source with different radiation patterns). Test simulations indicate, that rotation rate amplitudes are correctly modeled for the different components based on comparisons with analytical results. Furthermore the free surface condition is tested and can explain the rotational motions, generated through conversion processes at the surface, observable for a purely compressional source. Therefore the FD code can be used for the validation of the RTT simulations of translational and rotational motion seismogram envelopes.

5.2 Simulation setup

The comparison of the FD and MC-RTT simulations is similar to the comparisons described in a study by Przybilla and Korn (2008). For the FD simulations a model of size $76{\times}76{\times}76$ km is used with an absorbing boundary condition at the edges of the model to avoid reflections of seismic energy. The width of the absorbing frame at the borders of the modeling domain is 5 km. In each direction of the model 760 grid points are placed, the distance in between the grid points is 0.1 km. The total simulation length is 20 s, with time steps of 0.005 s. The choice of the temporal and spatial discretization ensures numerical stability of the simulations and minimizes simulation artifacts in the data. Average P- and S-wave velocity v_p and v_s of the medium are 6.0 km/s and 3.46 km/s, respectively. Random density and velocity fluctuations are added to the model in form of an exponential ACF (equation 2.5a), this ACF is described by a fluctuation strength ϵ of 10 % and a correlation length a of 1 km.

Density and velocity fluctuations are correlated, the correlation factor ν in equation 4.14 is chosen to be 0.8 (Sato et al., 2012). Intrinsic attenuation in the FD and MC-RTT simulations is not considered and set to zero. A source is placed in the center of the FD model domain. A purely compressional source is used with an isotropic radiation pattern. As source function in the FD simulations a Fuchs-Müller wavelet is used (Bohlen, 2002) with a dominant center frequency of 6 Hz. The seismic energy of the translational and rotational motions is recorded at receivers placed on spheres at distances of 10, 20 and 30 km from the source. In total approximately 2700 receivers are used, $\sim$ 200 on the 10 km sphere, $\sim$ 500 on the 20 km sphere and $\sim$ 2000 on the 30 km sphere.
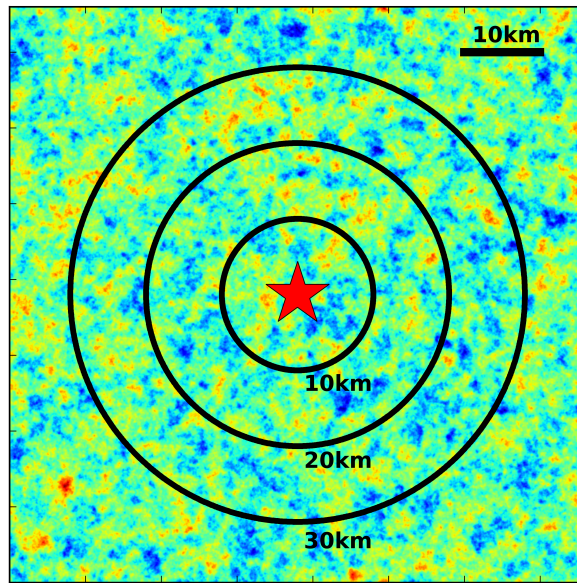
(a) cross section
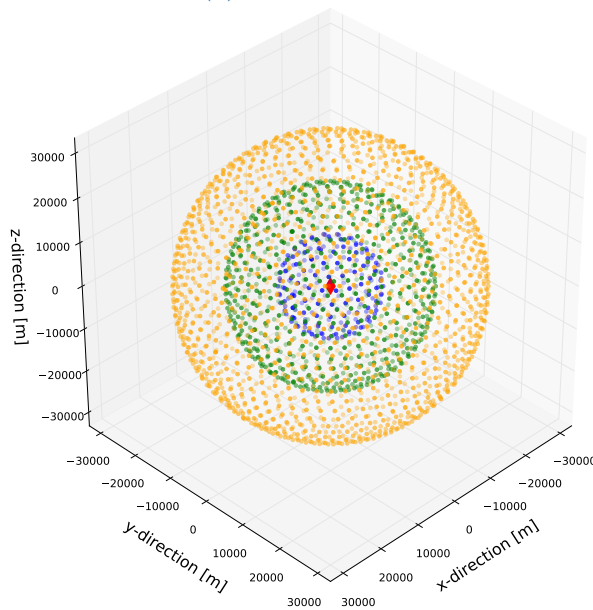
(b) 3D spheres

Figure 5.2: Receiver setup in the FD simulations. (a) 2D-representation of the expo-
nential random medium, which is described by density and velocity fluctu-
ations ϵ of 10 per cent and a correlation length a of 1 km. The receivers
are placed on spheres of radius 10, 20 and 30 km. (b) 3D-representation
of the receiver setup. Receivers are placed on spheres of radius 10, 20 and
30 km. The source is indicated in red color.

To account for different realizations of the medium, the simulations are computed for
ten different random media. This then yields a number of ~ 27000 receivers used in

the comparisons. A cross section through the medium with the receiver spheres is illustrated in figure 5.2a, a 3D-representation of the receiver setup is shown in figure 5.2b. Figures 5.3a and 5.3b show example translational and rotational motion traces from the FD simulations at 30 km distance. The traces are rotated from the XYZ recording system into the ray-based LQT system. In some cases energy is observable prior to theoretical arrival time of the direct P-wave (first orange line). This indicates energy traveling faster than the average background velocity. Rotational motions can already be observed in the coda of the direct P-wave, therefore indicating the scattering from P- to S-energy, as rotational motions are sensitive to shear energy only.

(a) translations (b) rotations
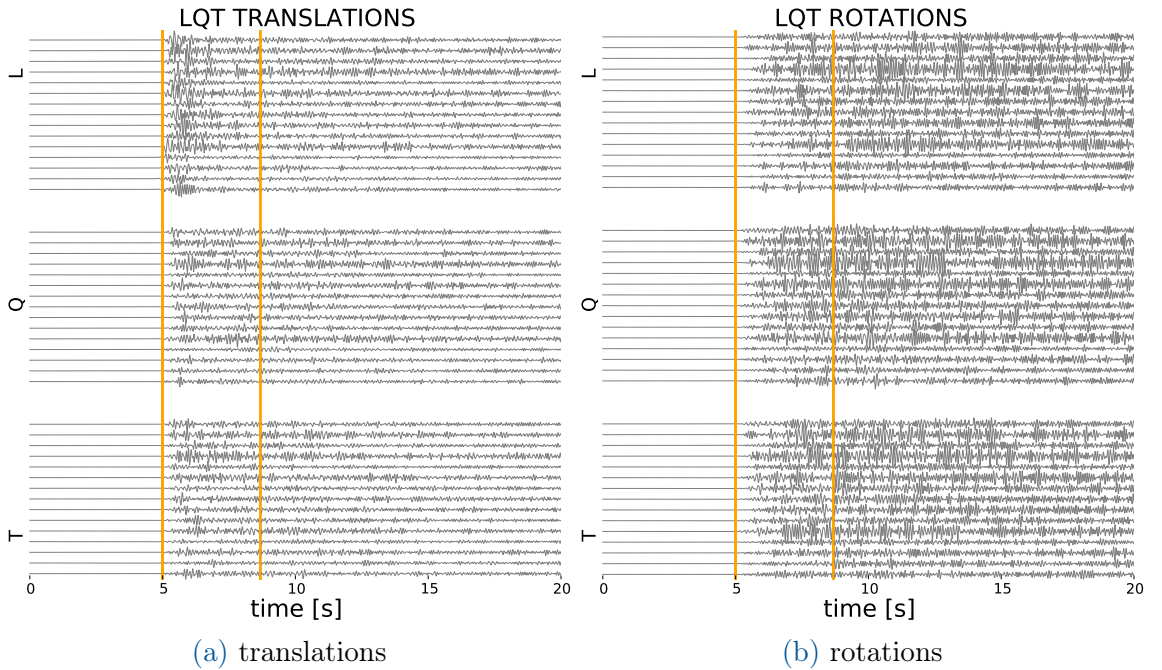
Figure 5.3: Example traces of translational and rotational motions in the FD simulations. (a) Translations in the LQT directions recorded at a distance of 30 km from the source. Due to the fact that a compressional source is used, most of the P-energy is observable in the radial (L) component. (b) Rotations around the LQT directions. Rotational motion energy can already be observed in the direct P-wave coda, indicating scattering processes from P- to S-energy. Orange lines indicate theoretical arrival time of the direct P- and S-wave traveling with v_p and v_s, respectively.

5.3 Data processing

To compare the FD simulations to the MC-RTT simulations, a number of processing steps are necessary, which are different for both methods. The processing steps are described as following:

FD simulations

First a bandpass filter around a center frequency f_c is applied. In this case a second order Butterworth bandpass filter around 6 Hz is applied to each individual trace of the translational and rotational motion components in the three distance ranges in the XYZ system. To be able to exploit the symmetry of the system for stacking of the traces, each trace is rotated from the original XYZ recording system into the ray-based LQT system. The L-component represents the radial direction, Q and T indicate the transverse directions. In a next step Hilbert envelopes are computed from each single rotated trace. In the final step, to obtain smooth envelopes, the Hilbert envelopes for each component (L, Q, T) and distance range (10, 20, 30 km) from the ten simulations are stacked and the mean envelopes are computed.

MC-RTT simulations

In the case of the MC-RTT simulations a rotation of the seismogram envelopes is not required, as the simulations are already recorded in the desired LQT system (compare section 4.7.1). Also the computation of the Hilbert envelopes is not necessary, as the MC-RTT simulations compute seismic energy, which is comparable to the envelopes of the squared velocities or rotation rates. Consequently the first step is to stack the envelopes for the individual receivers in the three distance ranges and compute mean envelopes for the six components and the three distances. The average envelopes are then convolved with the squared source time function wavelet from the FD simulations, to account for the finite length of the source-time function used in the FD simulations. Furthermore an effect, referred to as the wandering effect, is applied to the envelopes. This effect accounts for wave front distortions and travel time fluctuations due to the propagation of the seismic waves in a heterogeneous medium. The wandering effect yields a pulse broadening of the envelopes. This broadening is required, because in the MC-RTT simulations, unlike in the FD simulations, seismic energy in the form of particles propagates exactly with the average background velocities of the medium. The wandering effect is given as (Przybilla and Korn, 2008; Sato et al., 2012)

$$W(r,t) = \frac{v_0}{\sqrt{2\pi A r}} \exp\left(\left(-\frac{v_0 r^2}{2Ar}\right)\left(t - \frac{r}{v_0}\right)\right)^2 \tag{5.2}$$

and serves as a filter that is convolved with the MC-RTT envelopes. r indicates the propagation distance, v_0 the average background velocity and A represents the longitudinal integral of the ACF, in this case $2\epsilon^2 a$ for the exponential case.

The resulting final envelopes from the FD and MC-RTT simulations are presented in section 5.4.

5.4 Results of the method comparison

The comparisons of the FD and MC-RTT envelopes are similar to the ones published by Przybilla and Korn (2008). In figure 5.4, a comparison is shown from the latter study of translational motion envelopes calculated using FD and RTT simulations for a medium with moderate to strong forward scattering ($ak = 3.14$ and $ak = 9.42$). k denotes the wave number. Their simulations (figure 5.4) are carried out in a random medium with an exponential ACF. The central frequency of the simulations is 3 Hz, fluctuation strength ϵ is 10 % and the correlation length of the medium is 1 km and 3 km, respectively. The figure shows the RMS (root mean square) envelopes for the total (L+Q+T), radial (L) and one of the two transverse components (Q or T) for the 10, 20 and 30 km distance ranges. The authors find a reasonable agreement between the RTT and the FD simulations, especially in the amplitude and the shape of the direct P-wave arrival, as well as in the later seismic coda. For both cases of forward scattering ($ak = 3.14$ and $ak = 9.42$) they describe a slightly faster decay in the coda of the FD simulations, which is attributed to the loss of seismic energy at the edges of the model due to the absorbing boundary conditions. The most significant discrepancies are observed in the total and transverse component, where a clear second arrival of energy (direct S-wave) can be observed at $\sim$ 3, 6 and 9 s for the 10, 20 and 30 km distance ranges, respectively. This second peak is much smaller in amplitude in the RTT simulations and is attributed to a near-source effect. It is explained as an effect of medium heterogeneity, which produces an apparent S-wave radiation in all directions which is not explained in the RTT with Born scattering coefficients. In the transverse component for moderate forward scattering ($ak = 3.14$) the observed P-wave peak is much larger in amplitude in the RTT simulations in comparison to the FD simulations. This difference in amplitude diminishes with increasing distance and is explained by Przybilla and Korn (2008) with a deficiency in the Born scattering coefficients of the RTT.

The comparisons in this study are carried out in the forward scattering regime ($ak \sim 6.28$) in a random medium with an exponential ACF. Fluctuation strength ϵ is set to 10 %, the correlation length of the medium a is 1 km. Center source frequency is chosen to be 6 Hz. The energy envelopes are computed for the total (L+Q+T), radial (L) and transverse (Q or T) components for distances of 10, 20 and 30 km. In the comparisons not only the translational components are investigated, but in addition the rotational motions from the RTT and FD simulations are compared. The results of the comparisons are shown in figure 5.5. Looking at the translational motions (figure 5.5, left), and taking into account the convolution of the RTT simulations with the source time function and the wandering effect (equation 5.2), it can be observed that the amplitude and also the shape of the direct P-wave arrival in the RTT and FD simulations show very good agreement in the total, radial and transverse components. Also the decay of the seismic coda in the translations is simulated correctly. A slightly faster decay in the coda of the FD translations can be observed, as already described in Przybilla and Korn (2008). This effect is attributed to the choice of the absorbing

boundary conditions at the edges of the model domain. As seismic energy is absorbed at the model boundaries, it is not backscattered from scatterers outside the model domain and is therefore not modeled and included in the FD simulations. This effect does not occur in the MC-RTT simulations, as the propagation of seismic energy does not stop at the edges of the recording domain, backscattering is possible in the MC-RTT simulations. This explains the slightly higher coda level in the MC-RTT simulations. A second peak of energy in the translations can be observed especially in the transverse and total component at around 3, 6 and 9 s, corresponding to the distances of 10, 20 and 30 km. This peak is not as distinct in the radial components, due to the fact that mainly P-energy is observed in this component. The amplitude of this second peak of energy is slightly higher in the RTT simulations compared to the FD simulations, which is different from the observations made by Przybilla and Korn (2008). They explain the lack of energy in the RTT simulations with a near-source effect of the medium and the additional generation of shear energy at medium heterogeneity. This effect is avoided in this study by using multiple realizations of the medium to obtain the final envelopes. Therefore effects of the near-source heterogeneities are averaged out.

The most striking feature in the rotational motion envelopes (figure 5.5, right) is the absence of a sharp P-wave pulse in all components, which is easily explained by the fact, that rotational motions are sensitive to shear energy only. The overall shape of the seismogram envelopes until the onset of secondary energy peak (3, 6 and 9 s) agrees fairly well between both simulation methods with some amplitude differences observable. The amplitude differences are clearest in the radial component of the rotational motions and increase with increasing distance. Here it is noted, that logarithmic differences appear to increase for decreasing amplitudes, which might be linked to the limited precision of the FD simulations. The rotations are computed from the differences of neighboring points on the the staggered grid. For small amplitudes, as for the rotations around the radial direction, this might introduce a significant bias. In general the amplitudes in the MC-RTT simulations are higher than in the FD simulations. This is comparable to the results from the translational motions and can be explained with deficiencies in the simulation methods and in the Born scattering approximation. The coda decay agrees well, with the FD coda decaying faster, due to the aforementioned reasons.

In general it is concluded, that the rotational motions can be modeled with similar accuracy as the translational motions. The MC-RTT approach can therefore be used to model the multi-component seismogram envelopes of the high frequency seismic wave field.
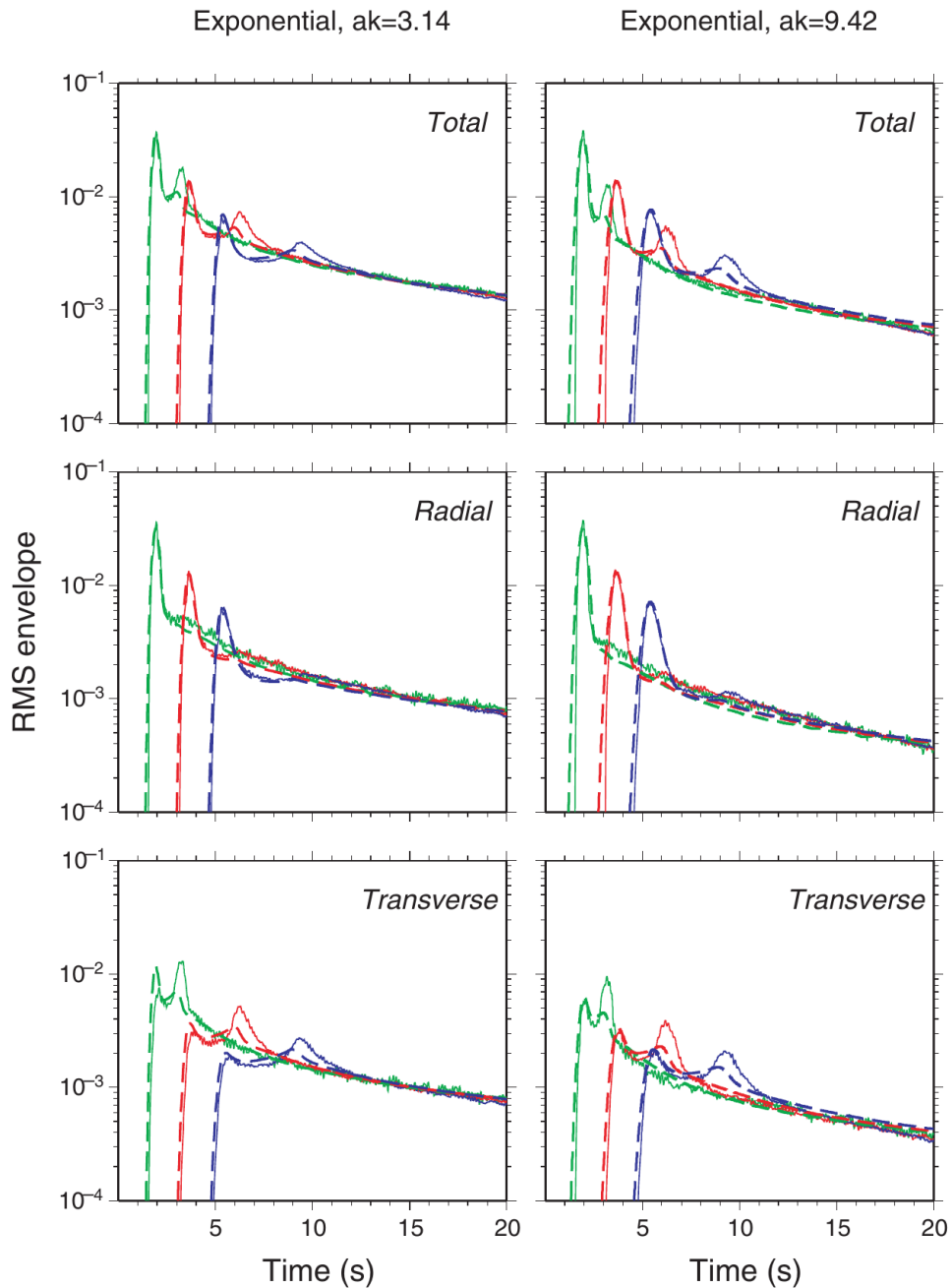
Figure 5.4: Comparison of translational motion envelopes from RTT and FD simulations. RTT and FD RMS envelopes in a random medium with exponential ACF, fluctuation strength ϵ is 10 per cent, correlation length a is 1 km (left column) and 3 km (right column). Center frequency in the simulations is 3 Hz. Top row shows total energy (L+Q+T), middle row shows radial energy (L) and bottom row shows transverse energy (Q). Dashed lines indicate RTT envelopes, solid lines indicate FD simulations. Green, red and blue color represent different distances (10, 20, 30 km). Figure redrawn from Przybilla and Korn (2008).
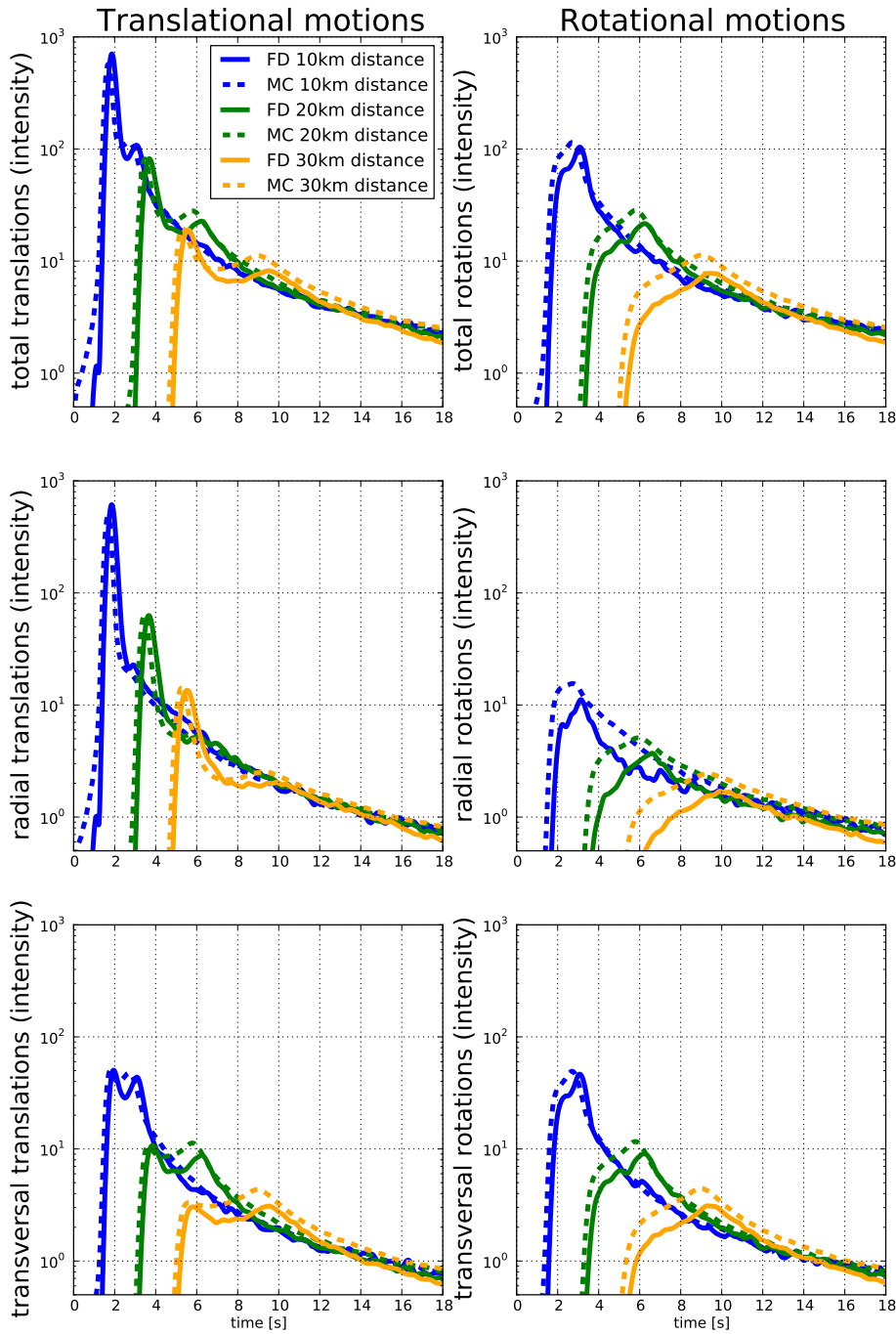
Figure 5.5: Comparision of translational and rotational motion envelopes from RTT and FD simulations. RTT and FD intensities in a random medium with exponential ACF, fluctuation strength ϵ is 10 %, correlation length a is 1 km. Center frequency in the simulations is 6 Hz ($ak \sim 6.28$). Left column shows the translational motions, right column gives the rotational motions. The top row shows the total energy (L+Q+T), middle row represents the radial component (L) and the bottom row shows the combined transverse components (Q+T). Dashed lines indicate RTT envelopes, solid lines indicate FD simulations. Blue, green and orange color represent the different distances of 10, 20 and 30 km.

6 Intrinsic and scattering attenuation on a local scale in the Vogtland

In the local data application the Vogtland region is investigated in terms of frequency dependent crustal scattering and intrinsic attenuation parameters. The parameters are estimated by comparing synthetic envelopes from acoustic and elastic RTT with seismic data from local swarm earthquakes. In the acoustic case a simple half space model with isotropic scattering is used, while in the elastic simulations a more complex setup with a layer over half space model under the assumption of multiple anisotropic scattering is used. The study area, the earthquake sources as well as the seismic receivers are introduced in section 6.1. The forward simulations, using the elastic and acoustic RTT method, and the processing of the data to generate the reference seismogram envelopes are described in section 6.2. The results of the comparison and additional outcomes are presented in section 6.3.

6.1 Study area and data

In the local data set investigations the focus lies on the crustal structure beneath the Vogtland region, situated at the border of the Czech Republic and Germany. The study area is illustrated in figure 6.1. The Vogtland region is attributed to the western part of the Bohemian Massif, one of the largest areas of exposed basement rocks in central Europe. The main tectonic structures in this area are the Eger-Rift-system (Prodehl et al., 2006) and the Regensburg-Leipzig-Rostock-Zone with the Cheb basin in the center. Numerous faults of various striking directions can be found in the area, with the most prominent being the Márianské Lázně fault (Fischer et al., 2013). The study area is of high interest as it is one of the few intra-continental regions in Europe, that exhibits present activity of geodynamical processes. Hints for these processes include the natural degassing of CO_2 from great depths, that is visible in the form of CO_2 rich mineral waters, or in the existence of wet and dry mofettes in the Vogtland region (Weinlich et al., 2003; Geissler et al., 2005). Another hint to the geodynamic processes is the present seismic activity in the Vogtland region. This activity mainly occurs in the

form of earthquake swarms with magnitudes no greater than 5 (M_L). The most recent swarms occurred in January 1997, August to December 2000, October to November 2008, October 2010, August to September 2011 and in August 2014. The earthquake-swarms have been subject to numerous studies (Heinicke et al., 2009; Vavryčuk, 2011). However, the underlying triggering mechanism of the earthquakes is still under debate. For more information about the study area, the swarm-earthquakes and the possible triggering mechanisms, the reader is referred to the excellent review paper by Fischer et al. (2013).
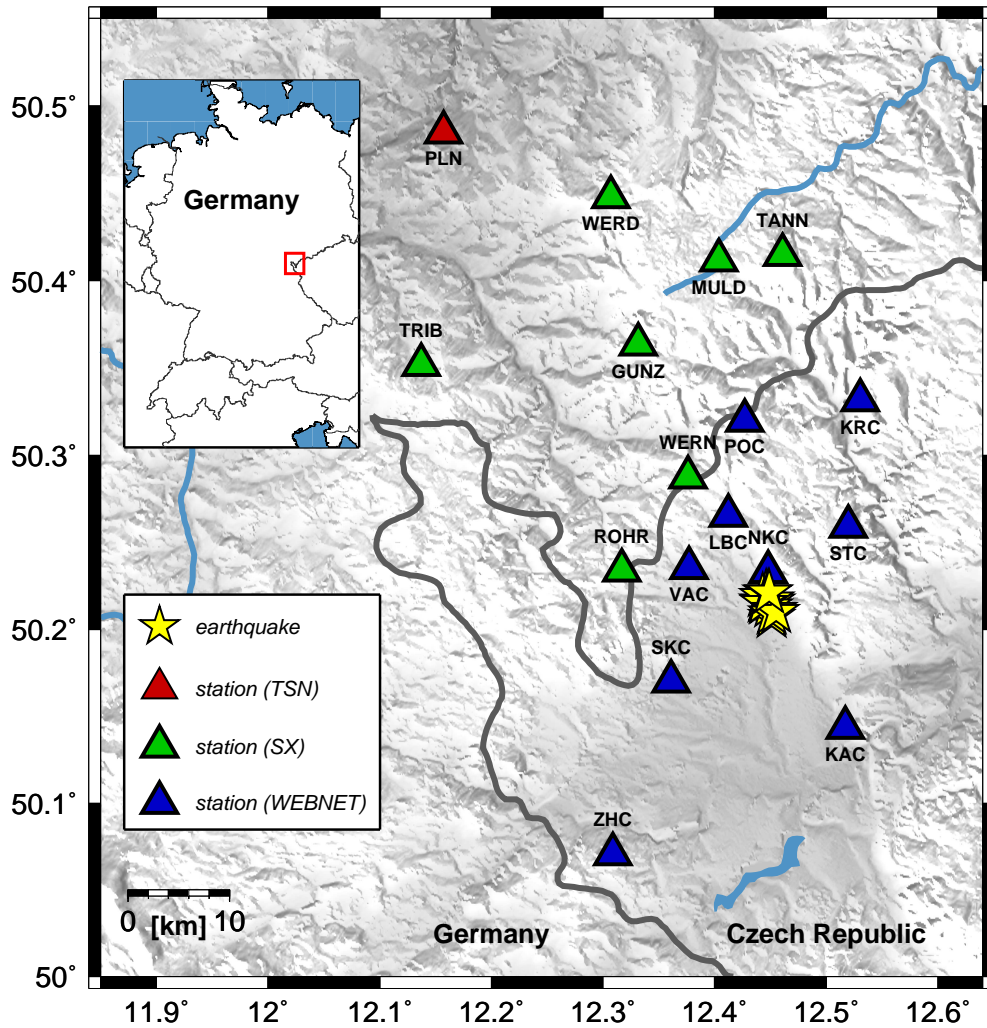
Figure 6.1: Study area in the local data application. The map shows the Vogtland region at the border of the Czech Republic and Germany in Europe. Colored triangles indicate the used seismic stations of the Thuringian seismic network (TSN, red), the Saxonian seismic network (SX, green) and from the Czech WEBNET network (WEBNET, blue). The investigated local earthquakes are indicated by yellow stars. Grey background shading represents topography. For additional details on earthquakes and stations see also tables 6.1 and 6.2.

As reference data for the inversion process for crustal scattering and attenuation parameters 14 earthquakes of the October 2010 swarm are used. Magnitudes (M_L) of the earthquakes are in the range from 3.1 to 4.2, event depths vary between 10 and 12 km. Earthquake locations, event depths, magnitudes and source times were estimated by the German Seismological Central Observatory (SZO). For an illustration of the epicenter locations see figure 6.1, event details are given in table 6.1. The events are recorded at 17 three-component seismic broadband stations, seven operated by the the Saxonian seismic network (SX), nine by the Czech WEBNET network (WEBNET) (Horálek et al., 2000) and one operated by the Thuringian seismic network (TSN). A list of stations is given in table 6.2, station locations for the different networks are illustrated in figure 6.1.

number	date	time	coordinates	depth	magnitude	region
01	2008-10-10	00:39:44	50.215°N 12.445°E	11 km	3.6 (ML)	Vogtland
02	2008-10-10	03:22:04	50.216°N 12.443°E	12 km	3.9 (ML)	Vogtland
03	2008-10-10	04:22:16	50.221°N 12.446°E	12 km	3.1 (ML)	VogtlanD
04	2008-10-10	07:32:01	50.216°N 12.451°E	11 km	3.3 (ML)	Vogtland
05	2008-10-10	08:08:45	50.213°N 12.449°E	11 km	4.2 (ML)	Vogtland
06	2008-10-10	11:18:41	50.217°N 12.450°E	11 km	3.5 (ML)	Vogtland
07	2008-10-10	19:08:31	50.219°N 12.443°E	11 km	3.3 (ML)	Vogtland
08	2008-10-12	07:44:15	50.207°N 12.451°E	11 km	3.9 (ML)	Vogtland
09	2008-10-14	04:01:35	50.215°N 12.444°E	12 km	3.2 (ML)	Vogtland
10	2008-10-14	19:00:32	50.211°N 12.453°E	12 km	4.0 (ML)	Vogtland
11	2008-10-21	02:14:01	50.221°N 12.448°E	11 km	3.4 (ML)	Vogtland
12	2008-10-28	08:30:10	50.209°N 12.451°E	11 km	4.1 (ML)	Vogtland
13	2008-10-28	10:07:00	50.210°N 12.444°E	10 km	3.1 (ML)	Vogtland
14	2008-10-28	14:51:52	50.221°N 12.449°E	11 km	3.1 (ML)	Vogtland

Table 6.1: List of earthquakes used in the local data application.

This choice of stations and earthquakes results in epicentral distances from 10 km up to around 40 km. Accordingly travel times range from 2 s for P-waves to 14 s for S-waves. P- and S-wave arrivals were manually picked. From these travel times a very local average velocity model for this region was calculated with $v_P = 5.12\ km/s$ and $v_s = 3.12\ km/s$. The estimated seismic velocities are used in the computation of the synthetic seismogram envelopes.

6.2 Methods, data processing and misfit calculation

The crustal scattering and attenuation parameters in the Vogtland region are estimated using two different approaches, each based on the theory of radiative transfer of seismic energy. The first approach is based on the assumption of multiple anisotropic scattering

network	station	coordinantes	elevation	location
SX	ROHR	50.234°N 12.317°E	629m	Rohrbach, Germany
SX	WERN	50.287°N 12.376°E	672m	Wernitzgrün, Germany
SX	GUNZ	50.364°N 12.332°E	669m	Gunzen, Germany
SX	MULD	50.412°N 12.404°E	678m	Muldenberg, Germany
SX	TANN	50.415°N 12.461°E	836m	Tannbergsthal, Germany
SX	TRIB	50.352°N 12.137°E	510m	Obertriebel, Germany
SX	WERD	50.448°N 12.307°E	589m	Werda, Germany
CZ	NKC	50.233°N 12.448°E	564m	Nový Kostel, Czech Republic
CZ	VAC	50.235°N 12.377°E	530m	Vackov, Czech Republic
CZ	LBC	50.266°N 12.412°E	638m	Luby, Czech Republic
CZ	STC	50.259°N 12.520°E	666m	Studenec, Czech Republic
CZ	SKC	50.170°N 12.361°E	455m	Skalná, Czech Republic
CZ	KAC	50.144°N 12.517°E	524m	Kaceřov, Czech Republic
CZ	POC	50.320°N 12.427°E	790m	Počátky, Czech Republic
CZ	KRC	50.332°N 12.530°E	760m	Kraslice, Czech Republic
CZ	ZHC	50.071°N 12.309°E	631m	Zelená Hora, Czech Republic
TSN	PLN	50.485°N 12.157°E	432m	Plauen, Germany

Table 6.2: List of stations used in the local data application.

of elastic energy at randomly distributed small scale heterogeneities and is described in section 4.7.1. This approach will also be used in chapter 7 in the inversion of the regional swarm earthquakes. The second approach assumes multiple isotropic scattering of acoustic seismic energy and is detailed in section 4.2. In both methods synthetic envelopes are compared to reference seismogram envelopes created from the individual local swarm earthquakes recorded at different stations in different frequency bands.

In the first approach of elastic radiative transfer the forward simulations are calculated using the simulation approach for local and regional earthquakes described in section 4.7.1. Multi-component translational motion seismogram envelopes are calculated in the LQT coordinate system and compared to the reference envelopes. For the modeling a domain with lateral dimensions of 100×100 km is used with a source placed in the center of the model in depth of around 11 km, which is the average depth of the used swarm-earthquakes (table 6.1). The source has an isotropic radiation pattern with a fixed ratio of P- to S-energy of ~ 0.05 (Shearer and Earle, 2008). The dimensions of the recording domain and the placement of the source allow the simulation of envelopes in epicentral distances up to 50 km. In the simulations a layer over half space model is assumed, with the layer representing the crust with a thickness of 30 km (Zeis et al., 1990). The mantle is represented by the half space. This setup is similar to the regional investigations described in chapter 7. The crustal scattering and attenuation parameters are estimated in different frequency bands and for each individual earthquake. A grid search method is used to find the best fitting parameters in each frequency band. For predefined sets of crustal parameters of intrinsic attenuation Q_S^i (Q_P^i), fluctuation

strength ϵ and correlation length a the forward simulations are calculated. The parameters are chosen to uniformly sample a parameter space of realistic crustal scattering and attenuation values. Crustal density and velocity fluctuations ϵ vary in the range from 0.1 to 10 per cent, the correlation length a is chosen to be equally sampled between 0.1 to 10 km. The random medium is described by an exponential ACF. The intrinsic attenuation for S-waves Q_S^i varies between 100 and 1500. Assuming a fixed Q_P^i/Q_S^i ratio of 2.25 (Shearer, 1999), this then corresponds to P-wave quality factors Q_P^i in the range from 225 to 3375. The scattering and attenuation parameters in the mantle are set to be equal to the crustal values in the predefined parameter sets. To ensure reflections at the interface between crust and mantle, wave speeds in the mantle are set to be higher than in the crust. The influence of scattering and attenuation in the mantle on the propagation of seismic waves in a local frame is very weak and therefore justifies the used mantle parameters. For each of the individual earthquakes in the different frequency bands, the precomputed forward simulations can now be used to find the best fitting set of crustal parameters to describe the reference data.

The second method used is also based on the theory of radiative transfer, but only models the transfer of acoustic energy under the assumption of multiple isotropic scattering. The approach to model the energy density is presented in section 4.2 and is similar to the one described by Sens-Schönfelder and Wegler (2006). Acoustic indicates in this case, that only the propagation of seismic shear energy is considered in our model, the radiative transfer of P-energy and consequently conversions from P- to S-energy and vice versa are not included in this approach. The possibility of multiple scattering is considered, that means seismic energy can be scattered more than once from the source to the receiver. Furthermore those scattering events are isotropic, meaning that there is no preferred direction of scattering at the medium heterogeneities. In the simulations energy propagation is modeled in a half space medium with an isotropic shear wave source placed in a depth of ~ 11 km, the average depth of the swarm earthquakes. An inversion process is used to estimate the crustal scattering and attenuation parameters in terms of the transport mean free path length l^* and the mean free absorption path l_i. In the case of acoustic radiative transfer l^* is given as

$$l^* = \frac{1}{g_0} \tag{6.1}$$

and l_i is defined as

$$l^i = \frac{v_s}{b}, \tag{6.2}$$

here v_s denotes the S-wave velocity and g_0 the total scattering coefficient. In contrast to the computationally very expensive elastic simulations, an individual inversion for the crustal parameters for each individual earthquake in different frequency bands is feasible. The main drawback of the acoustic simulations is, that it is only possible to model the propagation of S-wave energy, therefore not considering P-energy transport. Furthermore, due to the assumption of isotropic scattering, forward scattering cannot be included and modeled in the simulations.

The elastic and acoustic RTT simulations are compared to reference envelopes R. These are generated by processing three-component seismic data from the stations listed in table 6.2. In a first step data is corrected for the instrument sensitivity to obtain absolute velocity seismograms in m/s. Furthermore data was demeaned and detrended prior to filtering. For comparison with the synthetic data the seismograms are filtered using a 2-corner Butterworth filter with zero shift in four frequency bands: 2–4, 4–8, 8–16 and 16–32 Hz. This results in center frequencies of 3, 6, 12 and 24 Hz. After filtering, seismogram envelopes are computed using the Hilbert transformation. Noise is removed from the traces by subtracting the average level of noise in a 2 s time window prior to the arrival of the first direct wave. In the acoustic case the three component envelopes are stacked to obtain total energy envelopes. For comparisons with the elastic simulations the traces are rotated from the classical ZNE-system into the ray-based LQT-coordinate system prior to the computation of the Hilbert envelopes. After stacking, respectively rotation, the envelopes are smoothed with a 0.5 s window to mimic an ensemble average for different realizations of the medium. The final step of the processing includes a correction for site effects at the stations (site amplification factor correction) using the coda normalization method after Aki (1980).

The fit of the simulations is evaluated in terms of its misfit to the reference envelopes. Misfits between the RTT forward simulations denoted with S and the reference envelopes R obtained from the swarm earthquakes are calculated as the sample-wise logarithmic L1-norm given by

$$M = \sum_{i=0}^{n} \sum_{j=0}^{m} |log(R[i,j]) - log(S[i,j])|\,, \qquad (6.3)$$

with n being the number of reference traces depending on the number of stations and on the number of recorded components. m is the number of samples in each trace. Using logarithmic differences ensures that high-amplitude direct waves and lower-amplitude coda values, have a similar weight in the misfit calculation. Furthermore the misfit calculation using the L1-norm is less sensitive to fluctuations in the forward simulations or the reference traces.

Comparisons of elastic and acoustic synthetic envelopes and the estimated parameters in the different frequency bands are presented in the following section.

6.3 Results of the comparison

In section 6.3.1 the results of the estimation of crustal scattering and attenuation parameters are presented. Investigations of parameter trade offs and limits in the resolution possibilities of the parameters are discussed in section 6.3.2.

6.3.1 Seperation of intrinsic and scattering attenuation

In the elastic approach intrinsic attenuation is estimated in terms of the quality factor for S-waves Q_S^i, while in the acoustic approach the intrinsic attenuation is expressed through the absorption coefficient b (equation 4.6). To compare the results of both methods intrinsic attenuation will further be presented as the absorption path length for S-waves l_S^i defined as:

$$l_S^i = \frac{v_s}{b} = \frac{v_s Q_S^i}{2\pi f}.$$

(6.4)

The scattering strength will further be expressed through the transport mean free path for S-waves l_S^*, which can be regarded as the propagation distance required for a wave to lose memory of its initial direction. In the elastic case the scattering properties are represented by the density and velocity fluctuations ϵ and the correlation length a. The parameters ϵ and a are linked to the transport mean free path l_S^* via the total scattering coefficients g_{ij} and the Fourier spectra P of the ACF R of the medium (Sato et al., 2012). The elastic transport mean free path for S-waves l_S^* is given as (Przybilla et al., 2009):

$$l_S^* = \frac{g_{PS}^0 + g_{PP}^0 - g_{PP}^D + g_{SP}^D}{(g_{PS}^0 + g_{PP}^0 - g_{PP}^D)(g_{SP}^0 + g_{SS}^0 - g_{SS}^D) - g_{PS}^D g_{SP}^D}.$$

(6.5)

The terms g_{ij}^D are defined as:

$$g_{ij}^D = \frac{1}{4\pi} \oint g_{ij}(\theta, \phi) \cos\theta d\Omega.$$

(6.6)

In the acoustic simulations the total scattering g_0 is estimated, which is related to the transport mean free path through equation 6.1.

The crustal scattering and attenuation parameters are estimated by comparisons of elastic and acoustic synthetic RTT envelopes to reference data envelopes as described in section 6.2. An example of the envelopes for one individual earthquake from the elastic and acoustic approach, that best describe the reference envelopes is shown in figure 6.2. The reference envelopes in figure 6.2 are created from earthquake 10 (table 6.1) in the frequency band from 4–8 Hz ($f_c = 6$ Hz). Recordings from five exemplary stations (LBC, ROHR, KRC, TANN and PLN) and the simulations for the corresponding distance ranges are shown. For both the elastic and the acoustic approach, the decay of the seismic coda following the S-wave arrival can be modeled with a high precision for lapse times up to 50 s. The onset of the direct guided S-wave in the crust can be modeled with good agreement in terms of amplitude of the envelope as well as in terms of the shape of the pulse using the elastic RTT approach. On the other hand the direct P-wave onset in the elastic simulations is more difficult to model. These discrepancies can to a large extent be explained by the isotropic source radiation pattern used in the simulations, which does not represent the true source radiation. Due to the use of individual earthquakes instead of stacked earthquakes (chapter 7),

the influence of the source radiation pattern is even stronger. Another reason for the rather poor simulation of the P-wave onset might be a deviation of the true unknown Q_P^i/Q_S^i ratio to the theoretical value of 2.25, which is assumed in the simulations. In the acoustic simulations the pulse broadening of the S-wave onset due to reverberations in the crustal layer and velocity fluctuations is not included in the modeling. The ballistic S-waves are only represented by a delta peak in the simulations. To account for these systematic differences in the shape of the direct S-envelope an average value around this peak is calculated to describe the total energy content of the S-wave onset. Comparisons of the average S-peak energies from data and acoustic simulations in general show a good agreement (figure 6.2).
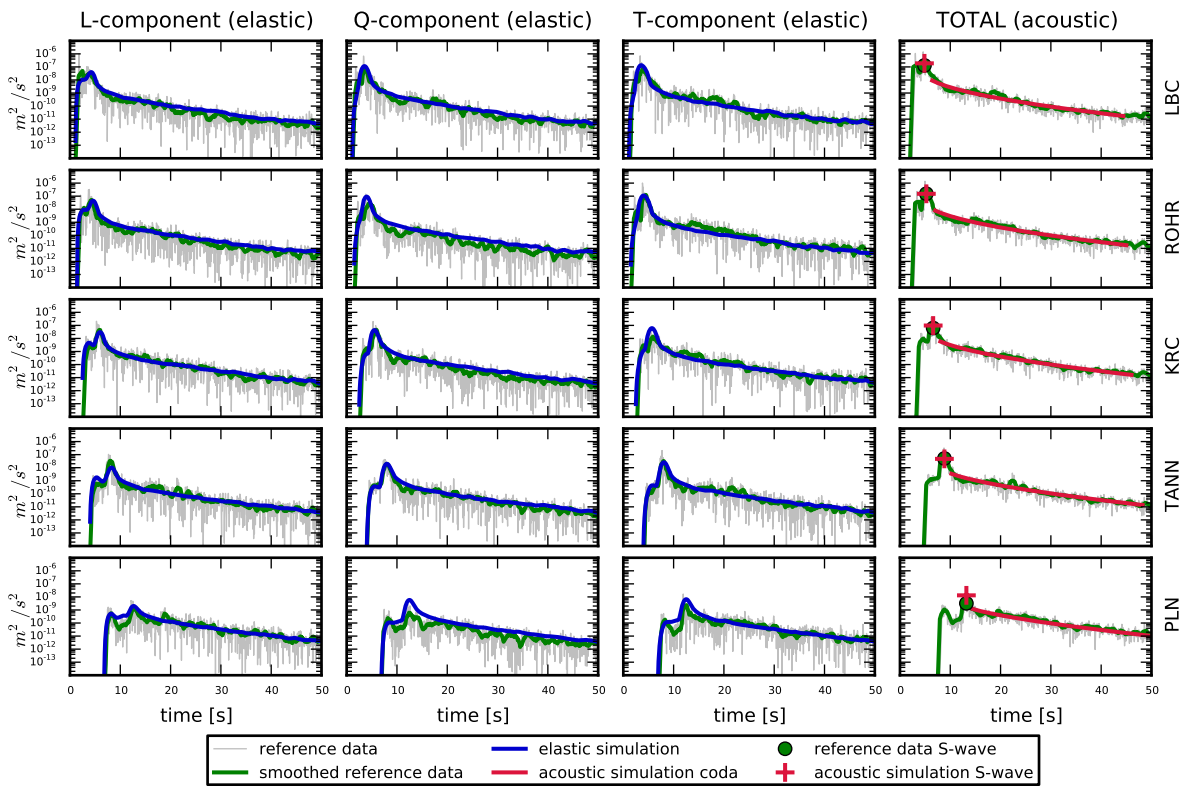

Figure 6.2: Comparison of local reference data with elastic and acoustic simulations. This example shows seismic data from earthquake number 10 (see figure 6.1 and table 6.1) recorded at the stations LBC, ROHR, KRC, TANN and PLN (see figure 6.1 and table 6.2). Data is filtered in the 4-8 Hz frequency band ($f_c = 6$ Hz). Thin gray lines represent reference envelopes, green lines represent the smoothed reference envelopes. Columns 1 to 3 show envelopes for the three components (L, Q and T) modeled with elastic radiative transfer theory (blue line). Column 4 contains the total energy envelopes computed with acoustic radiative transfer theory (red line). The mean amplitude of the direct S-wave energy for reference and acoustic simulations is represented by the green dot and the red cross, respectively.

For each individual earthquake in the four different frequency bands the crustal scattering and attenuation parameters are now determined from fitting the envelopes of elastic and acoustic RTT simulations to the reference envelopes. The resulting parameters are presented in figure 6.3, the average values for the scattering and attenuation parameters are given in table 6.3 for the different frequency bands.
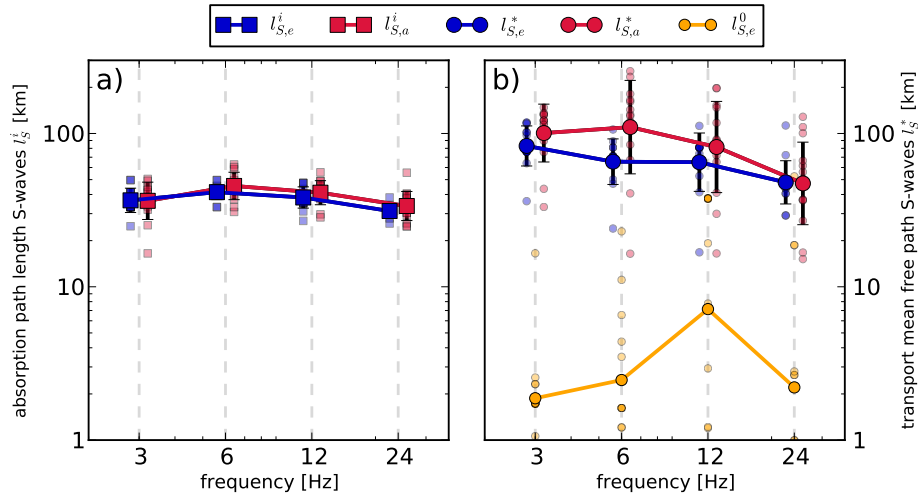

Figure 6.3: Attenuation and scattering parameters from elastic and acoustic radiative transfer theory for the four investigated frequency bands. Left side (a) shows the absorption path length for S-waves l_S^i, right side (b) shows the transport mean free path of S-waves l_S^*. Blue color indicates results computed from elastic theory, red color represents acoustic theory. Symbols in the background indicate the results for each individual earthquake, large symbols represent the logarithmic mean. In addition to the transport mean free path, the mean free path for S-waves estimated from elastic theory $l_{S,e}^0$ is shown in the right side in golden color (see section 6.3.2 for a discussion of this parameter). Subscripts e and a denote elastic and acoustic radiative transfer theory, respectively.

The elastic method yields values from 41 km in the 6 Hz band down to values of 32 km in the 24 Hz band for the absorption path length l_S^i. In the acoustic case values for l_S^i vary from 34 km (24 Hz) up to 45 km (6 Hz). Considering the fluctuations of the estimates from the different earthquake, the results obtained from the both methods for the intrinsic attenuation are in good agreement. Deviations of the individual values to the average values are slightly higher in the acoustic approach than in the elastic method (table 6.3).

In the elastic case the transport mean free path of S-waves l_S^* reaches values from up to 90 km in the 3 Hz frequency band to values of as low as 50 km in the 24 Hz band. These values transfer to scattering attenuation factors for S-waves Q_{sc}^S of 543 (3 Hz)

up to 2417 (24 Hz). The scattering attenuation factor for S-waves Q_S^{sc} is defined as:

$$Q_S^{sc} = \frac{2\pi f l_S^*}{v_s}.\tag{6.7}$$

The acoustic approximation predicts transport mean free paths for S-waves l_S^* of 100 km in the 6 Hz frequency band down to values of 47 km in the 24 Hz band. Corresponding scattering attenuation quality factors Q_S^{sc} range from 610 (3 Hz) up to 2272 (24 Hz). As for the intrinsic attenuation, the scattering attenuation parameters estimated from the two different methods agree fairly well. Also here the acoustic results show larger scatter than the elastic results. It can be concluded, that intrisic attenuation is dominant in the investigated frequency bands and in the chosen epicentral distances of up to 40 km.

frequency [Hz]	l_S^i [km] (Q_S^i)		l_S^* [km] (Q_S^*)	
	elastic	acoustic	elastic	acoustic
3	38 (230)	36 (217)	90 (543)	101 (610)
6	41 (496)	45 (546)	66 (797)	110 (1329)
12	38 (919)	41 (992)	66 (1595)	82 (1982)
24	32 (1538)	34 (1639)	50 (2417)	47 (2272)

Table 6.3: Crustal scattering and attenuation parameters in the Vogtland region. Mean free absorption path for S-waves is denoted as l_S^i, the scattering transport mean free path is given as l_S^*. Quality factors for intrinsic attenuation and scattering Q_S^i and Q_S^* are given in round brackets.

From the estimated values of the transport mean free path in the different frequency bands information about the ACF describing the random medium can be obtained. Assuming a von Karman type of medium, the Hurst parameter ν, which describes the roughness of the medium (equation 2.4a) can be estimated according to following equation (Przybilla and Korn, 2008):

$$l_S^* = f^{2\nu-1}\tag{6.8}$$

Equation 6.8 yields $\nu = 0.38$ from the elastic results and a value of $\nu = 0.35$ from the acoustic results. In the elastic simulations an exponential ACF of the medium is assumed, which is a special case of the von Karman type medium with $\nu = 0.5$. The estimated values from both methods are close to the value of 0.5 of an exponential ACF type medium and therefore justify our assumption of this type of medium in chapters 6, 7 and 8. Figure 6.4 shows the frequency dependence of the transport mean free path for S-waves for both methods with the weighted least square fit resulting in following equations:

$$l_{S,e}^* \sim 107 \left(\frac{f}{Hz}\right)^{-0.24}\tag{6.9}$$

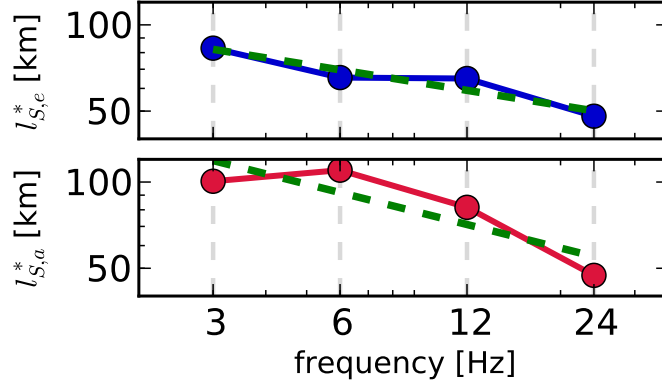$$l_{S,a}^* \sim 178 \left(\frac{f}{Hz}\right)^{-0.30}\tag{6.10}$$

Figure 6.4: Hurst parameter estimation from the transport mean free path. Transport mean free path estimates from elastic (top) and acoustic (bottom) simulations for the four investigated frequency bands. Green dashed lines indicate the weighted least square fit to obtain the Hurst parameter ν, describing the roughness of the medium (equations 6.9 and 6.10). Subscripts e and a denote elastic and acoustic radiative transfer theory, respectively.

6.3.2 Parameter trade-offs and resolution limits

Additionally to the seperation of of scattering and intrinsic attenuation, the data set is used to investigate the parameter trade off between fluctuation strength and correlation length, as well as obtain information about the resolution limits of the mean free path of S-waves l_S^0. The mean free path is a measure of the characteristic distance between two scattering events.

It is shown, that it is not possible to individually resolve the parameters ϵ and a. Only the parameter of the transport mean free path, which results from a combination of these two parameters as a trade-off, can be estimated. This trade-off was already described in earlier studies, see for example (Przybilla et al., 2009). In this study the trade-off is demonstrated by comparisons of elastic RTT simulations with a reference dataset, which was already used in section 6.3.1. Additional elastic simulations are computed for different correlation lengths a and fluctuation strengths ϵ. The parameter a is uniformly spaced between 0 and 2 km, ϵ is in the range from 0 to 10 %. Intrinsic attenuation is kept constant at a value of $Q_S^i = 600$ to be able to only investigate the effect of scattering attenuation. The center frequency is 6 Hz, which results in a absorption path length l_S^i of ~ 50 km. For all the different sets of parameters, the forward simualtions are computed according to section 4.7.1. Reference envelopes are created from earthquake 10 in the 4–8 Hz frequency band and the misfits to the forward simulations are calculated according to equation 6.3. The resulting misfit surface for the parameter sets is shown in figure 6.5.
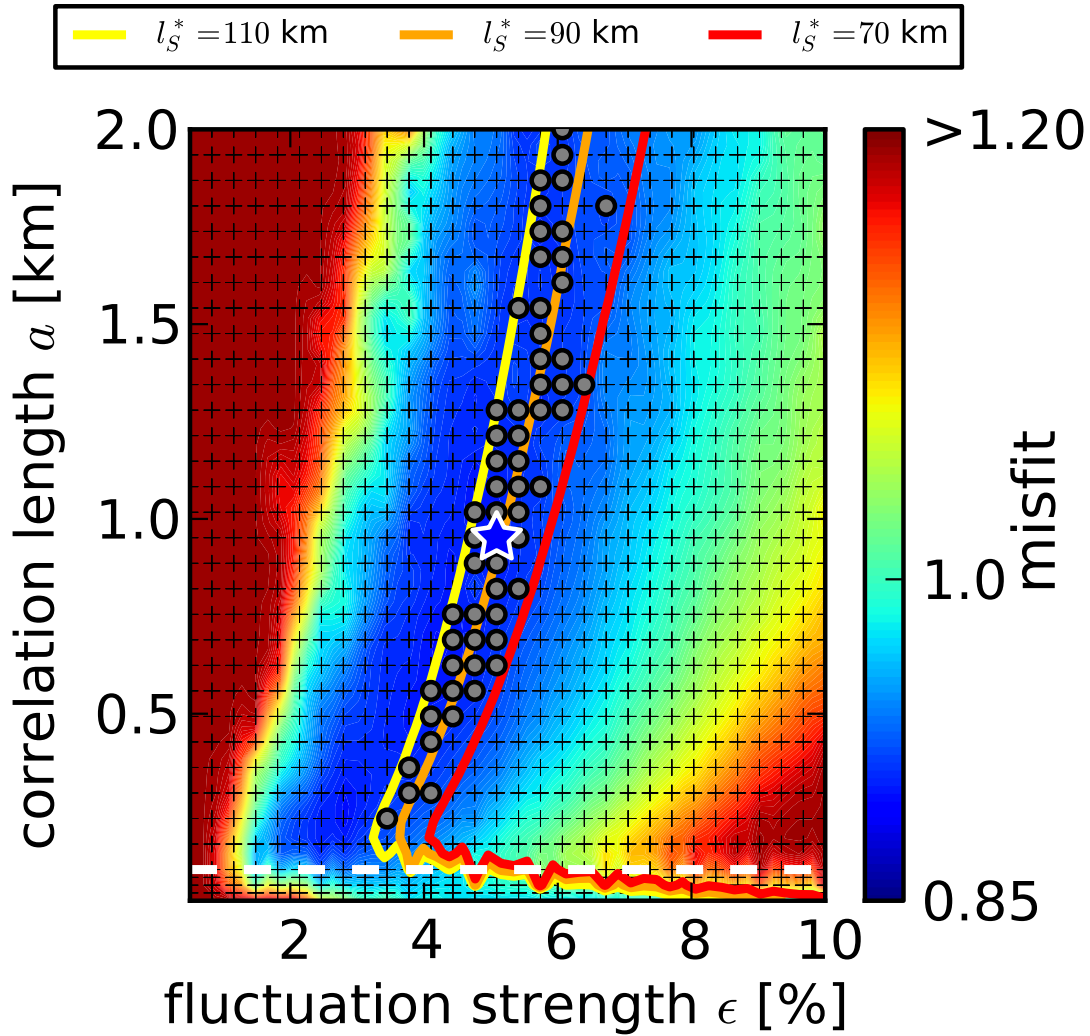
Figure 6.5: Resolution limits of correlation length a and fluctuation strength ϵ. This figure shows the misfit value for different pairs of correlation length a and fluctuation strength ϵ. Light crosses represent elastic RTT simualtions with different sets of a and ϵ. Intrinsic attenuation l_S^i is constant for all simulations, center frequency is 6 Hz. The simulation with the lowest misfit is represented by the blue star, grey dots represent simulations with similar misfits. Dashed white line indicates $a_{ks}=1$. Yellow, orange and red lines represent isoline of the tmfp for 110, 90 and 70 km, respectively.

A number of simulations with misfits comparable to the best simulation can be observed, those simulations are marked with grey dots. In the elastic simulations some weak fluctuations, especially in the coda window, can be observed. This fluctuations are caused by the limited number of particles used in the simulations and can cause

statistical variations that influence the resulting misfit (see section 7.1.2). The simulations all have different pairs of correlation lengths and fluctuation strengths, but share a similar value for the transport mean free path length. This is illustrated in figure 6.5, where additionally to the color coded misfit, the transport mean free path is illustrated as colored isolines. The best fitting models align along similar values of l_S^* ranging between 70 -110 km. The total energy traces (L+Q+T) of these simulations, as well as the total energy reference envelope from station KRC for event 10 in the 4–8 Hz band is shown in figure 6.6. The main differences in the traces of the simulations with similar transport mean free paths can be observed in the coda following the S-wave. These differences are accounted for by fluctuations in the individual simulations due to the limited number of particles used. The direct onsets of the P- and S-wave show only small differences and are nearly equal for simulations with similar transport mean free paths. From figure 6.6 it can be concluded, that forward scattering is required to describe the reference data. All simulations with low misfit values have an ak_s value of greater than 1, which implies forward scattering. Higher misfits are visible for all simulations with ak_S values below 1, which would imply isotropic scattering. Even though forward scattering is required, the strength of the forward scattering, described by the value of ak_s, cannot be determined.
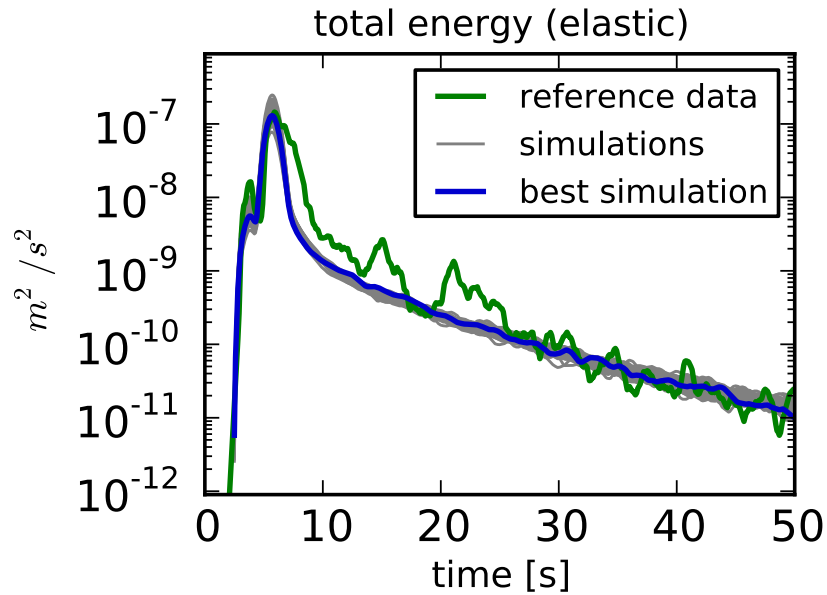

Figure 6.6: Total energy envelopes of smoothed reference data (green line) and best fitting elastic simulation (blue) for earthquake 10 at station KRC in the 4–8 Hz frequency band. Thin grey lines represent the simulations, that can equally well describe the reference envelopes (figure 6.5)

From the elastic and acoustic simulations information about the resolution possibilities and limits of the mean free path l_S^0 can be obtained. In figure 6.3 the estimated values

of l_S^0 from the elastic simulations are presented additionally to the transport mean free path. The deviations of l_S^0 are in the range from far below 1 km up to 40 km and therefore show much higher uncertainty than l_S^*. This fact is also supported by figure 6.7, which shows the misfit values of the simulations already shown in figure 6.5, but for the different values of transport mean free path and mean free path. Note, that it is possible to estimate the transport mean free path with a high accuracy and to narrow it down to a range between 70–110 km. The mean free path on the other hand, cannot be estimated reliably as the values from the simulations with low misfits range from a few hundred meters up to over 40 km.
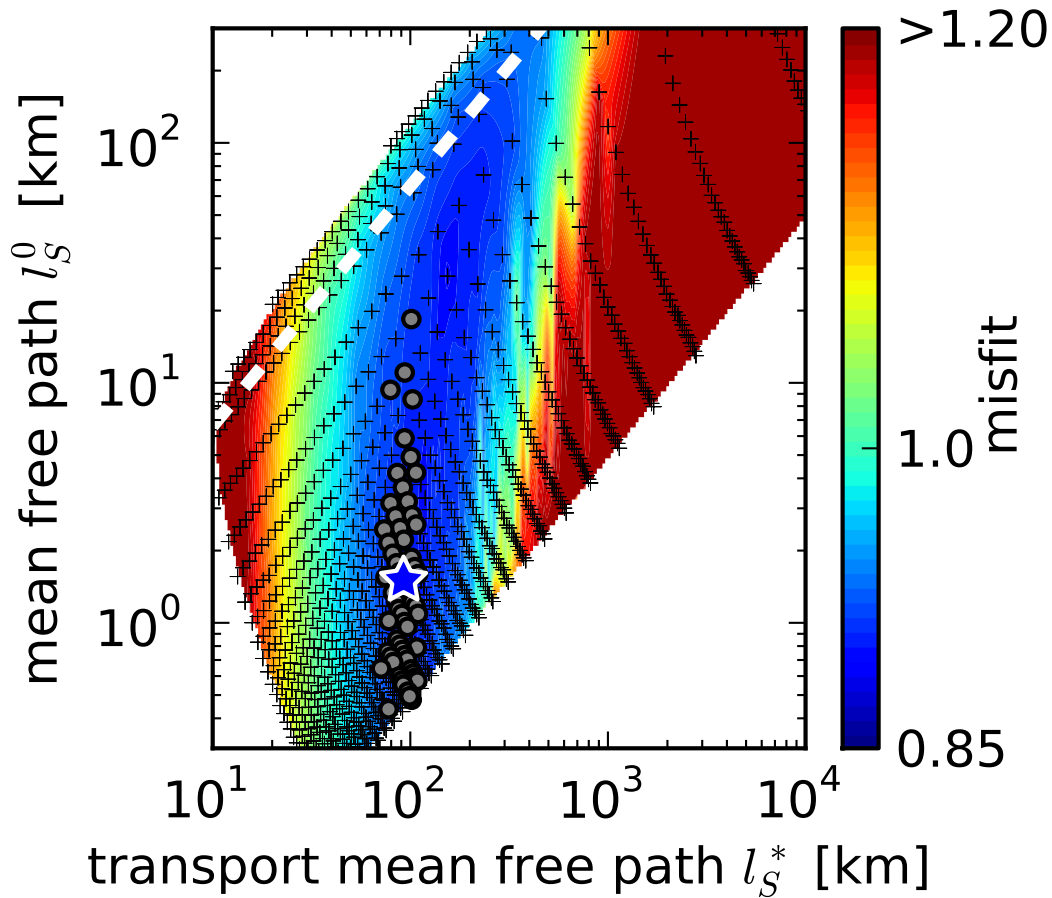

Figure 6.7: Similar to figure 6.5, but for the different pairs of transport mean free path and mean free path. Light crosses represent elastic RTT simulations. The simulation with the lowest misfit is represented by the blue star, grey dots represent simulations with similar misfits. Dashed white line indicates $a_{ks} = 1$. Simulations above the white line have a value of ak_s greater than 1 and therefore are in the isotropic scattering regime.

7 Inversion of regional envelopes for attenuation and scattering parameters

In this application swarm earthquakes from the Vogtland region (eastern Germany) are recorded on a regional scale and inverted for scattering and attenuation parameters of the random medium representing the crustal material beneath the Gräfenberg array in south-east Germany. Reference seismogram envelopes of different epicentral distances are used and compared to forward simulations using elastic MC-RTT (section 4.7.1). The estimated parameters are then used in section 8 to model translational and rotational motion seismogram envelopes for teleseismic arrivals and compare them to records from deep teleseismic events recorded in the Gräfenberg array area. The genetic inversion algorithm, that estimates the best fitting parameters is detailed and tested in section 7.1. The inversion setup, including the used data, starting parameters for the inversion and the creation of the reference seismogram envelopes is described in section 7.2. The results of the inversion of the the regional earthquakes are further presented in section 7.3.

7.1 Genetic inversion approach

This section details the genetic algorithm used for the inversion (section 7.1.1) and presents a test of the algorithm using synthetic seismogram envelopes in section 7.1.2.

7.1.1 Basic information

In the inversion process of the regional data a genetic approach is used, for example described by Goldberg (1989). According to Mitchell (1996) the most basic form of a genetic inversion algorithm features three different operations: selection, crossover and mutation, which in the field of seismology can be explained as following. The selection operator selects a set of parameters describing a random medium, which in the next step will be subject to the crossover or mutation operation. The fitter the

set of parameters is, i.e. the better the parameters describe the data, the greater the chance that it is selected in the next iteration. In this study fit sets of parameters result in small misfit values (compare equation 6.3) and therefore give a good approximation of the reference data. The crossover operation exchanges single parameters of two fit parameter sets and mimics the process of biological recombination. The operation of mutation randomly changes single parameters in a parameter set. An overview of the inversion approach is shown in figure 7.1.
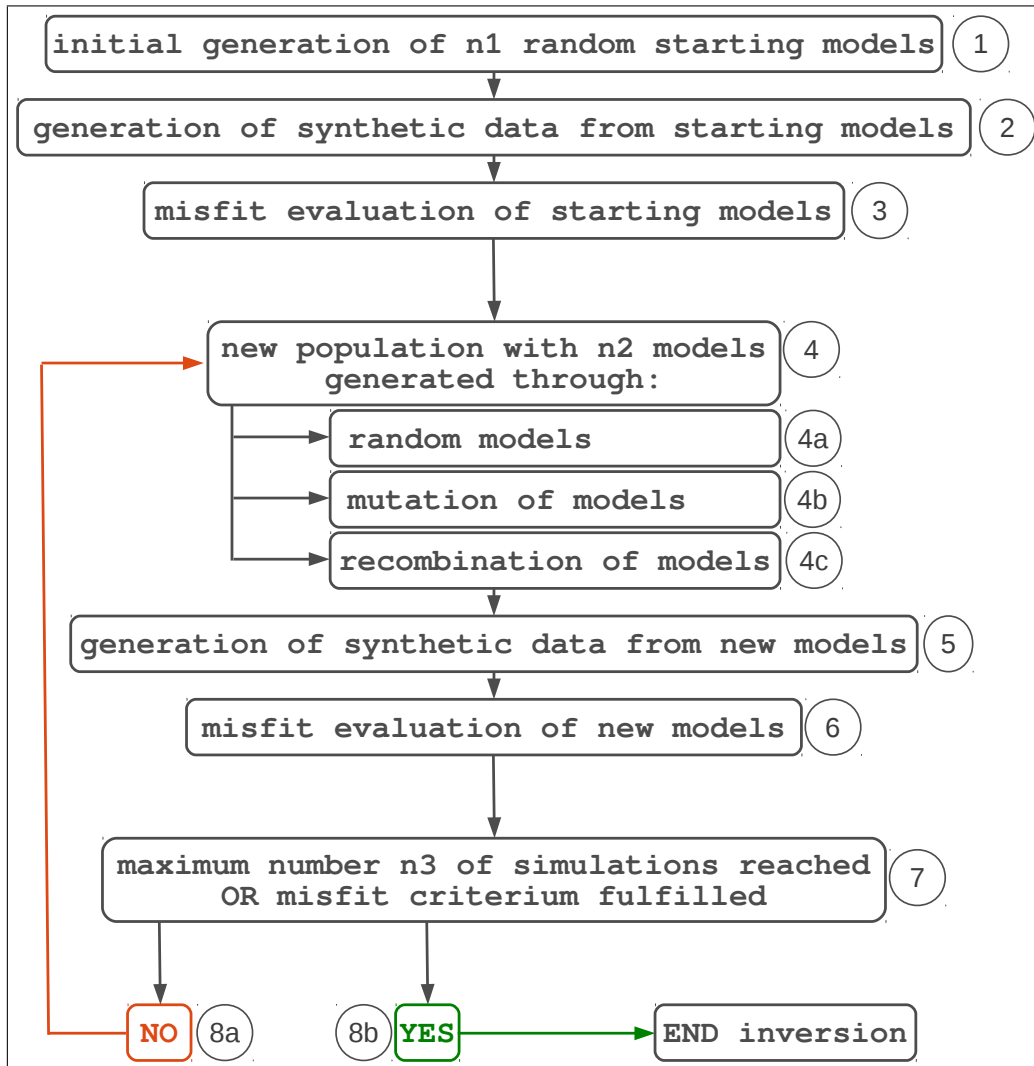

Figure 7.1: Flowchart of the genetic inversion algorithm.

The inversion approach starts off with a first population of models consisting of *n1* random starting models (1). These starting models are generated by random alternation of starting values within a certain range. The starting values for the individual parameters (for example fluctuation strength or correlation length of the medium) are set to reasonable values obtained from the literature. For these *n1* starting models,

the forward simulations are calculated using MC-RTT simulations (2) and are compared to reference traces (3) (for example a synthetic data set or real data reference seismogram envelopes). The evaluation of the starting models (1-3) is the first cycle in the inversion process. In each of the following iteration cycles a new population of *n2* models is created (4). This is achieved by the generation of completely new random models similar to the starting models (4a). Random models are created throughout the inversion process in each iteration cycle to enforce sampling of the entire model parameter space. Furthermore in each iteration cycle new models are created via the mutation of individual parameters from parameter sets that yield a good fit (4b) in the evaluation of the misfit. Mutation ensures the creation of models in the vicinity of minima in the misfit function. Recombination (4c) describes the process of combining individual parameters from fit models to obtain new models which are located close to other good models in the parameter space. Recombination also ensures the dense sampling space in the vicinity of good models. Forward models are calculated from the new model population (5) and evaluated in terms of their fitness (6). The generation of new model populations is repeated (8a) until a maximum number *n3* of models is investigated (7). This criteria ends the inversion process (8b). Alternatively the inversion process can be terminated earlier, when one set of parameters results in a misfit value falling below a predefined threshold value (7). This also stops the inversion process (8b). The inversion process is implemented in the *Python* programming language.

7.1.2 Synthetic test of the inversion algorithm and statistical variations

The genetic inversion algorithm was subject to testing using a synthetic data set on a regional distance scale. The synthetic reference seismogram envelopes were computed using MC-RTT simulations in accordance to section 4.7.1 for distances of 60, 100 and 140 km and for the three components of translations in the LQT system. Reference traces are shown in figure 7.2. The reference model consists of a layer over half space, the top layer represents the crustal part, the half space represents the mantle. Crust and mantle are separated by a boundary in a depth of 30 km. Velocities of P- and S-waves v_P and v_S in the crust are set to 6.0 km/s and 3.46 km/s, respectively . In the mantle the velocities are 7.6 km/s and 4.4 km/s, respectively. The random medium representing the crust and mantle has an exponential ACF. Fluctuation strength in the crust ϵ_{crust} is 5 per cent, in the mantle the fluctuation strength ϵ_{mantle} is set to 2 per cent. Correlation length a_{crust} and a_{mantle} are 4 km and 2 km, respectively. Intrinsic attenuation of S-waves Q_S^i in the crust is set to 600 with a fixed Q_P^i to Q_S^i ratio of 2.25 (Shearer, 1999). The intrinsic P-wave attenuation Q_P^i in the mantle is set to 1070, with Q_S^i in the mantle being 475. An isotropic source with an energy ratio of radiated P- and S-energy of ~ 0.05 (Shearer and Earle, 2008) is used. The source is placed in the crustal part of the model in a hypocenter depth of 10 km. The simulations are carried out at a frequency of 2 Hz. In the inversion process fluctuation strength of

both crust and mantle are estimated, as well as the intrinsic attenuation of the crustal part of the model. The remaining parameters, intrinsic attenuation of the mantle and correlation length of crust and mantle, are set to the *true* values, mentioned above. As starting values for the inversion 2 % is chosen for the crustal velocity fluctuations, 7 per cent for the fluctuations in the mantle and an intrinsic attenuation value for S-waves of 2222. More than 2000 models were created in the inversion run with different sets of parameters (ϵ_{crust}, ϵ_{mantle}, $Q_S^i(Q_P^i)$ crust). The best fitting model has a fluctuation strength of 5 per cent in the crust, an intrinsic attenuation value for S-waves Q_S^i in the crust of 584 and a fluctuation strength of 2.8 per cent in the mantle. The best model is shown in figure 7.2 in comparison with the reference simulations. Misfits between the simulations and the synthetic reference envelopes are calculated according to equation 6.3.
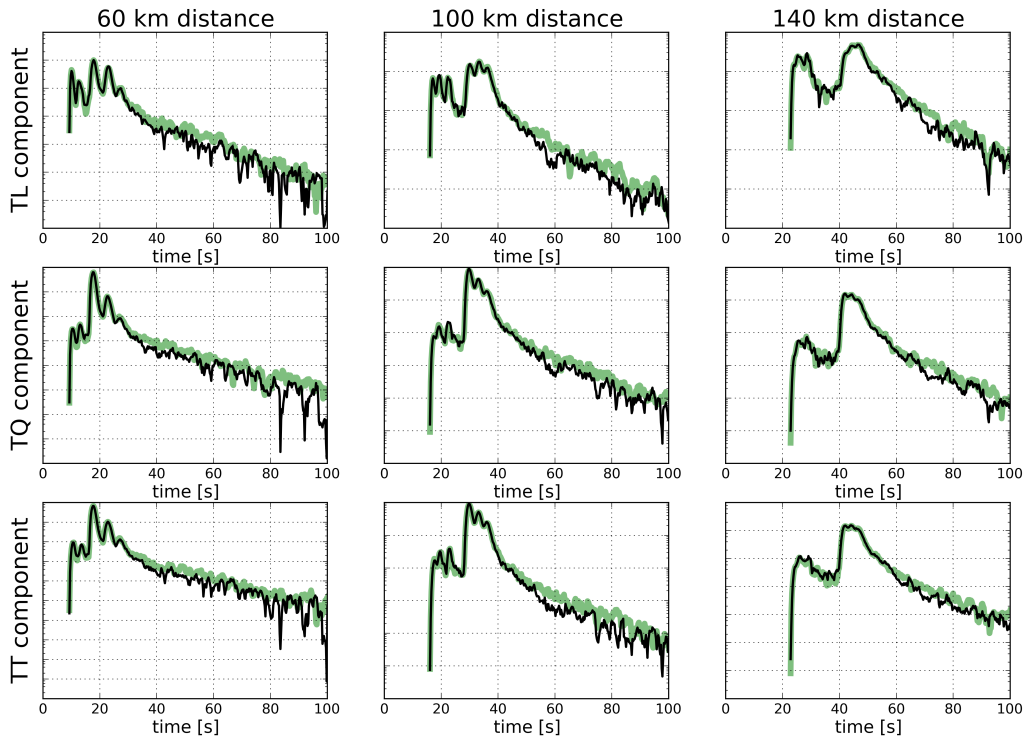

Figure 7.2: Synthetic inversion test: reference vs. best fitting envelopes. Shown are the reference envelopes of the inversion process (green) and the envelopes resulting from the model with the smallest misfit (black). Distances are 60, 100 and 140 km (left to right column) for the different components of translational motions in the LQT system (top to bottom row).

Table 7.1 gives an overview of the true, starting and estimated values from the inversion.

	Q_S^i (crust)	ϵ_{crust} [%]	ϵ_{mantle} [%]
true	600	5.0	2.0
starting	5000	2.0	7.0
estimated	584	5.0	2.8

Table 7.1: Starting, true and estimated values in the synthetic inversion.

In figure 7.2 a very good agreement between the reference seismogram envelopes and the envelopes calculated from the best fitting model can be observed from the first onset of the direct P-wave until the late seismic coda. Fluctuations in the coda of the envelopes can be observed and will be subject of investigation at the end of this section. From table 7.1 it can be observed, that the crustal scattering and attenuation parameters are inverted nearly perfectly, while the scattering parameter in the mantle is harder to resolve. This is due to the fact that scattering in the mantle does not contribute strongly to the simulated envelopes due to the small influence of the mantle on wave propagation on a regional scale. This fact can also be observed in figures 7.3a and 7.3b. The figures show the misfit surfaces for two pairs of free parameters: Q_P^i versus ϵ_{crust} and ϵ_{mantle} versus ϵ_{crust}.

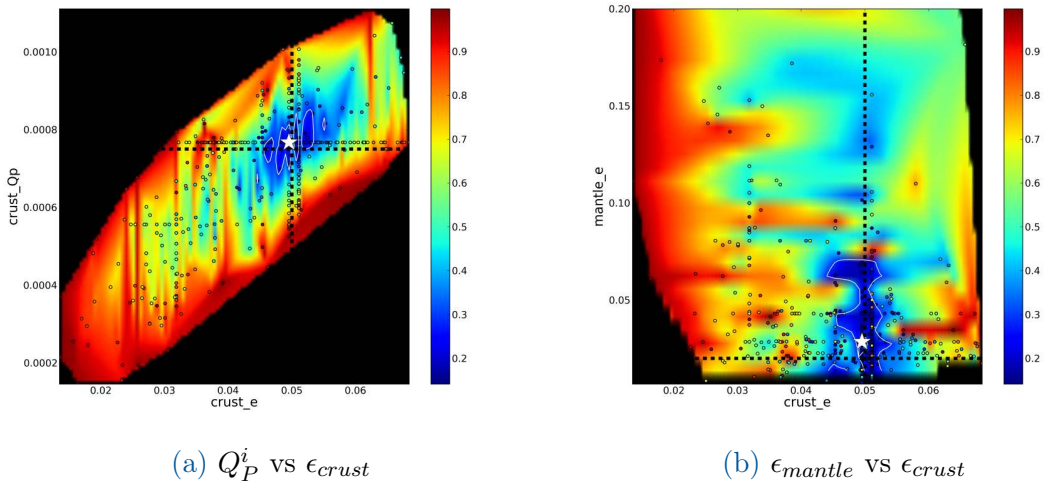(a) Q_P^i vs ϵ_{crust} (b) ϵ_{mantle} vs ϵ_{crust}

Figure 7.3: Misfit surfaces for two different parameter pairs. (a) Misfit surface for Q_P^i versus ϵ_{crust}. (b) Misfit surface for ϵ_{mantle} versus ϵ_{crust}. Blue colors indicate small misfit values and therefore fit models, red colors represent models with high misfit values. White indicate the best model found in the inversion, dashed black lines represent the true parameters. Each small circle represents one set of parameters. White lines indicate models, that can explain the reference data equally well. Black dots indicate individual forward simulations.

It is clearly visible from figure 7.3a that the crustal parameters ϵ and Q_P^i (Q_S^i) can

be estimated quite well and that there is a distinct minimum in the misfit function. The mantle parameter (figure 7.3b) ϵ is harder to resolve and no distinct minimum in the misfit function can be observed. This suggests a weak influence of the mantle scattering properties on the regional wave propagation and on the outcomes of the MC-RTT simulations. From the synthetic test it can be concluded, that the inversion algorithm is implemented correctly and can be used in a real data application.

Looking at the coda in figure 7.2 some strong fluctuations can be observed in the simulations. The fluctuations result from the limited number of particles used in the MC-RTT simulations due to computational reasons. Together with the geometrical spreading, the lack of particles causes statistical variations which have to be considered in the evaluation of the model fitness. Fluctuations get stronger for longer lapse times and larger distances. Figure 7.4 shows a comparison of a reference simulation with ten simulations with identical model parameters. For the reference simulation ten times more particles are used in the computation of the envelopes.
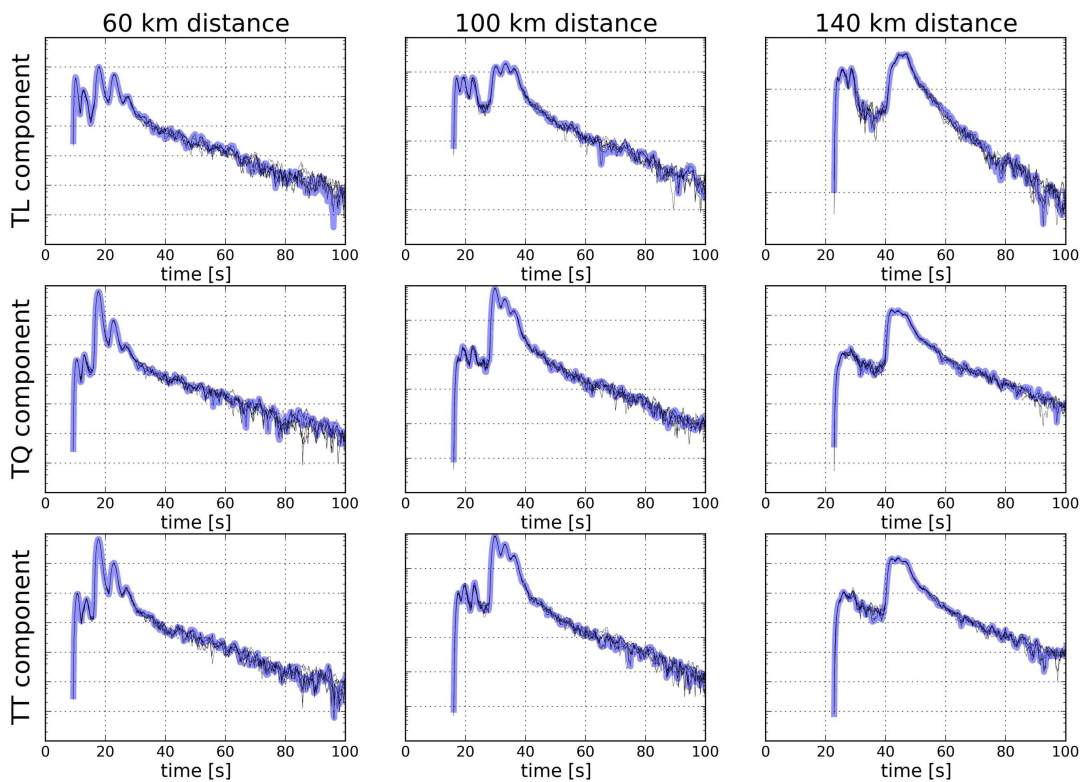

Figure 7.4: Statistical fluctuations in the MC-RTT simulations results. Reference simulation (blueish) with ten simulations with identical model parameters (thin black) are shown. Especially in the coda, fluctuations can be observed, that have to be considered in the misfit calculation. Distances are 60, 100 and 140 km (left to right column) for the different components of translational motions in the LQT system (top to bottom row).

Clear fluctuations are visible especially in the coda of the seismogram envelopes. A computation of the misfits between the ten simulations and the reference simulation is shown in figure 7.5. The fact, that misfits already exist for models with identical model parameters, shows the existence of a forward modeling error that has to be considered in the interpretation of the best model in the simulations. Models that have misfits in a certain confidence interval also have to be considered as the best possible model, even if the misfit is higher. This models are encircled in figures 7.3a and 7.3b with white lines.
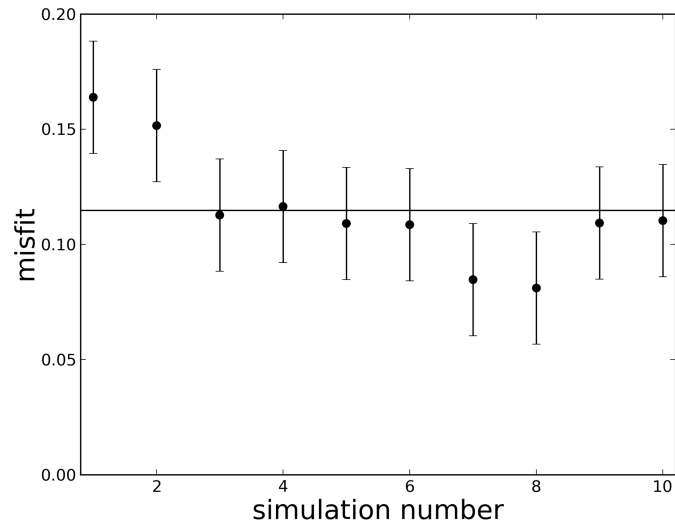

Figure 7.5: Forward modeling error in the MC-RTT simulations. This figure shows the misfit values between a reference simulation and ten other simulations with identical model parameters. These misfits indicate a forward modeling error, that has to be accounted for in the interpretation of the best model.

7.2 Inversion setup

This section describes the study area and gives information about the sources and receivers used in the inversion of regional seismogram envelopes in section 7.2.1. The parameter setup and the generation of the reference seismogram envelopes for the inversion is presented in section 7.2.2.

7.2.1 Study area and data

The region of interest in the regional application is in the south-eastern part of Germany close to the border of the Czech Republic, in particular the subsurface beneath the Gräfenberg array (figure 7.6). The stations of the Gräfenberg array (GR) are deployed at remote sites on a plateau of the Frankonian Jura. This formation is made

of comparatively homogeneous Upper Jurassic Limestone and is overlain by a sedimentary wedge of varying thicknesses between 400 and 1150 m (Krüger, 1994). The lithospheric basement of this formation belongs to the Variscian Belt (Franke, 1989). A crustal thickness of about 30 km is estimated by Zeis et al. (1990) for the Gräfenberg area with a total lithospheric thickness between 80-100 km (Mueller and Panza, 1986). The station in Wettzell (WET) in the eastern part of the study area is directly deployed on bedrock gneisses (Klügel et al., 2001).
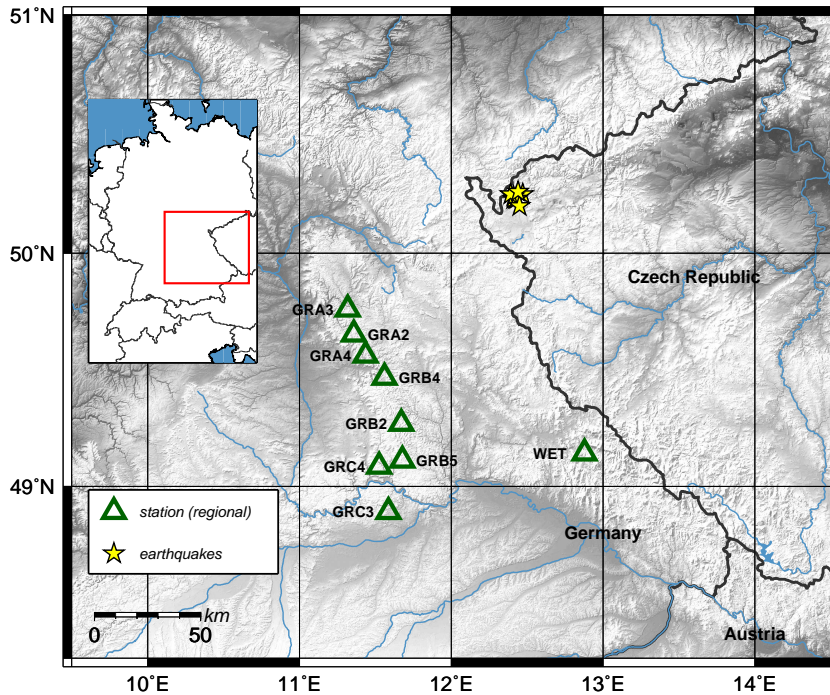

Figure 7.6: Study area in the regional data investigations. The map shows the southeastern part of Germany. Stations used in the inversion of the regional earthquakes are shown in green triangles. Swarm-earthquakes in the Vogtland area are given as yellow stars. Grey shading indicates topography.

To create the reference seismogram envelopes for different epicentral distances, swarm earthquakes of moderate magnitude in the Vogtland region are used. Eight earthquakes with magnitudes M_L between 3.0 and 4.0, that occurred during the swarm activity in August 2011, are used. The events have a hypocenter depth between 4 and 9 km. The distribution of the earthquakes is shown in figure 7.6, more details about the earthquakes are given in table 7.2.

The earthquakes are recorded at seven stations of the Gräfenberg array and additionally at the station Wettzell (WET). The GR stations are part of the Seismological Central Observatory (SZO) operated by the Federal Institute for Geosciences and Resources (BGR). The station WET is part of the German Regional Seismic Network (GRSN) and is operated by the geodetic observatory in Wettzell. This station is included in the inversion process, as in chapter 8 the vertical rotation rate observed at that station

region	UTC-time	mag	lon [°]	lat [°]	d [km]
Vogtland	2011-08-28-06-45-08	3.0	12.47	50.25	4
Vogtland	2011-08-26-15-27-24	3.1	12.41	50.24	6
Vogtland	2011-08-26-06-54-05	3.6	12.42	50.23	5
Vogtland	2011-08-26-06-15-45	3.3	12.41	50.23	6
Vogtland	2011-08-26-00-35-02	3.2	12.43	50.23	4
Vogtland	2011-08-26-00-15-34	3.4	12.39	50.25	5
Vogtland	2011-08-25-23-33-21	4.0	12.45	50.20	9
Vogtland	2011-08-25-23-05-41	3.6	12.44	50.26	5

Table 7.2: Swarm earthquakes used in the regional inversion. *lon* indicates longitude, *lat* indicates latitude and *d* represents depth. The magnitude of the event is given by *mag*.

will be subject to further investigations. All stations are equipped with broadband, three component STS-2 seismometers. Station distribution is shown in figure 7.6, more details about the stations are presented in table 7.3.

network	station	lon [°]	lat [°]	seismometer
GR	GRA3	11.32	49.76	STS-2
GR	GRA2	11.36	49.66	STS-2
GR	GRA4	11.44	49.57	STS-2
GR	GRB4	11.56	49.47	STS-2
GR	GRB2	11.67	49.27	STS-2
GR	WET	12.88	49.14	STS-2
GR	GRB5	11.67	49.11	STS-2
GR	GRC4	11.53	49.09	STS-2
GR	GRC3	11.59	49.89	STS-2

Table 7.3: Stations used in the regional inversion. *lon* indicates longitude and *lat* indicates latitude.

7.2.2 Parameters for the inversion and reference envelopes

The forward simulations of the synthetic data in the inversion process are calculated using the MC-RTT approach for local and regional earthquakes described in section 4.7.1. To simulate translational LQT snapshots of the wave field the seismic energy is recorded in the LQT system in a domain with lateral size of 400×400 km. Note, that there are no boundary effects in the simulations, as for example absorbing boundary conditions used in the FD simulations in chapter 5. The particle propagation is modeled throughout the full time interval irrespective of the particle location. In the vertical direction a 30 km thick crust overlaying a half space representing the mantle is modeled. The

random velocity and density fluctuations are described by an exponetial ACF of the random medium. Velocities of P- and S-waves in the crust are set to 5.6 km/s and 3.31 km/s, in the mantle the velocities are 7.7 km/s and 4.5 km/s. The source is placed in the center of the model at a depth of 5.5 km, which is the mean depth of the swarm-earthquakes used here (table 7.2). The lateral dimensions and the placement of the source allow to compute azimuthally stacked cross sections in the distance range from 0 to 200 km. A source with an isotropic radiation pattern is chosen as the reference envelopes are created from averaging over different earthquakes that will equilibrate the source radiation pattern. A center frequency for the source of 6 Hz is chosen. The energy ratio between radiated P-and S-energy is fixed at $\sim$0.05 (Shearer and Earle, 2008). In principal there are eight free parameters in the inversion: fluctuation strength ϵ, correlation length a, the intrinsic quality factor Q_S^i for S-waves and Q_P^i for P-waves in the crust, and in the mantle respectively. In the actual inversion process the number of free parameters is limited, as it is computationally not feasible to invert for all eight parameters. Parameters in the mantle are fixed to fluctuation strength $\epsilon = 0.5$ %, correlation length $a = 4\ km$ and $Q_S^i = 475$ ($Q_P^i = 1070$) according to Sens-Schönfelder et al. (2009). It is inverted for the crustal parameters of fluctuation strength ϵ, the correlation length a, as well as for the intrinsic attenuation values for P- and S-waves Q_P^i and Q_S^i. Here it is not inverted for Q_P^i and Q_S^i separately, but for Q_S^i with a fixed ratio of Q_P^i to Q_S^i of 2.25 (Shearer, 1999). This leaves three free parameters. As crustal starting values $\epsilon = 0.5$ %, $a = 2$ km and $Q_S^i = 600$ are chosen. ($Q_P^i = 1350$) (Sens-Schönfelder et al., 2009; Dziewonski and Anderson, 1981).

Reference seismogram envelopes are calculated for the events given in table 7.2 recorded at the stations detailed in table 7.3. The computation of the reference seismogram envelopes involves processing of individual records, the estimation of correction factors for site amplification and event size and finally the stacking of records from different events. For the processing of individual records the following steps are performed:

1. Demeaning of the traces.

2. Instrument response removal.

3. Bandpass filtering (4–8 Hz).

4. Distance correction (stretching).

5. Subtraction of noise level.

6. Rotation from ZNE into the LQT system.

7. Calculation of Hilbert envelopes.

8. Smoothing of the envelopes.

The correction of the instrument response is done to enable broadband comparison of absolute amplitudes of translational and rotational measurements. A distance corrections for each station-earthquake pair is necessary, as different earthquakes with slightly

variable epicentral distances (less than 5 %) are stacked to obtain smooth reference seismogram envelopes. The stretching aligns phases of equal slowness ($t' = t(1+(r_0-r)/r)$, with t being lapse time, t' is corrected lapse time, r is epicentral distance and r_0 is the average epicentral distance of events used for stacking). After these processing steps, site amplification factors for the stations and energies of the events are computed with the coda normalization method (CNM) according to Aki (1980) to correct the smoothed Hilbert envelopes. One set of parameters for station corrections and source energies (nine stations and eight events) is obtained from a large number of observations from nine stations and eight events, which transfers to a total of 72 observations. This ensures that even though magnitudes of the events are different they get similar weight in the stacking and maintain consistent relative amplitudes in different epicentral distances. After this correction the seismogram envelopes are stacked to obtain the reference envelopes for the inversion. Reference envelopes R in the LQT system for different epicentral distances represented by the average distance of the different stations to the center of the earthquakes are generated. The closest distance is ∼95 km, the greatest epicentral distance investigated is ∼163 km.

The calculation of the misfits between real data reference envelopes and the MC-RTT forward simulations is according to equation 6.3.

7.3 Results of the inversion

Here the results of the genetic inversion (section 7.2) for crustal scattering and attenuation parameters from the regional swarm-earthquakes are presented. During the inversion process more than 2000 simulations for different sets of parameters (ϵ_{crust}, a_{crust}, Q_P^i (Q_S^i) of the crust) were calculated using the MC-RTT simulations and compared to the reference seismogram envelopes. The simulations cover a model space of roughly $0.1 < \epsilon < 20$ per cent, $100 < Q_S^i < 5000$ and $0.01 < a < 10$ km. The resulting misfit values for the different pairs of parameters ($a - \epsilon, Q_S^i - \epsilon, Q_S^i - a$) are shown in figure 7.7.

The best model, that is the model with the lowest misfit value between reference envelopes and simulations has following crustal scattering and attenuation parameters for a continuous random medium with an exponential ACF: fluctuation strength ϵ= 2.9 per cent, correlation length $a = 0.27$ km and intrinsic S-wave quality factor $Q_S^i = 667$ ($Q_P^i = 1500$). The values of a and ϵ result in a transport mean free path of ∼ 420 km. In figure 7.7 a number of simulations located around the best simulation with misfit values that do not significantly differ from the model with the minimum misfit can be observed. Especially in the parts of the coda of the direct P- and S-waves some weak fluctuations can be observed in the simulations. Due to these statistical variations (section 7.1.2) the resulting misfit for simulations with identical parameters can differ by ∼1.5 %. These differences are a measure of the uncertainties of our simulations. If taking into account these uncertainties of the misfit values, parameters, that
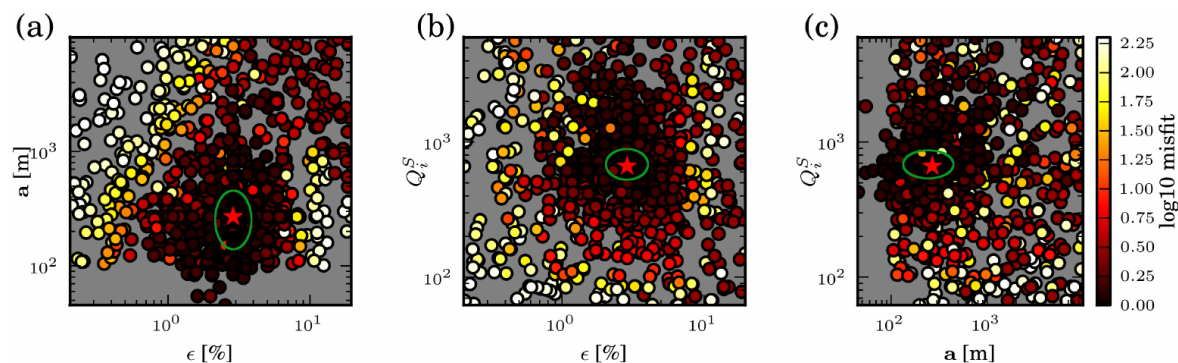
Figure 7.7: Misfit values for different pairs of free parameters in the inversion process. (a) Correlation length a against fluctuation strength ϵ. (b) Intrinsic quality factor Q_S^i against fluctuation strength ϵ. (c) Intrinsic quality factor Q_S^i against correlation length a. Darker colors of the symbols indicate a low misfit value (good model), brighter colors represent a (bad) model with a high misfit value. Misfits are illustrated in a logarithmic scale to increase the contrast for visualization. Misfits are scaled to the simulation with the lowest misfit value (red star). Note the clear area of simulations with low misfit values around the best model. Green ellipses indicates models with misfit similar to the best model (difference $\sim 1.5\%$).

can explain the data equally well, are in the range 2.5 per cent $< \epsilon <$ 3.5 per cent, 0.1 km $< a <$ 0.4 km and $580 < Q_S^i < 750$. These ranges are approximately represented by the green ellipsoids in figure 7.7. In figure 7.8 the comparison of the best model with the reference seismogram envelopes is shown. All stations in the inversion process are shown. Station WET is highlighted in orange as it will further be used for modeling of teleseismic arrivals including rotational motions around the vertical axis (chapter 8).

Some differences can be noticed between the simulations and the reference envelopes, especially for the direct P- and S-wave arrivals and the P-coda. These differences can to a large extent be explained by the isotropic source radiation used in the modeling or by a Q_P^i/Q_S^i ratio that may be different from the theoretical value assumed here. An influence of the radiation pattern is plausible because as it is averaged over different earthquakes while constructing the reference envelopes, but apparently the similarity of the source processes (Fischer et al., 2013) hinders an efficient averaging of the radiation pattern during stacking. In contrast, the coda of the S-wave can be modeled well. The suggested crustal scattering and attenuation parameters are in good agreement with the results of other studies for non-volcanic areas. Especially the comparison to studies by Sens-Schönfelder and Wegler (2006), Sens-Schönfelder et al. (2009), Calvet and Margerin (2013) and Rothert (2000) is of interest, as they investigate scattering and attenuation parameters in similar regions. For a comparison of the estimated attenuation and scattering parameters see table 2.1 and section 2.3.
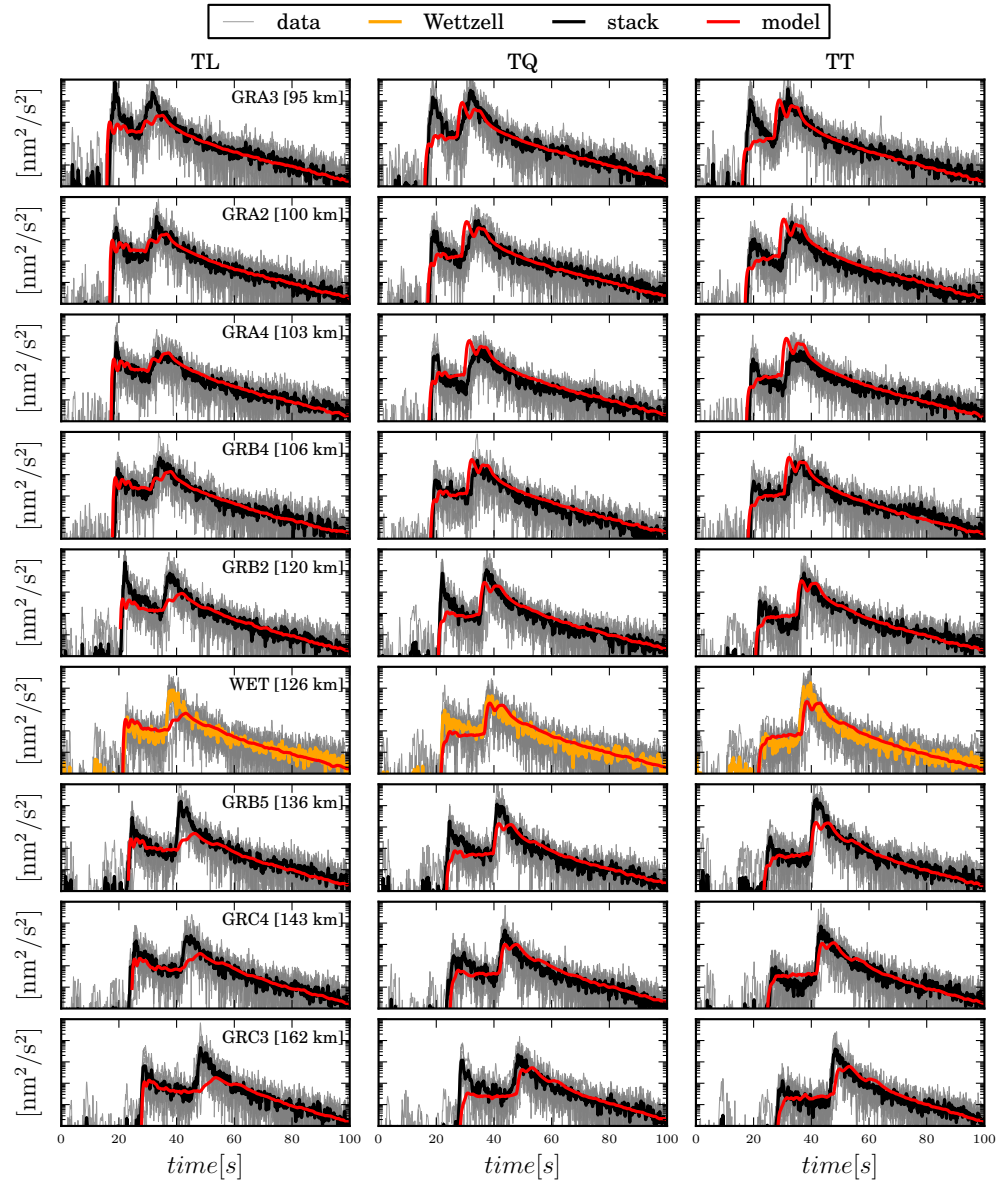
Figure 7.8: Comparison of reference seismogram and simulated envelopes. Best simulations from the regional inversion are shown in red, reference traces are shown in black or orange in the case of WET. This station will further be used in chapter 8 for the modeling and comparison of rotational envelopes from teleseismic events. Rows represent different stations with different epicentral distances increasing from top to bottom, columns show the different components in the ray based LQT coordinate system. Grey lines indicate traces for the individual earthquakes. Units are given in nm^2/s^2 (intensity) and scaled to the coda average at around 80s. The central frequency of the MC-RTT simulations is 6 Hz, the earthquake data is filtered in a frequency band from 4–8 Hz.

8 Simulation of teleseismic records of P- and PcP-coda envelopes

In chapter 7 crustal scattering and intrinsic attenuation parameters were estimated using an established technique of inverting translational motion envelopes from regional, shallow swarm earthquakes. This estimated set of parameters is now used to model translational and rotational motion seismogram envelopes for teleseismic arrivals and to investigate the crustal influence on different seismic scales. The computed envelopes are compared to translational and rotational motion records from deep teleseismic events. The attention is focused the station WET, located at the Fundamentalstation in Wettzell, as this station offers recordings of the three translational motions as well as high-quality measurements of the rotation rate around the vertical axis performed by the ringlaser. The investigated teleseismic events and the stations used for the recording are presented in section 8.1. Some information about the performance of the ringlaser rotational motion sensor are given in section 8.2. The comparison of simulated and observed seismogram envelopes is given in section 8.3.

8.1 Study area and observations

As this chapter compares translational and rotational motion seismogram envelopes from records of the teleseismic P-coda with simulations based on the inversion results from the regional events in chapter 7, this data application consequently covers the same study area, the subsurface beneath the Gräfenberg array in south-east Germany. An overview over the study area, including the station distribution is shown in figure 8.1.

In this application teleseismic events are used instead of the regional earthquakes to investigate the influence of crustal scattering on the teleseismic coda. Four deep teleseismic events in the distance range between 70.8° to 73.3° are used, one event from E-Russia-N-China and three events from the Sea of Okhotsk region. The deep events in this distance range have the advantage, that the crustal structure beneath the receivers is excited by an almost plane wave. As the depth phase pP, that is scattered in the crust at the source side, is excluded, it can be assumed that interaction of the waves with Earth's structure is weak in terms of scattering on the way from the source to the model domain beneath the receiver. Thus the signal that enters the crust at
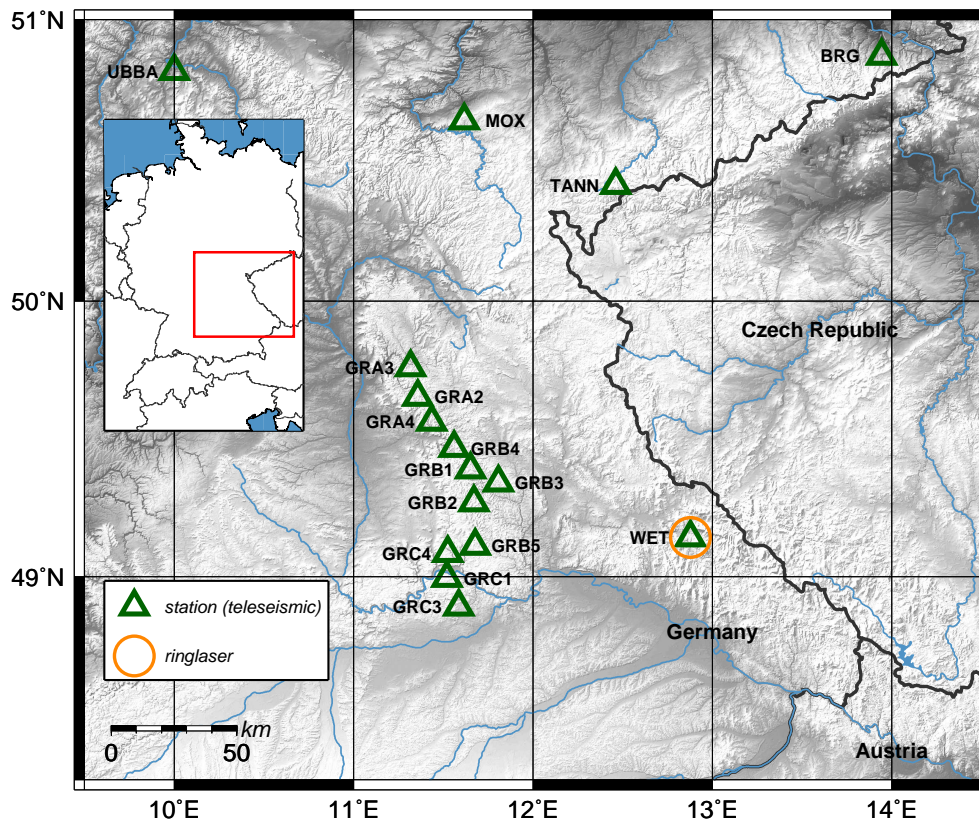
Figure 8.1: Study area in the teleseismic data application. The map shows the south-eastern part of Germany. Stations used in the comparison of teleseismic events to simulations of the teleseismic P-coda are shown in green triangles. Orange circle indicates the ringlaser instrument in Wettzell, the device used to record the rotational motions around the vertical axis. Grey shading indicates topography.

the receiver site is close to the source time function of the earthquake and is not yet influenced strongly by scattering. In the selected epicentral distances the first arriving phases are P and PcP, which have similar traveltimes (617–648 s) and also show a similar incidence angle at the receiver of 14° to 18°. The traveltimes and incident angles for P- and PcP-waves are calculated using the IASPEI91 model introduced by Kennett and Engdahl (1991). An overview over the used earthquakes is given in table 8.1.

The earthquakes are recorded at multiple stations of the Gräfenberg array, the Saxonian Seismic Network (SX) and of the German Regional Seismic Network (GRSN). The station WET is of particular interest as, additionally to a classical three-component seismometer, it houses the ringlaser device, that records the rotational ground motions around the vertical axis. An overview of the used stations is given in table 8.2, the station distribution is shown in figure 8.1.

Figure 8.2 shows the seismic records of the four deep teleseismic events (table 8.1) recorded at the station Wettzell. The three components of translational motion in

event id	region	M_w	Δ [°]	d [km]	origin time UTC	$t_{PcP} - t_P$ [s]
event A	E-Russia,NE-China	6.3	73.3	549	2013-04-05-13:00:01	12
event B	Sea of Okhotsk	8.3	70.8	605	2013-05-24-05:44:48	16
event C	Sea of Okhotsk	6.7	72.7	629	2013-05-24-14:56:31	13
event D	Sea of Okhotsk	6.7	72.2	573	2013-10-01-03:38:22	14

Table 8.1: Deep teleseismic events used in this study, with M_w being moment magnitude, Δ the epicentral distance from station WET. $t_{PcP} - t_P$ is the arrival time of the PcP wave after the P-wave onset time. d indicates hypocenter depth.

network	station	lon [°]	lat [°]	equipment
GR	GRA3	11.32	49.76	STS-2
GR	GRA2	11.36	49.66	STS-2
GR	GRA4	11.44	49.57	STS-2
GR	GRB4	11.56	49.47	STS-2
GR	GRB2	11.67	49.27	STS-2
GR	WET	12.88	49.14	STS-2
GR	GRB5	11.67	49.11	STS-2
GR	GRC4	11.53	49.09	STS-2
GR	GRC3	11.59	49.89	STS-2
GR	BRG	13.94	50.87	STS-2
GR	UBBA	10.00	50.82	STS-2
GR	GRC1	11.52	50.00	STS-2
GR	GRB1	11.65	49.39	STS-2
GR	GRB3	11.80	49.34	STS-2
GR	MOX	11.62	50.65	STS-2
SX	TANN	12.46	50.42	STS-2

Table 8.2: Stations used in the teleseismic application. *lon* indicates longitude and *lat* indicates latitude.

vertical (TZ), north-south (TN) and east-west (TE) direction are shown, as well as the rotation rate around the vertical axis. A clear increase in rotational motion energy can be observed in the coda after the P- and PcP-arrival.

8.2 Ringlaser performance

Before modelling its data the ringlaser is investigated in terms of its performance, that is its frequency response. The optical measurement principle of the ringlaser results in a flat response over the entire frequency range. The acquired data, however is the product of the instrument and the data acquisition system. To investigate the
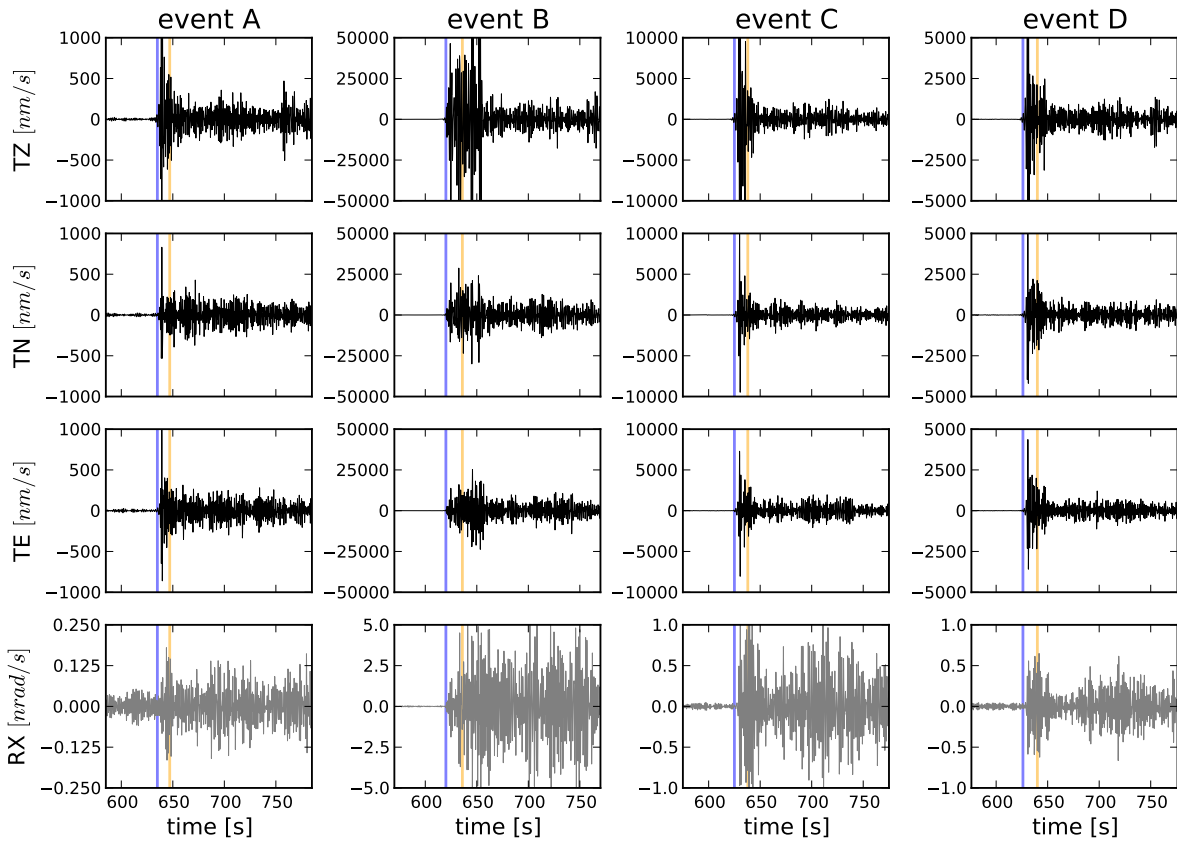
Figure 8.2: Records of the deep teleseismic events. Top three rows show the translational velocities in the vertical (TZ), north-south (TN) and east-west (TE) direction recorded at the station Wettzell. Bottom row shows the rotation rate measured around the vertical axis (RZ). Rows indicate the four deep events. Data is filtered in a narrow bandpass around 1 Hz. Vertical blue lines indicates the theoretical arrival of the P-phase, the theoretical onset of the PcP-phase is indicated by the vertical orange line.

frequency response of the entire rotational motion recording system, the power spectral density (PSD) of the rotation data is compared to the PSDs of the three translational components. The PSD functions are calculated using data from the S-wave coda of a regional event. This comparison is shown in figure 8.3. To compare the PSDs of translational and rotational motions, the amplitudes of the PSDs have to be scaled. PSDs of the ground velocity are multiplied by the angular frequency to obtain the acceleration spectrum and rotation rate data are scaled with two times the local S-wave phase velocity prior the computation of the PSD. For plane horizontally polarized shear waves the accelerations and scaled vertical rotation rates should have similar amplitudes (equations 4.30 and 4.32). A relatively stable PSD can be observed for the translational components over the entire frequency range (see figure 8.3), representing the source spectrum of the event. Up to around 1 Hz the scaled translational amplitudes and the rotation rates agree well. On the other hand a clear drop can be noticed in

the PSD of the rotational components for frequencies above 1 Hz. This sudden drop in the PSD is explained by limitations of the data acquisition system of the ringlaser data. For that reason, the frequency band around 1 Hz is used for the comparison of rotational and translational motion envelopes from the station WET.
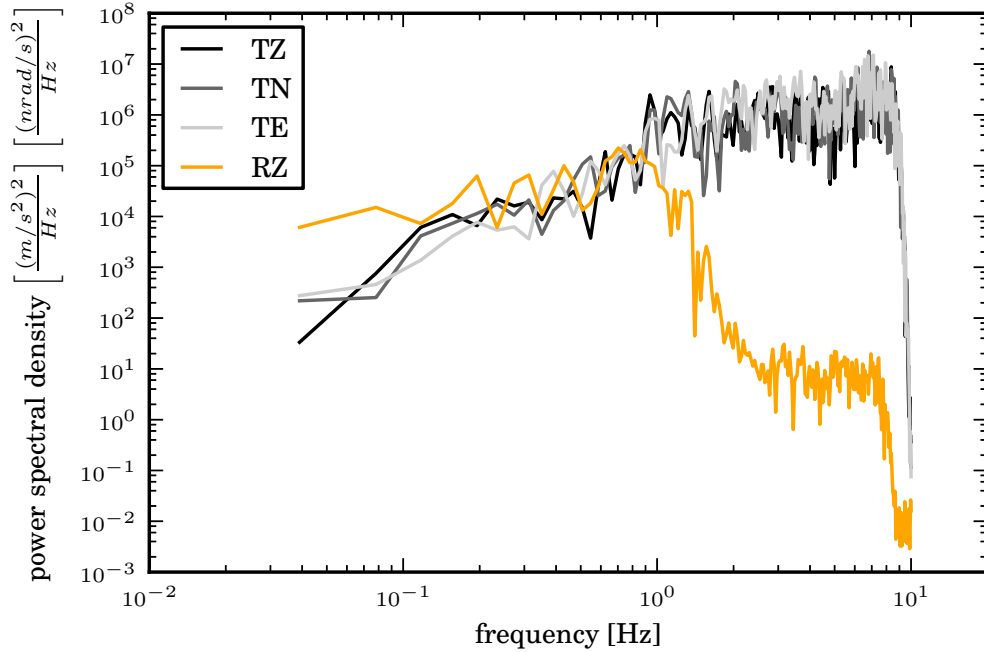

Figure 8.3: Power spectral density of the three translational motion components and the rotation around the vertical axis (RZ) for the S-wave coda of a regional event. Translational components are shown in gray colors, the rotational component is shown in orange. A clear drop in the PSD is noticed for the rotational component at around 1 Hz, whereas the translational component PSDs are stable over the entire frequency range. TZ indicates motion in the vertical direction, TN in north-south direction and TE indicates motion in the east-west axis.

8.3 Modeling and comparison of the teleseismic P- and PcP-coda

The simulations of the teleseismic events are based on the modeling approach described in section 4.7.2. To synthesize the seismogram envelopes a model as the one introduced in chapter 7 is used, consisting of a heterogeneous layer with a thickness of 30 km representing the crustal part of the model domain over a half space representing the transparent mantle. The scattering and attenuation parameters in the crust are chosen according to the results obtained in chapter 7. Fluctuation strength is 2.9 per cent, correlation length a is 0.27 km and the intrinsic quality factor for S-waves Q_S^i is 667

(Q_i^P=1500). This choice of ϵ and a results in transport mean free path length of $\sim$420 km. The source is placed below the crust inside the transparent mantle. The energy is radiated in an unidirectional direction upwards with an angle θ_2, which results in the predicted incidence angle at the surface θ_1 (equation 4.36). The arrival of P- and PcP-energy is simulated in two steps. First the arrival of P-energy with the corresponding theoretical incidence angle is simulated. In a second step the arrival of PcP is simulated using the incidence angle for PcP-energy and taking into account the reflection coefficient for reflected P-energy at the core-mantle boundary. In the algorithm a source is modeled, in which all energy is emitted at the same time. The resulting envelopes for P- and PcP-arrivals are then convolved with the mean square envelope of the source time function of the earthquake to account for the finite source duration. Source time functions are extracted from the SCARDEC method described in Vallée et al. (2011) and Vallée (2013). Envelopes of PcP-energy are shifted according to the difference in PcP- and P-traveltime (see table 8.1). The resulting traces are added to obtain the envelope representing P- and PcP-energy.

A comparison between the simulated arrivals and the recordings for the three translational motions and the rotation rate around the vertical axis are shown in figure 8.4. The figure shows the envelopes recorded at all the stations (figure 8.1, table 8.1) as gray lines and their average in black. As the distance is small between the stations in comparison to the epicentral distance the records are very similar allowing for averaging. Station WET is highlighted in orange as it corresponds to the envelopes of the rotation rate. Modeled translational (top three rows) and vertical rotational (bottom row) envelopes are plotted in red. To compare simulations and data, the envelopes are scaled to the average coda amplitude in a late time window. Note that only the average coda amplitude in a late time window of the total translational envelope is used to scale all three translational envelopes as well as the vertical rotational envelopes with a single scaling factor. This is possible due to the assumption of plane wave propagation and the corresponding scaling described in equations 4.30 and 4.32. The first thing to note in figure 8.4 is the complexity in the data. The different durations of the direct P-pulse is well accounted for by convolution with the source time functions plotted in green in figure 8.4.The coda decay of the translational motion envelopes is fairly well modeled for all events. The rotation rate envelopes show much larger fluctuations as thetranslational reference envelopes for two reasons. First, no averaging over different stations could be performed as there is only one instrument of this type available. Second the noise level of the ringlaser is high compared to the noise level of classical seismometers. So the main characteristics of the rotation data are the absence of a direct pulse at the arrival time of the P-wave and a decay similar to the translational envelopes. As shown in the bottom row of figure 8.4 these main characteristics of the data are modeled well by the synthetic envelopes. Additionally note, that the absolute amplitude levels of the simulated translations and rotations agree with the observations and there no independent parameter is required for scaling the rotational amplitudes.
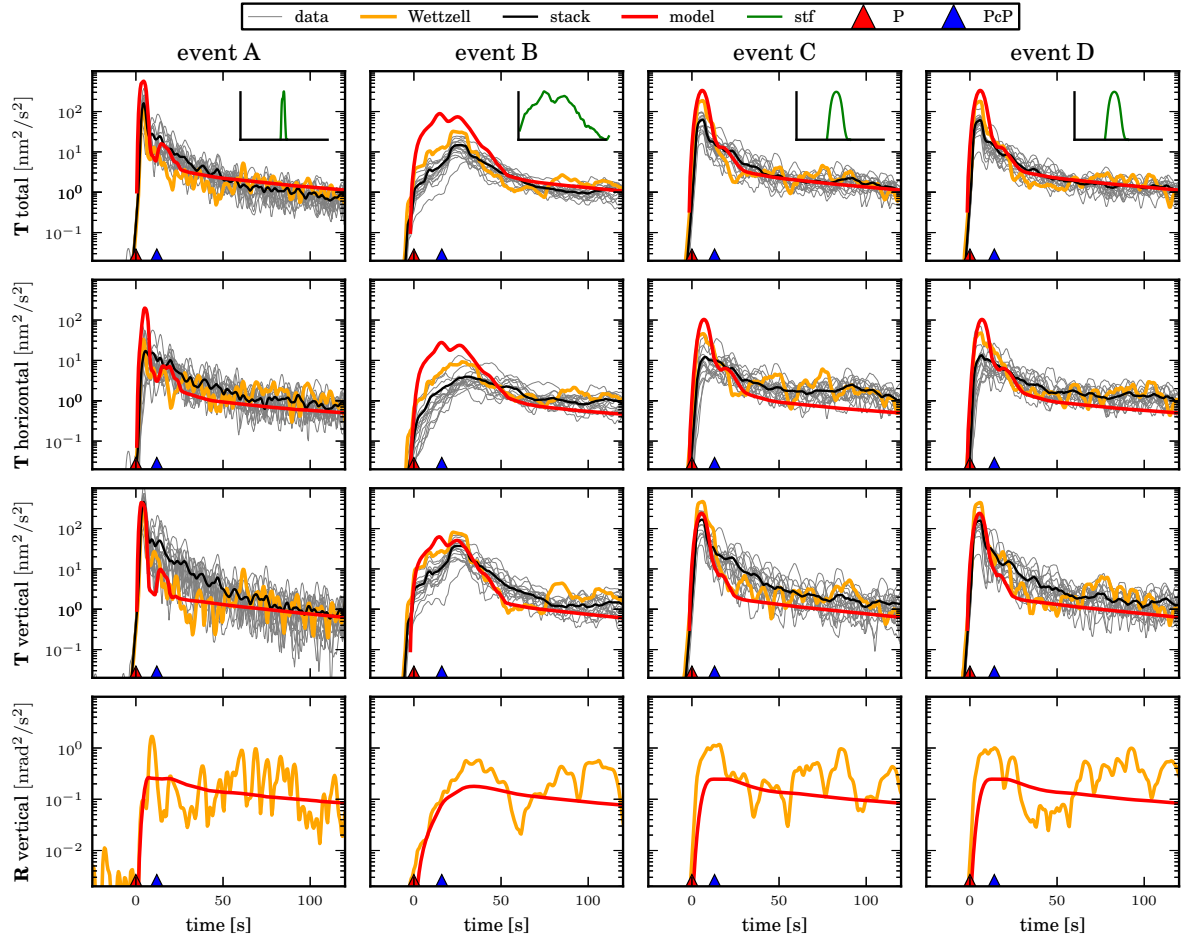
Figure 8.4: Comparison of simulations and data for teleseismic arrivals. Results of the simulations are shown in red, black lines represent a stack of all available stations (see figure 8.1). The gray lines in the background represent traces for each single station. The station WET is highlighted in orange color. Top row shows total translations, the second row gives the horizontal translations and the vertical translations are shown in the third row. Columns represent the different earthquakes given in table 8.1. Rotational motions around the vertical axis are shown in the bottom row. As only for station WET rotational motion records are available, only one recorded trace can be compared to the simulations. Source time functions used for the convolution with the simulated traces are indicated in green in the same time scale as the data. The time scale is chosen such that P-wave arrival is a time zero. Units are given in nm^2/s^2 or $nrad^2/s^2$ (intensity) and scaled to a coda average. Theoretical arrivals of P- and PcP-energy are marked with red and blue triangles, respectively. In the investigated time window only the arrival of P- and PcP-energy is theoretically expected.

9 Discussion

In the local data investigation in chapter 6 crustal scattering and attenuation parameters are estimated using elastic and acoustic RTT. As the acoustic approach only simulates S-wave propagation, the focus is on the analysis of the transport mean free path for S-waves l_S^* and on the intrinsic attenuation of S-waves, expressed through the absorption path length of S-waves l_S^i. Both methods yield very similar results for the scattering and attenuation parameters, with smaller errors estimated in the elastic approach. Both, the elastic and the acoustic theory, yield a similar frequency dependence of the parameters and are able to describe the first onset of the direct S-wave as well as the following S-wave coda with a high precision. The estimated parameters in the different frequency band are comparable to the results from other studies, but are estimated to be situated in the stronger scattering and attenuation regime. The transport mean free path of S-waves l_S^* is comparable to a study by Przybilla et al. (2009), who used a local data set in Norway to estimate values of ~ 80–170 km for frequencies in the range of 2–10 Hz. A local study by Fielitz and Wegler (2015) estimates absorption path lengths for S-waves between 36–43 km for frequencies between 6–24 Hz at the Continental Deep Drilling site in Germany. Investigations of regional data sets in general, for example Sens-Schönfelder and Wegler (2006), Sens-Schönfelder et al. (2009) or chapter 7 estimate higher values for the transport mean free path and the intrinsic quality factor for S-waves, which indicates weaker attenuation and weaker scattering properties. This can be explained by the different penetration depths of the seismic waves for different investigated distance ranges. In the case of regional data sets the direct waves, as well as the scattered energy, sense much deeper regions of the crust in comparison to waves recorded in a local distance range (Calvet and Margerin, 2013). Scattering and attenuation parameters are depth dependent and therefore can explain the slightly higher values estimated in the local data set in comparison to the regional data set (chapter 7), even if the two investigated areas in this study are in close proximity. From the elastic simulations the conclusion can be drawn that it is not possible to estimate the scattering parameters correlation length a and the velocity fluctuation strength ϵ separately, but only the transport mean free path of l^*, which results from a combination the two parameters a and ϵ. This fact can be used to narrow down the parameter space that has to be investigated in inversion or grid search processes. Instead of considering two free scattering parameters (a and ϵ), only the parameter ϵ is sampled in the parameter finding process. Due to the fact that forward scattering is necessary to explain the data ($ak \gg 1$), the parameter a can be

fixed in the individual frequency bands, so that $ak \gg 1$. Therefore, only considering ϵ as a free parameter will lead to different values for the transport mean free path and will suffice to give a correct description of the scattering parameters of the medium.

The results from the local data set using acoustic and elastic RTT yield fairly similar parameters for the S-wave scattering and attenuation parameters. This indicates that for a simple setup with a half space, isotropic scattering and only modeling S-wave propagation, the acoustic approach may suffice to obtain basic parameters about the scattering properties of the medium. This is especially attractive, as analytic solutions to this approach exist, which can be computed very efficiently and deliver results with only minor computational costs. For more complex models however, numerical solutions to the elastic RTEs have to be utilized. This methods includes the possibility of modeling the propagation of P- and S-energy, as well as conversions between those two modes. The modeling of the two modes of energy allows investigations of the ratio of Q_i^P/Q_i^S. Furthermore the more realistic assumption of forward scattering can be implemented in the modeling.

In the regional application in chapter 7 an inversion of regional three-component seismogram envelopes at different epicentral distances is used to infer parameters of the crustal heterogeneities in south-east Germany beneath the Gräfenberg array. The resulting values 2.5 % $< \epsilon <$ 3.5 %, 0.1 $km < a <$ 0.4 km and 580 $< Q_i^S <$ 750 for the fluctuation strength, the correlation length of the random medium with an exponential ACF and the S-wave quality factor are in fair agreement with comparable studies in Europe. Sens-Schönfelder and Wegler (2006) revealed an intrinsic quality factor Q_i^S of 769 in Germany at 3 Hz using events at regional distances. Another study by Sens-Schönfelder et al. (2009) in the Pyrenees (France) describes the attenuation of S-waves with a value Q_i^S of 625. These results in France were confirmed by Calvet and Margerin (2013), who found an intrinsic quality factor for S-waves Q_i^S of $\sim$ 800 for a frequency of 3 Hz. In the regional application the correlation length of the exponential type fluctuations of $a = 0.25$ km together with a fluctuation strength $\epsilon = 2.9$ % leads to a transport mean free path of S-waves of $l_S^* = 420$ km at 6 Hz. This value is supported by Calvet and Margerin (2013) who found $l_S^* \sim 400$ km for their preferred model at 6 Hz. Sens-Schönfelder et al. (2009) obtained a transport mean free path of 761 km at 3 Hz which is also comparable to the results of this study. Rothert (2000) inferred similar correlation lengths and fluctuations of velocity in the crust from the analysis of teleseismic events at the Gräfenberg array. The agreement with results of Calvet and Margerin (2013) is remarkable as these authors inverted the lapse time dependence of the coda attenuation Q^c with a model of multiple anisotropic acoustic scattering in an infinite half space. In contrast, the model used in this study features elastic scattering in a layer over half space structure. This correspondence confirms the importance of S-wave scattering in the crust and supports the decision to ignore scattering in the mantle in section 8. In addition, the more realistic modeling approach in this study allows to simulate full seismogram envelopes, including P-wave energy and the early coda. Comparison of the envelopes in figure 7.8, however, indicates that detailed modeling of the early coda requires the incorporation of the source radiation pattern even

in the present case where an averaging over different events is performed.

In the teleseismic analysis in chapter 8 the modeling domain is separated into a scattering crust and a transparent mantle. This setup allows to model the excitation of the domain by sources outside the scattering medium, in a simplified way focusing on scattering in the crust at the receiver side. This possibility is used to model the envelopes of the teleseismic P- and PcP-coda including rotational motions around the vertical axis. As the same study area is investigated as in the regional application (chapter 7), the parameters estimated from the inversion of regional seismogram envelopes are used to model the first 100 s after the arrival of the direct P-wave. This 100 s time window contains the direct P-phase, the direct PcP-phase and the coda of the P/PcP-phase. The observations are restricted to this time interval to exclude the depth phase pP, which arrives $\sim$ 120 s after the direct P-wave for the chosen distance and depth range. The reason for excluding pP is its dependence on the structure on the source side of the path. As the pP-phase penetrates the crust on the source side twice, its shape is not only influenced by the source time function of the event, but the shape of the coda is also strongly dependent on the crustal heterogeneities above the source. Modeling of the source side would therefore require a detailed knowledge about the crustal parameters in the source region. A further argument of excluding the pP-phase, is the dependence of the P/pP amplitude ratios on the radiation pattern of the source.

The modeling results show a reasonable agreement with the observed seismogram envelopes for translational motions as well as for rotation rate around the vertical axis (figure 8.4). The focus lies on the comparison of the peak of the direct arrival as well as on the decay of the coda of the translational and rotational motion envelopes. An additional observable is the relative amplitude of the translational and rotational data. The different width of the direct P-pulse is well accounted for by the convolution with the source time function of the respective events. Also the coda decay of the translational motion envelopes is fairly well modeled for the investigated events. Especially in comparison to the decay of the regional envelopes that extends over almost 3 orders of magnitude during 80 s, the slow decay of the teleseismic coda is matched well by the model. Absolute amplitudes of the direct pulse show different misfit for the horizontal and vertical motion. In our case the horizontal motions are overestimated. This is attributed to the effect of the shallow velocity structure that is not properly accounted for in our model and causes steeper incidence in reality. The vertical rotational motion envelopes show larger fluctuations than the translational envelopes. This is related to the lack of averaging, as only one rotational sensor can be used, and to a higher noise level in the rotational motion data. The main characteristics of the data is again well reproduced by the model. In contrast to the translational motion envelopes, the rotational data do not show a direct pulse due to the insensitivity of the rotation data to compressional energy. The decay is the same for rotational and translational data and is well reproduced by the model. Also the absolute amplitude of the rotational coda envelope is well predicted by the model. This observation confirms findings of earlier studies, that the local structure and heterogeneity at the receiver side is sufficient to generate the long lasting coda of teleseismic arrivals. The presented model consistently
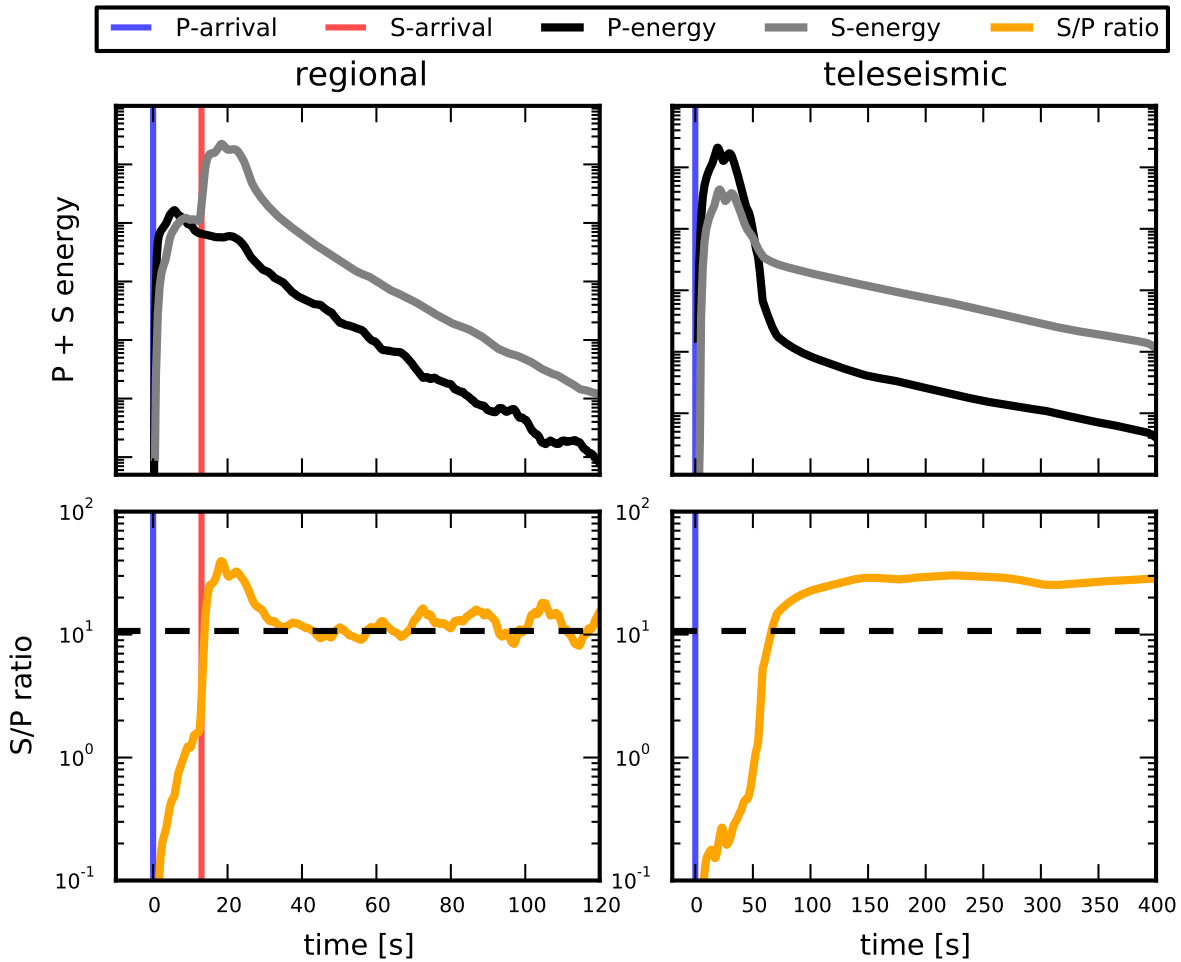
Figure 9.1: Temporal evolution of the equipartition ratio for S- and P-energy. Top row shows P- and S-energy for a regional simulation at en epicentral distance of 100 km (left, compare figure 7.8) and for the teleseismic case (right, compare figure 8.4). Bottom row gives the ratio of S- and P-energy. Dashed black line represents the theoretical equipartition value of ~ 10.7 for our model.

describes the coda of regional events at variable distances and the coda of teleseismic P- and PcP-wave arrivals including data of rotational motions around the vertical axis. Especially the fit of the rotational motion envelopes, that is qualitatively modeled here for the first time, provides confidence in the correct modeling of the main mechanism that generates the coda of local, regional and teleseismic events.

Assuming that the preferred model provides a realistic description of the scattering processes allows to investigate properties of the scattered wave field beyond the observables that can directly be compared to measurements using MC-RTT simulations. The energy partitioning between P- and S-energy in the wave field is such an observable that is difficult to measure (Shapiro et al., 2000; Hennino et al., 2001; Margerin et al., 2009) in the field but can easily be calculated from simulations (Margerin et al., 2000). According to Ryzhik et al. (1996) the theoretical value for the S- to P-energy ratio for
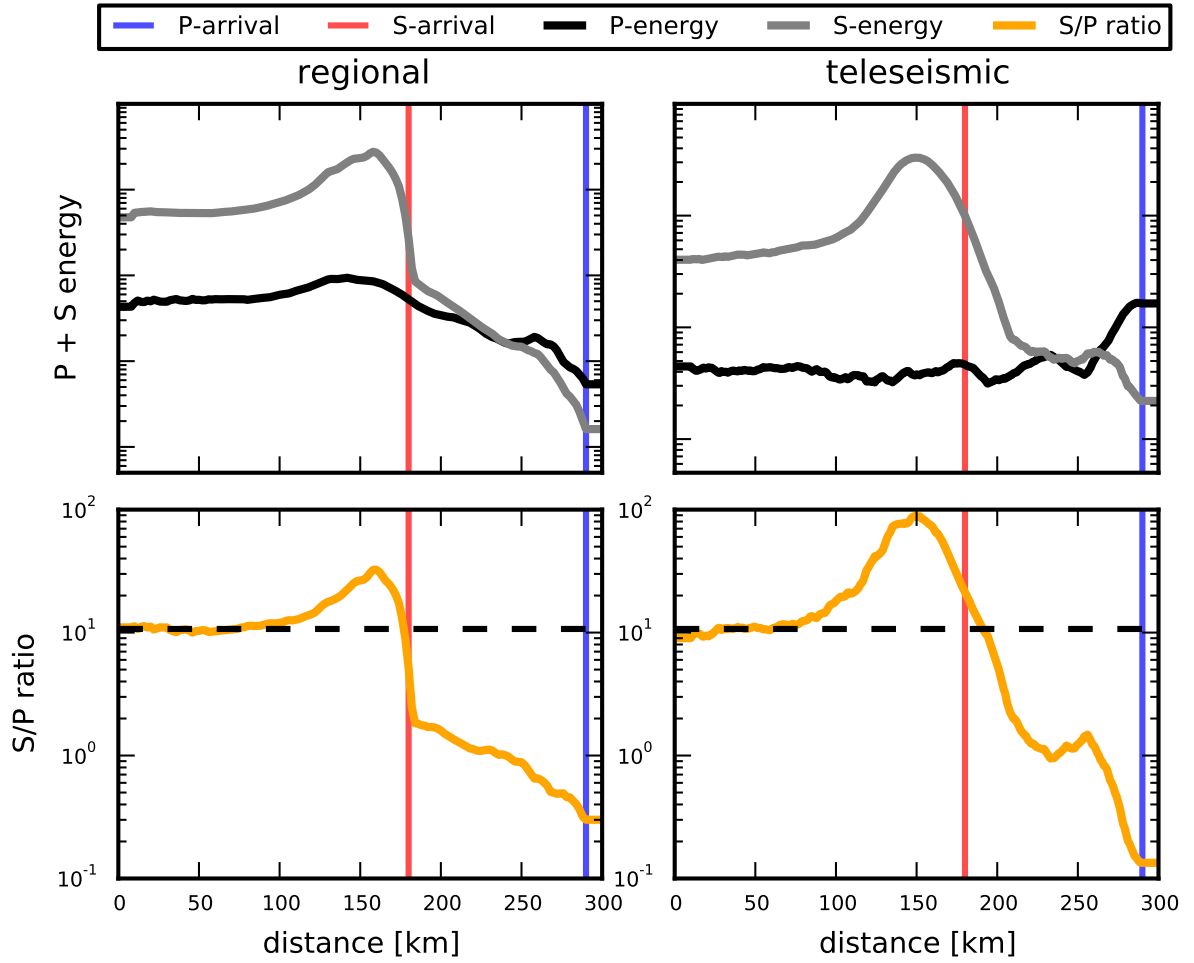
Figure 9.2: Spatial evolution of the equipartition ratio for S- and P-energy. Top row shows a temporal, space dependent snapshot of P- and S-energy of an regional (left) and teleseismic event (right) for 50 s lapse time. Traces are according to the snapshots shown in figure 4.5 and 4.7. Bottom row gives the ratio of S- and P-energy. Dashed black line represents the theoretical equipartition value of ~ 10.7.

long lapse times tends to stabilize in infinite space at

$$\frac{E_S}{E_P} = \frac{2v_p^3}{v_s^3}, \tag{9.1}$$

with E_S and E_P being S- and P-energy, v_p and v_S are P- and S-wave speeds respectively. This is the value that is expected to be found in the simulations performed here, as the interference effect at the surface, that leads to a locally different value at the surface (Margerin et al., 2009), is not included in our model. The velocity structure in our model results, applying equation 9.1, in an equipartition ratio of ~ 10.7. In figure 9.1 the temporal evolution of energy partitioning is shown for the regional (chapter 7) and

teleseismic (chapter 8) simulations.

For the regional case a fast stabilization of the partition ratio at the expected value of 10.7 can be observed only a short time after the passage of the direct S-wave. This behavior is similar to simulations shown by Margerin et al. (2000). In contrast the simulations for the excitation by teleseismic waves converge to a S- to P-energy ratio of about 30, this is an indication that the equipartition regime is not reached even after 400 s. A ratio of 30 for E_S/E_P indicates a three fold excess of S-energy compared to equipartition, which is surprising as the teleseismic wave field, modeled in this study, is excited by a purely compressional P-wave.

The explanation for this observation is the excitation by the plane wave impinging on the crust. To illustrate this the spatial distribution of deformation energy at 50 s lapse time is shown in figure 9.2. In the case of the regional simulation (figure 4.5, 50 s) we observe the expected behavior with a S- to P-energy ratio below the equipartition value between the P- and S-wave fronts and above equipartition directly behind the S-wave train. Around the source location and some distance behind the S-wave front the ratio converges towards equipartition. The illustration of the spatial energy distribution for the teleseismic excitation is related to figure 4.6. The teleseismic plane wave excitation corresponds to an areal distribution of upward directed P-sources. Figure 9.2 (right) shows the energy distribution for one of these directed sources at 50 s lapse time (compare figusre 4.7, 50 s). Even though this source emits pure P-energy, the figure shows that a S-wave is generated by scattering close to the source that propagates as a guided wave as seen in figure 4.6. The energy partitioning is similar to the isotropic source inside the crust in the regional simulations and converges towards the equipartition ratio of 10.7 behind the S-wave. The integral effect of the areal distribution of such individual sources, that simulate the plane wave excitation, causes a superposition of sources at different distances. As seen in figure 4.7 the strongest contribution in this source integral comes from sources in the distance corresponding to the propagation distance of the guided S-waves. These sources introduce an excess in S-wave energy which leads to an increased S- to P-energy ratio above the theoretically expected equipartition value.

10 Conclusions

In this work a method to model multi-component seismogram envelopes of translational and rotational motions in a deterministic, macroscopic background structure with spatially dependent density and velocity fluctuations is introduced. This approach is based on Monte Carlo solutions to the RTEs assuming multiple, anisotropic scattering events described by the Born approximation. This method allows the modeling of events in the local, regional and teleseismic distance range. This methodology is introduced to also model the envelopes of rotational motion sensor measurements.

The results of the MC-RTT simulations are verified by comparisons with 3D full wave field FD simulations. Six-component seismogram envelopes from the two different approaches are computed and show a good agreement for the translational motions as well as for the rotational motion energy. It is concluded, that the elastic radiative transfer approach is a suitable method to model translational and rotational motion seismogram envelopes of the high frequency seismic wave field from the initial onset of the direct P-wave to the late parts of the S-wave coda in continuous elastic random media.

Results of the local investigation of the Vogtland region using a local data set show slightly stronger scattering and higher attenuation values in comparison to similar study areas, in particular to the Gräfenberg array area, which is in close proximity. These higher values can be explained with the depth dependence of scattering and attenuation. Seismic waves recorded on a local or a regional scale sense different depths of the crustal structure due to their varying penetration depth and therefore can result in different scattering and attenuation values. Results from the acoustic and elastic radiative transfer simulations show nearly identical values for the S-wave scattering and attenuation. For the investigation of S-wave propagation and scattering, the simple isotropic acoustic approach may suffice. However, for the modeling of coupled P- and S-energy propagation, conversions between those modes, multiple anisotropic scattering and complex background models, the numerical elastic radiative transfer theory approach is essential.

Crustal scattering and attenuation parameters from the Gräfenberg array area in southeast Germany were obtained using an inversion of regional swarm earthquake envelopes. Results agree with the outcomes from comparable studies covering the European region. Scattering in the mantle is not required for the modeling of the seismogram envelopes, but weak scattering in the lithospheric mantle cannot be ruled out.

10 Conclusions

In the teleseismic data example P- and PcP-phase arrivals are simulated, using the set of crustal scattering and attenuation parameters obtained from the regional inversion. The simulation results are compared to translational and rotational motion records from deep teleseismic events and show a reasonable agreement to the observations. The observed and simulated rotations around the vertical axis indicate the scattering from P- to SH-energy in the vicinity of the receiver and therefore strengthens the argument of multiple scattering at 3D-heterogeneities. The scaling of the rotations with respect to the translational motions described in equations 4.30 and 4.32 shows, that S-waves can locally be treated as plane waves and that the level of observed rotational energy in the teleseismic P-coda is a natural consequence of the scattering processes that generate the coda of the conventional translational motions.

Observations of seismic energy equipartition in the regional coda show a rapid stabilization around the theoretically expected value, while in the teleseismic P/PcP-coda the energy partitioning strongly favors S-energy due to the spatially extended source mechanism of the incident plane wave. This conclusion is drawn from simulations and has to be further investigated using real data from teleseismic events for example applying seismic array techniques.

To improve the estimation of scattering and intrinsic attenuation and to further determine the influence of crust and mantle, simultaneous investigations of data from different epicentral distance ranges are proposed. The observation and modeling of the rotational motion components provides additional and independent information about scattering and propagation of the high frequency seismic wave field in the Earth's structure and is a valuable additional observable to the classical translational components. However only a few rotational motion sensors are currently available, that can reliably and with high quality record the rotational motions excited by seismic waves. This underlines the necessity of developing high-quality instruments able to continuously observe and record the rotational motion components of the seismic wave field.

List of References

Abubakirov, I. R. and Gusev, A. A. (1990). Estimation of scattering properties of lithosphere of Kamchatka based on Monte-Carlo simulation of record envelope of a near earthquake. *Physics of the Earth and Planetary Interiors*, 64:52–67. Cited on pages 5, 7, 9, and 10.

Aki, K. (1969). Analysis of the Seismic Coda of Local Earthquakes as Scattered Waves. *Journal of Geophysical Research*, 74(2):615–631. Cited on page 5.

Aki, K. (1980). Atenuation of shear-waves in the lithosphere for frequencies from 0.05 to 25 Hz. *Physics of The Earth and Planetary Interiors*, 21:50–60. Cited on pages 64 and 83.

Aki, K. (1981). Scattering and attenuation of high-frequency body waves (1-25 Hz) in the lithosphere. *Physics of the Earth and Planetary Interiors*, 26:241–243. Cited on page 6.

Aki, K. and Chouet, B. (1975). Origin of coda waves: source, attenuation, and scattering effects. *Journal of Geophysical Research*, 80(23):3322–3342. Cited on pages 5 and 7.

Aki, K. and Richards, P. G. (2002). *Quantitative Seismology*. University Science Books. Cited on page 12.

Apresyan, L. and Kravtsov, Y. (1996). *Radiation Transfer: Statistical and Wave Aspects*. Gordon and Breach Publishers, Amsterdam. Cited on pages 29 and 30.

Belfi, J., Beverini, N., Carelli, G., Virgilio, A., Maccioni, E., Saccorotti, G., Stefani, F., and Velikoseltsev, A. (2012). Horizontal rotation signals detected by "G-Pisa" ring laser for the $M_w = 9.0$, March 2011, Japan earthquake. *Journal of Seismology*, (March 2011). Cited on page 17.

Bernauer, F., Wassermann, J., and Igel, H. (2012). Rotational sensors - a comparison of different sensor types. *Journal of Seismology*, 16(4):595–602. Cited on pages 16, 17, 19, and 21.

Birch, F. (1961). The Velocity of Compressional Waves in Rocks to 10 Kilobars, Part 2. *Journal of Geophysical Research*, 66(7):2199–2224. Cited on page 32.

List of References

Bohlen, T. (2002). Parallel 3-D viscoelastic finite difference seismic modelling. *Computers & Geosciences*, 28(8):887–899. Cited on pages 49 and 51.

Bohlen, T., De Nil, D., Köhn, D., and Jetschny, S. (2010). Parallel 3-D viscoelastic / acoustic finite difference seismic modeling (Users Guide). Cited on pages 49 and 50.

Bouchon, M. and Aki, K. (1982). Strain, tilt and rotation associated with strong motion in the vicinity of earthquake faults. *Bulletin of the Seismological Society of America*, 72:1717–1738. Cited on page 12.

Brokešová, J. and Málek, J. (2013). Rotaphone, a Self-Calibrated Six-Degree-of-Freedom Seismic Sensor and Its Strong-Motion Records. *Seismological Research Letters*, 84:737–744. Cited on page 17.

Brokešová, J., Málek, J., and Kolínský, P. (2012). Rotaphone, a mechanical seismic sensor system for field rotation rate measurements and its in situ calibration. *Journal of Seismology*. Cited on pages 17 and 18.

Bullen, K. and Bolt, B. (1985). *An Introduction to the Theory of Seismology*. University Press, Cambridge. Cited on page 1.

Calvet, M. and Margerin, L. (2013). Lapse-Time Dependence of Coda Q : Anisotropic Multiple-Scattering Models and Application to the Pyrenees. *Bulletin of the Seismological Society of America*, 103(3):1993–2010. Cited on pages 5, 10, 84, 95, and 96.

Chandrasekhar, S. (1960). *Radiative Transfer*. Dover Publications, Inc. Cited on page 25.

Dainty, A. (1981). A scattering model to explain seismic Q observations in the lithosphere between 1 and 30 Hz. *Geophysical Research Letters*, 8(1):1126–1128. Cited on pages 6 and 7.

Dainty, A., Toksöz, M., Anderson, K., Nakamura, Y., and Latham, G. (1974). Seismic scattering and shallow structure of the Moon in Oceanus Procellarum. *The Moon*, 9(1974):11–29. Cited on page 7.

Dunn, W., Mahdi, H., and Al-Shukri, H. (2009). Design of a Relatively Inexpensive Ring Laser Seismic Detector. *Bulletin of the Seismological Society of America*, 99:1437–1442. Cited on page 17.

Dziewonski, A. M. and Anderson, D. L. (1981). Preliminary reference Earth model *. *Physics of the Earth and Planetary Interiors*, 25:297–356. Cited on pages 1 and 82.

Eentec (2015a). http://www.eentec.com/pdf/ELEKTROCHEMICA-1.pdf. *Webpage, last visited 11.01.2015*. Cited on page 15.

Eentec (2015b). R2 Instruction Manual. *Manual*. Cited on pages 16, 21, and 22.

Emoto, K., Sato, H., and Nishimura, J. (2010). Synthesis of vector wave envelopes on the free surface of a random medium for the vertical incidence of a plane wavelet based on the markov approximation. *Journal of geophysical research*, 115(B08306):1–15. Cited on page 28.

Exxon (2015). www.sakhalin-1.com. *Webpage, last visited 16.01.2015.* Cited on page 1.

Fehler, M., Hoshiba, M., Sato, H., and Obara, K. (1992). Separation of scattering and intrinsic attenuation for the Kanto-Tokai region, Japan, using measurements of S-wave energy versus hypocentral distance. *Geophysical Journal International*, 108(3):787–800. Cited on pages 9 and 10.

Fielitz, D. and Wegler, U. (2015). Intrinsic and scattering attenuation as dervided from fluid induced microseismicity at the german continental deep drilling site. *Geophysical Journal International*, 201(3):1346–1361. Cited on page 95.

Fischer, T., Horálek, J., Hrubcová, P., Vavryčuk, V., Bräuer, K., and Kämpf, H. (2013). Intra-continental earthquake swarms in West-Bohemia and Vogtland: A review. *Tectonophysics*, 611:1–27. Cited on pages 59, 60, and 84.

Fowler, C. (2005). *The Solid Earth.* University Press, Cambridge. Cited on pages 1 and 2.

Franke, W. (1989). Variscan plate tectonics in Central Europe – current ideas and open questions. *Tectonophysics*, 169(4):221–228. Cited on page 80.

Gaebler, P. J., Sens Schönfelder, C., and Korn, M. (2015a). The influence of crustal scattering on translational and rotational motions in regional and teleseismic coda waves. *Geophysical Journal International*, 201(1):355–371. Cited on page 3.

Gaebler, P. J., Eulenfeld, T., and U., W. (2015b). Seismic scattering and absorption parametersin the w-bohemia/vogtland region from elastic and acoustic radiative transfer theory. *Geophysical Journal International*, 203(1):1471–1481. Cited on page 3.

Geissler, W. H., Kämpf, H., Kind, R., Bräuer, K., Klinge, K., Plenefisch, T., Horálek, J., Zedník, J., and Nehybka, V. (2005). Seismic structure and location of a CO 2 source in the upper mantle of the western Eger (Ohře) Rift, central Europe. *Tectonics*, 24(5). Cited on page 59.

Goldberg, D. (1989). *Genetic Algorithms in Search, Optimization, and Machine Learning.* Addison-Wesley. Cited on page 73.

Gomberg, J. and Agnew, D. (1996). The accuracy of seismic estimates of dynamic strains: An evaluation using strainmeter and seismometer data from piñon flat observatory, california. *Bulletin of the Seismological Society of America*, 86:212–220. Cited on page 12.

List of References

Gusev, A. and Abubakirov, I. (1987). Monte-Carlo simulation of record envelope of a near earthquake. *Physics of the Earth and Planetary Interiors*, 49(1-2):30–36. Cited on pages 34 and 35.

Gutenberg, B. (1914). Beobachtungen an Registrierungen von Fernbeben in Göttingen und Folgerungen über die Konstitution des Erdkörpers. *Nachr. Ges. Wiss. Göttingen*, 1:1–52. Cited on page 2.

Hadziioannou, C., Gaebler, P., Schreiber, U., Wassermann, J., and Igel, H. (2012). Examining ambient noise using colocated measurements of rotational and translational motion. *Journal of Seismology*. Cited on pages 12 and 19.

Halley, E. (1692). An Account of the Cause of the Change of the Variation of the Magnetical Needle; With an Hypothesis of the Structure of the Internal Parts of the Earth: As It Was Proposed to the Royal Society in One of Their Late Meetings. *Philosophical Transactions*, 16:563–587. Cited on page 1.

Heinicke, J., Fischer, T., Gaupp, R., Goetze, J., Koch, U., Konietzky, H., and Stanek, K.-P. (2009). Hydrothermal alteration as a trigger mechanism for earthquake swarms: the Vogtland/NW Bohemia region as a case study. *Geophysical Journal International*, 178(1):1–13. Cited on page 60.

Hennino, R., Trégourès, N., Shapiro, N., Margerin, L., Campillo, M., van Tiggelen, B., and Weaver, R. (2001). Observation of Equipartition of Seismic Waves. *Physical Review Letters*, 86(15):3447–3450. Cited on page 98.

Hock, S., Korn, M., Ritter, J. R. R., and Rothert, E. (2004). Mapping random lithospheric heterogeneities in northern and central Europe. *Geophysical Journal International*, 157(1):251–264. Cited on page 10.

Horálek, J., Fischer, T., Boušková, A., and Jedlička, P. (2000). The Western Bohemia/Vogtland region in the light of the WEBNET network. *Studia Geophysica et Geodaetica*, 44:107–125. Cited on page 61.

Hoshiba, M. (1995). Estimation of nonisotropic scattering in western Japan using coda waves eneveloptes: application of a multiple nonisotropic scattering model. *Journal of Geophysical Research*, 100:645–657. Cited on page 7.

Hoshiba, M., Sato, H., and Fehler, M. (1991). Numerical basis of the separation of scattering and intrinsic absorption from full seismogram envelope: a Monte-Carlo simulation of multiple isotropic scattering. *Pap. Meteorol. Geophys*, 42(2):65–91. Cited on pages 7 and 34.

Igel, H., Cochard, A., Wassermann, J., Flaws, A., Schreiber, U., Velikoseltsev, A., and Pham Dinh, N. (2007). Broad-band observations of earthquake-induced rotational ground motions. *Geophysical Journal International*, 168(1):182–196. Cited on pages 12, 13, 14, and 19.

Ishimaru, A. (1978). *Wave Propagation and Scattering in Random Media.* Academic Press, Inc. Cited on page 38.

Jeffreys, H. (1926). The Rigidity of the Earth's Central Core. *Mon. Not. Roy. Astron. Soc. Geophys. Suppl.*, 1:371–383. Cited on page 2.

Kennett, B. and Engdahl, E. (1991). Traveltimes for global earthquake location and phase identification. *Geophysical Journal International*, 105:429–465. Cited on pages 45 and 88.

Klügel, T., Schreiber, U., Schneider, M., Riepl, S., Schlüter, W., Weber, H., and Stedman, G. (2001). Realisierung des Großringlasers G auf der Fundamentalstation Wettzell. Technical report. Cited on page 80.

Korn, M. (1997). Modelling the teleseismic P coda envelope: depth dependent scattering and deterministic structure. *Physics of the earth and planetary interiors*, 9201(1984). Cited on page 5.

Krüger, F. (1994). Sediment structure at GRF from polarization analysis of P waves of nuclear explosions. *Bulletin of the Seismological Society of America*, 84(1):149–170. Cited on page 80.

Kurrle, D., Igel, H., Ferreira, A. M. G., Wassermann, J., and Schreiber, U. (2010). Can we estimate local Love wave dispersion properties from collocated amplitude measurements of translations and rotations? *Geophysical Research Letters*, 37(4):1–5. Cited on page 19.

Lacombe, C., Campillo, M., Paul, A., and Margerin, L. (2003). Separation of intrinsic absorption and scattering attenuation from Lg coda decay in central France using acoustic radiative transfer theory. *Geophysical Journal International*, 154(2):417–425. Cited on page 10.

Lehmann, I. (1936). P'. *Publications du Burea Central Seismologique International*, 14:87–115. Cited on page 2.

Levander, A. (1988). Fourth-order finite-difference p-sv seismograms. *Geophysics*, 53(11):1425–.1436. Cited on page 49.

Levander, A. R. and Holliger, K. (1992). Small-Scale Heterogeneity and Large-Scale Velocity Structure. *Journal of Earth System Science*, 97:8797–8804. Cited on page 10.

Margerin, L., Campillo, M., and van Tiggelen, B. (2000). Monte Carlo simulation of multiple scattering of elastic waves. *Journal of Geophysical Research*, 105:7873–7892. Cited on pages 7, 30, 34, 38, 98, and 100.

Margerin, L., Campillo, M., Van Tiggelen, B. a., and Hennino, R. (2009). Energy partition of seismic coda waves in layered media: theory and application to Pinyon Flats Observatory. *Geophysical Journal International*, 177(2):571–585. Cited on pages 98 and 99.

List of References

McLeod, D. and Stedman, G. (1998). Comparison of standard and ring laser rotational seismograms. *Bulletin of the Seismological Society of America*, 88(6):1495–1503. Cited on page 17.

Milne, J. (1906). Recent Advances in Seismology. *Proceedings of the Royal Society of London*, 77:365–376. Cited on page 1.

Mitchell, M. (1996). *An introduction to genetic algorithms*. MIT Press, Cambridge. Cited on page 73.

Mueller, S. and Panza, G. F. (1986). Evidence of a Deep-Reaching Lithospheric Root Under the Alpine Arc. In WEZEL, F.-C., editor, *The Origin of Arcs*, volume 21 of *Developments in Geotectonics*, pages 93–113. Elsevier. Cited on page 80.

Nolet, G. (1987). *Seismic Tomography – With Applications in Global Seismology and Exploration Geophysics*. Reidel Publishing Company. Cited on page 2.

Oldham, R. (1906). The Constitution of the Interior of the Earth as Revealed by Earthquakes. *Quaterly Journal of the Geological Society*, 62:450–475. Cited on page 2.

Paasschens, J. (1997). Solution of the time-dependent Boltzmann equation. *Physical Review E*, 56(1):1135–1141. Cited on pages 27 and 34.

Pham, N. D., Igel, H., Wassermann, J., Cochard, A., and Schreiber, U. (2009a). The Effects of Tilt on Interferometric Rotation Sensors. *Bulletin of the Seismological Society of America*, 99(2B):1352–1365. Cited on page 13.

Pham, N. D., Igel, H., Wassermann, J., Kaser, M., de la Puente, J., and Schreiber, U. (2009b). Observations and Modeling of Rotational Signals in the P Coda: Constraints on Crustal Scattering. *Bulletin of the Seismological Society of America*, 99(2B):1315–1332. Cited on page 13.

Prodehl, C., Mueller, S., and Haak, V. (2006). Chapter 4 The european cenozoic rift system. In Olsen, K. H., editor, *Continental rifts:evolution, structure, tectonics*, volume 25 of *Developments in Geotectonics*, pages 133–212. Elsevier. Cited on page 59.

Przybilla, J. and Korn, M. (2008). Monte Carlo simulation of radiative energy transfer in continuous elastic random media-three-component envelopes and numerical validation. *Geophysical Journal International*, 173(2):566–576. Cited on pages 32, 34, 51, 54, 55, 56, 57, and 68.

Przybilla, J., Korn, M., and Wegler, U. (2006). Radiative transfer of elastic waves versus finite difference simulations in two-dimensional random media. *Journal of Geophysical Research*, 111(B4):1–13. Cited on page 7.

Przybilla, J., Wegler, U., and Korn, M. (2009). Estimation of crustal scattering parameters with elastic radiative transfer theory. *Geophysical Journal International*, 178(2):1105–1111. Cited on pages 10, 65, 69, and 95.

Rothert, E. (2000). Small-scale heterogeneities below the Gräfenberg array, Germany from seismic wavefield fluctuations of Hindu Kush events. *Geophysical Journal International*, 140:175–184. Cited on pages 10, 84, and 96.

Rutherford, E. (1907). Some Cosmical Aspects of Radioactivity. *Journal of the Royal Astronomical Society of Canada*, pages 145–165. Cited on page 1.

Ryzhik, L., Papanicolaou, G., and Keller, J. (1996). Transport equations for elastic and other waves in random media. *Wave motion*, 24(4):327–370. Cited on pages 29 and 98.

Sato, H. (1977). Energy propagation including scattering effects: single isotropic scattering approximation. *J. Phys. Earth*, 25:27–41. Cited on page 7.

Sato, H., Fehler, M. C., and Maeda, T. (2012). *Seismic Wave Propagation and Scattering in the Heterogeneous Earth: Second Edition*. Springer Berlin Heidelberg, Berlin, Heidelberg. Cited on pages 7, 8, 10, 27, 32, 33, 35, 42, 45, 51, 54, and 65.

Schreiber, K., Hautmann, J., Velikoseltsev, A., Wassermann, J., Igel, H., Otero, J., Vernon, F., and Wells, J. (2009). Ring Laser Measurements of Ground Rotations for Seismology. *Bulletin of the Seismological Society of America*, 99(2B):1190–1198. Cited on pages 14 and 17.

Schreiber, K., Velikoseltsev, A., Rothacher, M., Klügel, T., Stedman, G., and Wiltshire, D. (2004). Direct measurement of diurnal polar motion by ring laser gyroscopes. *Journal of Geophysical Research*, 109(06):1–5. Cited on pages 14 and 15.

Segall, P. (2010). *Earthquake and Volcano Deformation*. Princton University Press. Cited on page 11.

Sens-Schönfelder, C., Margerin, L., and Campillo, M. (2009). Laterally heterogeneous scattering explains Lg blockage in the Pyrenees. *Journal of Geophysical Research*, 114(B7). Cited on pages 7, 10, 26, 27, 30, 34, 35, 37, 82, 84, 95, and 96.

Sens-Schönfelder, C. and Wegler, U. (2006). Radiative transfer theory for estimation of the seismic moment. *Geophysical Journal International*, 167(3):1363–1372. Cited on pages 7, 9, 10, 27, 28, 63, 84, 95, and 96.

Shapiro, N. M., Campillo, M., Margerin, L., Singh, S. K., Kostoglodov, V., and Pacheco, J. (2000). The Energy Partitioning and the Diffusive Character of the Seismic Coda. *Bulletin of the Seismological Society of America*, (June):655–665. Cited on page 98.

Shearer, P. and Earle, P. (2008). Observing and modeling elastic scattering in the deep Earth. *Advances in Geophysics*, 2687(08). Cited on pages 62, 75, and 82.

Shearer, P. M. (1999). *Introduction to seismology*. Cambridge Univ. Press. Cited on pages 42, 63, 75, and 82.

List of References

Spakman, W., Wortel, M. J. R., and Vlaar, N. J. (1988). The hellenic subduction zone: A tomographic image and its geodynamic implications. *Geophysical Research Letters*, 15(1):60–63. Cited on page 2.

Stein, S. and Wyssession, M. (2009). *An Introduction to Seismology, Earthquakes and Earth Structure*. Blackwell Publishing. Cited on page 6.

Stupazzini, M., de La Puente, J., Castellani, A., Smerzini, C., Igel, H., and Käser, M. (2009). Study of Rotational Ground Motion in the Near-Field Region. *Bulletin of the Seismological Society of America*, 99(2B):1271–1286. Cited on page 19.

Toksöz, M. N., Dainty, A. M., Reiter, E., and Wu, R.-S. (1988). A model for attenuation and scattering in the Earth's crust. *Pure and Applied Geophysics*, 128(1-2):81–100. Cited on page 6.

Trégourès, N., Hennino, R., Lacombe, C., Shapiro, N. M., Margerin, L., Campillo, M., and van Tiggelen, B. a. (2002). Multiple scattering of seismic waves. *Ultrasonics*, 40(1-8):269–74. Cited on page 5.

Turner, J. A. and Weaver, R. L. (1994). Radiative transfer of ultrasound of ultrasound. Cited on pages 28 and 30.

Vallée, M. (2013). Source time function properties indicate a strain drop independent of earthquake depth and magnitude. *Nature Communications*, 4. Cited on page 92.

Vallée, M., Charléty, J., Ferreira, a. M. G., Delouis, B., and Vergoz, J. (2011). SCARDEC: a new technique for the rapid determination of seismic moment magnitude, focal mechanism and source time functions for large earthquakes using body-wave deconvolution. *Geophysical Journal International*, 184(1):338–358. Cited on page 92.

van Driel, M., Wassermann, J., Nader, M., Schuberth, B., and Igel, H. (2012). Strain rotation coupling and its implications on the measurement of rotational ground motions. *Journal of Seismology*, 16:657–668. Cited on page 19.

Vavryčuk, V. (2011). Detection of high-frequency tensile vibrations of a fault during shear rupturing: observations from the 2008 West Bohemia swarm. *Geophysical Journal International*, 186(3):1404–1414. Cited on page 60.

Virieux, J. (1986). P-sv wave propagation in heterogeneous media: velocity-stress finite-difference method. *Geophysics*, 51(4):889–901. Cited on page 49.

Weaver, R. (1990). Diffusivity of ultrasound in polycrystals. *Journal of the Mechanics and Physics of Solids*. Cited on page 28.

Wegler, U. and Lühr, B.-G. (2001). Scattering behaviour at Merapi volcano (Java) revealed from an active seismic experiment. *Geophysical Journal International*, 145(3):579–592. Cited on pages 7 and 9.

Weinlich, F., Bräuer, K., Kämpf, H., and Strauch, G. (2003). Gas flux and tectonic structure in the western Eger Rift, Karlovy Vary–Oberpfalz and Oberfranken, Bavaria. *Geolines*, 15:181–187. Cited on page 59.

Wettzell, F. (2015). www.fs.wettzell.de. *Webpage, last visited 09.01.2015*. Cited on page 14.

Wiechert, E. (1897). Über die Masseverteilung im Innern der Erde. *Nachrichten von der Gesellschaft der Wissenschaften zu Göttingen*, pages 145–165. Cited on page 1.

Wu, R. (1985). Multiple scattering and energy transfer of seismic waves—separation of scattering effect from intrinsic attenuation—I. Theoretical modelling. *Geophys. J. R. Astr. Soc*, 82:57–80. Cited on page 7.

Wu, R. and Aki, K. (1988). Multiple Scattering and Energy Transfer of Seismic Waves - Separation of Scattering Effect from Intrinsic Attenuation II. Application of the Theory to Hindu Kush Region. *Pure and Applied Geophysics*, 128. Cited on page 7.

Yoshimoto, K. (2000). Monte Carlo simulation of seismogram envelopes in scattering media. *Journal of Geophysical Research*, 105:6153–6161. Cited on pages 34 and 35.

Zeis, S., Gajewski, D., and Prodehl, C. (1990). Crustal structure of southern Germany from seismic refraction data. *Tectonophysics*, 176:59–86. Cited on pages 62 and 80.

Zeng, Y., Su, F., and Aki, K. (1991). Scattering wave energy propagation in a random isotropic scattering medium. 1. Theory. *Journal of Geophysical Research*, 96:607–619. Cited on page 34.

Zhao, D. (2001). Seismic structure and origin of hotspots and mantle plumes. *Earth and Planetary Science Letters*, 192(3):251 – 265. Cited on page 2.

List of Figures

List of Tables

Scientific development

2014/04 – 2015/06	**Wissenschaftlicher Mitarbeiter**, BGR Hannover
2011/02 – 2014/03	**Promotionsstudent**, Universität Leipzig und GFZ Potsdam
2008/10 – 2010/10	**Studium der Geophysik**, LMU und TU München (M.Sc.)
2005/10 – 2008/09	**Studium der Geowissenschaften**, LMU und TU München (B.Sc)
2003/10 – 2005/09	**Studium der Humanmedizin**, LMU München
1993/09 – 2002/09	**Christop-Scheiner-Gymnasium**, Ingolstadt (Abitur)